Turbulent dissipation along contrasting internal tides paths, off the Amazon shelf from AMAZOMIX

Fabius Kouogang[1,5~~4~~], Ariane Koch-Larrouy[1], Jorge Magalhaes[2], Alex Costa da Silva[4], Daphne Kerhervé[1], Arnaud Bertrand[5], Evan Cervelli[3], Fernand Assene4[~~1~~], Jean-François Ternon6[~~5~~], Pierre Rousselot7[~~6~~], James Lee8[~~7~~], Marcelo Rollnic8[~~7~~], Moacyr Araujo5[4]

[1]~~LEGOS, Université de Toulouse, CNRS, OMP, IRD, Toulouse, France~~ CECI, Université de Toulouse, CERFACS/CNRS/IRD, Toulouse, France

[2]Department of Geoscience, Environment and Spatial Planning (DGAOT), Faculty of Sciences, University of Porto, Porto, Portugal

[3]Rockland Scientific Inc, Lunenburg, Nova Scotia, Canada

4Centro Euro-Mediterraneo sui Cambiamenti Climatici, Bologna, Italy

5[~~4~~]Departamento de Oceanografia, Universidade Federal de Pernambuco, DOCEAN/UFPE, Recife, Brazil

6[~~5~~]MARBEC, Université de Montpellier, CNRS, Ifremer, IRD, Sète, France

7[~~6~~]IMAGO, Université de Bretagne Occidentale, CNRS, Ifremer, IRD, Brest, France

8[~~7~~]Departamento de Oceanografia, Universidade Federal do Pará, UFPA, Belém, Brazil

Correspondence to: Fabius Kouogang (fabius.cedric@yahoo.fr)

Abstract.

The Amazon shelf break is a key oceanic region where strong internal tides (ITs) are generated, playing a substantial~~significant~~ role in climate processes and ecosystems through vertical mixing. During the AMAZOMIX survey (2021), currents, hydrography, and turbulence were measured over the M_2 tidal period (12.42 hrs) at multiple stations along both high (HTE) and low (LTE) tidal energy paths, covering IT generation and propagation regions off the Amazon shelf. This dataset provides a unique opportunity to assess IT-driven vertical mixing and quantify its spatial extent and influence in the region.~~at numerous sites near the Amazon outflow, where ITs are also generated along the slope. This dataset offers an opportunity to explore the influence of ITs on vertical mixing off the Amazon shelf, as well as to quantify the extent and locations of this impact.~~ Microstructure analyses, integrated with hydrographic data, highlighted contrasting dissipation rates. The highest ~~dissipation~~ rates occurred at IT generation sites ~~and~~ along the HTE paths~~IT pathways~~, while the lowest rates~~values~~ were observed on the slope along the LTE path~~in non-tidal areas~~. Near generation sites, mixing rates were elevated, ~~between~~ [10^{-6}~~, 10^{-5}~~] W kg^{-1}, with IT shear contributing ~60~~5~~%~~ %~~, compared to mean baroclinic current (MBC) shear. Along IT path~~way~~s ~~and in far-field IT~~

Formatted: Subscript

~~regions~~, mixing decreased to [10^{-8}~~, 10^{-7}~~] W kg^{-1} but remained substantial, driven by nearly equal contributions from IT and MBC shear.

A key finding was the relative increase in mixing ([10^{-7}~~, 10^{-6}~~] W kg^{-1}) ~ 230 km from two distinct IT generation sites at the shelf break. This zone of high mixing was located in an area where the general circulation vanished, coinciding with a region of potential constructive interference of IT rays originating from different generation sites. It also aligned with the occurrence of large-amplitude internal solitary waves (ISWs), suggesting that constructive IT ray interference may generate nonlinear ISWs, leading to enhanced mixing.~~This region of increased mixing coincided with the constructive interference of IT rays from different generation sites. It also aligned with the presence of large-amplitude internal solitary waves (ISWs) observed in satellite imagery, suggesting that constructive IT ray interference may generate non-linear ISWs, leading to intensified mixing~~. ~~These findings provide valuable insights for developing parameterizations of tidal and mean shear mixing for ocean or coupled models, with significant implications for regional biogeochemistry and the climate system.~~

1 Introduction

Turbulent mixing in the ocean is essential for sustaining thermohaline and meridional overturning circulation and for maintaining the global ocean energy budget (Kunze, 2017; Koch-Larrouy et al., 2010). It regulates climate by controlling heat and carbon transport and providing nutrients for photosynthesis (Huthnance, 1995; Munk & Wunsch, 1998). Mixing effects are often reflected in step-like density features, indicating homogeneous regions (Koch-Larrouy et al., 2015; Bouruet-Aubertot et al., 2018). Ocean mixing can be driven by processes like current shear (Rainville and Pinkel, 2006; Whalen et al., 2012; Miles, 1961), river plumes (Ruault et al., 2020), fronts (Geyer, 1995), overturns (Thorpe, 2018; Munk & Wunsch, 1998), and tides (Zhao et al., 2012).

Barotropic tides interacting with sharp topography generate internal tides (ITs), strong internal waves at tidal frequencies and harmonics (Zhao et al., 2016). ITs can create strong vertical displacements of up to tens of meters (Garrett & Kunze, 2007) and may propagate offshore. As they propagate, ITs can interact with topography, stratification, waves, currents, and eddies (Whalen et al., 2012; Bordois, 2015; Ivey et al., 2020; Inall et al., 2021), leading to complex offshore mixing (Gill, 1982). ITs can also destabilize, break, and dissipate locally (Zhao et al., 2016), and their intensity and path can change due to environmental factors, potentially generating nonlinear Internal Solitary Waves (ISWs; Jackson et al., 2012).

These processes are prominent in the Amazon River-Ocean Continuum (AROC) in the western tropical Atlantic. This dynamic region, shaped by interactions between currents, eddies, the Amazon River plume, and internal waves, drives complex circulation and vertical mixing. The North Brazil Current (NBC), the region's dominant western boundary current, flows northwest along the coast (Fig. 1), with velocities of ~1.2 m s^{-1} and a vertical extent of up to 100 m, transporting warm, saline waters from the South Atlantic (Barnier et al., 2001). The NBC influences the Amazon plume's dispersal and contributes to mesoscale eddy formation (Johns et al., 1998; Bourlès et al., 1999; Neto & Silva, 2014). The Amazon plume shows strong seasonal variability, extending up to 1500 km offshore during the rainy season (May–July) and retreating to under 500 km during the dry season (September–November; Coles et al., 2013).

At the Amazon shelf break, internal waves, such as ITs and ISWs, are generated, propagate, and dissipate. These waves have been observed through in situ measurements (Brandt et al., 2002) and SAR satellite imagery (Magalhães et al., 2016). Recently, de Macedo et al. (2023) used MODIS images to identify frequent mode-1 ISWs originating from two IT generation sites (A^a and A^b ; Figs. 1, 2a, and 2b), with wavelengths ranging from 72 to 128 km. These ISWs appeared where Tchilibou et al. (2022) predicted IT energy dissipation using numerical modeling. Their findings suggest that ~30% of M2 IT energy dissipates near generation sites (A^a, A^b, and E; Fig. 1), corresponding to higher-mode ITs, while lower-mode ITs propagate offshore, where they dissipate and enhance mixing. Offshore mixing may result from shear instabilities driven by interactions between currents, eddies, the Amazon plume, ITs, and coupled processes (e.g., wave-wave, wave-current, or plume-wave interactions). However, no direct dissipation measurements have been made in this region to quantify IT-driven mixing.

To address this, the AMAZOMIX cruise (Bertrand et al., 2021) was conducted to investigate IT-driven mixing off the Amazon shelf. Microstructure and hydrographic measurements were collected at repeated stations over an M2 tidal cycle (~12.42 hrs), providing dissipation estimates and insights into associated processes. Stations were positioned along contrasting IT paths, such as high tidal energy (HTE) paths (sites A^a and A^b ; Fig. 1) and low tidal energy (LTE) path (site E; Fig. 1), enabling dissipation quantification in varying tidal regimes. The AMAZOMIX dataset provides a unique opportunity to assess the role of ITs in mixing within the AROC region.

~~Turbulent mixing in the ocean plays an important role in sustaining the thermohaline and meridional overturning circulation and in closing the global ocean energy budget (Kunze, 2017). These processes have strong implications for the climate, influencing heat and carbon transport, as well as nutrients supply for photosynthesis (Huthnance, 1995; Munk and Wunsch, 1998). Mixing processes can result from wind in the surface waters layer, internal waves and shear instability in the ocean interior, and bottom friction near the bottom layer (Miles, 1961; Thorpe, 2018; Ivey et al., 2020; Inall et al., 2021). Barotropic tides interacting with steep shelf-break topography trigger internal waves at tidal frequencies and harmonics, known as internal tides (ITs), which can propagate and produce mixing. These ITs can be expressed by large vertical displacements (up to tens of meters) of water masses (Garrett and Kunze, 2007). After their generation on the shelf-break, the (more unstable) higher modes of ITs may dissipate locally, while the lower modes can propagate far away (Zhao et al., 2016). IT beams (generated where the slope of the ITs and the topography match together on the shelf-break) can propagate vertically, resulting in reflection, scattering and dissipation of ITs at the bottom, surface waters, or thermocline levels (New and Da Silva, 2002; Gerkema and Zimmerman, 2008; Bordois, 2015; Zhao et al. 2016). They can also dissipate when energy fluxes interfere (Zhao~~

~~et al., 2012) or interact with strong baroclinic eddies or currents (Rainville and Pinkel, 2006; Whalen et al., 2012). Furthermore, ITs may disintegrate into packets of higher-mode nonlinear internal solitary waves (ISWs), which can propagate and dissipate offshore (Jackson et al., 2012).~~

~~Previous and recent studies have shown that ITs-induced turbulent mixing can affect the surface, such as sea surface temperature (Ray and Susanto, 2016; Nugroho et al., 2018; Assene et al., 2024), chlorophyll content (Muacho et al., 2014; M'Hamdi et al., in preparation), marine ecosystems (Wang et al., 2007; Zaron et al., 2023), and atmospheric convection and the rainfall structure (Koch-Larrouy et al., 2010, Sprintall et al. 2014).~~

~~In the western tropical Atlantic, the Amazon River-Ocean Continuum (AROC) constitutes a key region of the global oceanic and climate system (Araujo et al., 2017; Varona et al., 2018). This region (Fig. 1a) is characterized by a system of western boundary currents, including North Brazil Current (NBC). NBC, which flows northwestward, has its core velocities (~ 1.2 m s^{-1}) that remain stable from the surface to a depth of 100 m (Johns et al., 1998; Bourlès et al., 1999; Barnier et al., 2001; Neto and Silva, 2014). This region also experiences highly variable dynamics due to the Amazon River Plume. During the rainy season (May-July), peak discharge can extend the plume over 1500 km offshore, northwest along the NBC. In the dry season (September-November), reduced discharge and stronger saline intrusion may confine the plume to less than 500 km offshore, near the Amazon Shelf, with some eastward dispersion (Coles et al., 2013). The Amazon plume can generate vertical shear in underlying currents, enhancing mixing. Additionally, a system of Amazonian Lenses of water (AWL), influenced by continental inputs, may affect both the boundary layer and mixed layer patterns (Silva et al., 2005; Prestes et al., 2018).~~

~~In the AROC region, the Amazon shelf-break is a hotspot for the generation, propagation and dissipation of ITs and ISWs as a result of non-linear processes (Geyer, 1995; Brandt et al., 2002; Magalhães et al., 2016; Ruault et al., 2020; Tchilibou et al., 2022; Fig 1). Previous studies using Synthetic Aperture Radar (SAR) satellite images (Magalhaes et al., 2016) identified ISWs along the path of ITs propagating from two sites (i.e., sites Aa and Ab; Fig. 1a). Conversely, other sites showed no ISWs propagation (i.e., sites E and D; Fig. 1a, 1b and 1c) (see Magalhaes et al., 2016 for definition). Using numerical modeling, Tchilibou et al. (2022) showed that about 30 % of the M2 (dominant tidal component; Le Bars et al. 2010) ITs energy is dissipated locally (for higher-modes ITs) at sites E, Aa, Ab and D (Fig. 1a), while the remaining lower-modes ITs energy can be dissipated remotely. Dissipation away from the generation sites (E, Aa, Ab and D; Fig. 1a) can result from the shear instabilities caused by ITs-ITs and/or ITs-eddy/current interactions. Despite the presence of ITs, no direct measurements of dissipation rates have been conducted to our knowledge.~~

~~The mixing induced by these internal waves in the region was observed during the AMAZOMIX cruise (Bertrand et al., 2021). The cruise was designed with stations/transects inside and outside ITs fields (Fig. 1a and 1c) to measure ITs dissipation and study their impact on the AROC ecosystem. Direct microstructure measurements of temperature, salinity and velocity were conducted at the different repeated stations/transects over a M2 tidal cycle (~ 12.42 h). These cruise measurements offer an~~

~~opportunity to explore whether ITs play a role in mixing within the AROC region. In this study, we will quantify mixing and identify the associated processes off the Amazon shelf. We will calculate turbulent kinetic energy (TKE) dissipation rates, vertical displacements of isopycnal surfaces and vertical eddy diffusivities using in situ microstructure and hydrography data. Finally, the baroclinic shear of currents and their contributions to mixing will be calculated from current data collected between stations and transects.~~

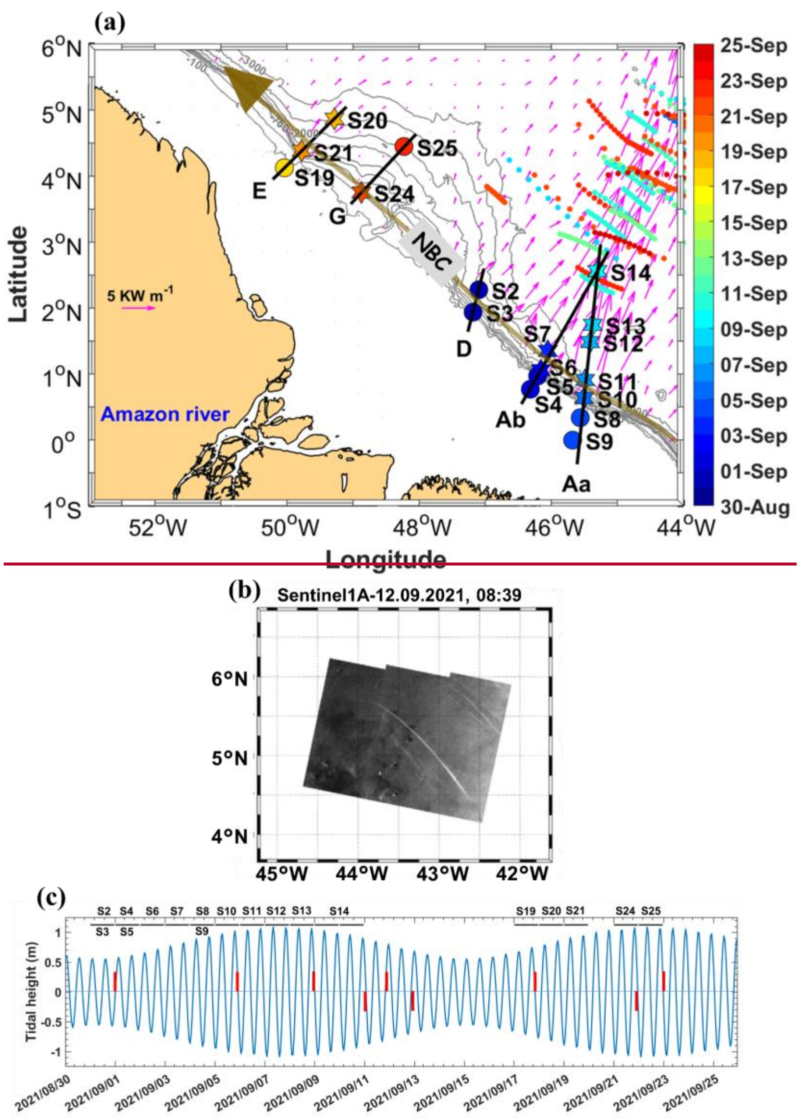
(a)
6°N
5°N
4°N
3°N
2°N
1°N
0°
1°S
52°W
50°W
48°W
46°W
44°W
Latitude
Longitude
5 KW m-1
Amazon river
NBC
S20
S21
S19
S25
S24
E
G
S2
S3
D
S7
S6
S5
S4
Ab
S14
S13
S12
S11
S10
S8
S9
Aa
25-Sep
23-Sep
21-Sep
19-Sep
17-Sep
15-Sep
13-Sep
11-Sep
09-Sep
07-Sep
05-Sep
03-Sep
01-Sep
30-Aug
(b)
Sentinel1A-12.09.2021, 08:39
6°N
5°N
4°N
45°W
44°W
43°W
42°W
(c)
S2 S4 S6 S7 S8 S10 S11 S12 S13 S14 S19 S20 S21 S24 S25
S3 S5 S9
Tidal height (m)
2021/08/30
2021/09/01
2021/09/03
2021/09/05
2021/09/07
2021/09/09
2021/09/11
2021/09/13
2021/09/15
2021/09/17
2021/09/19
2021/09/21
2021/09/23
2021/09/25
Time (d)

Formatted: Font: Italic

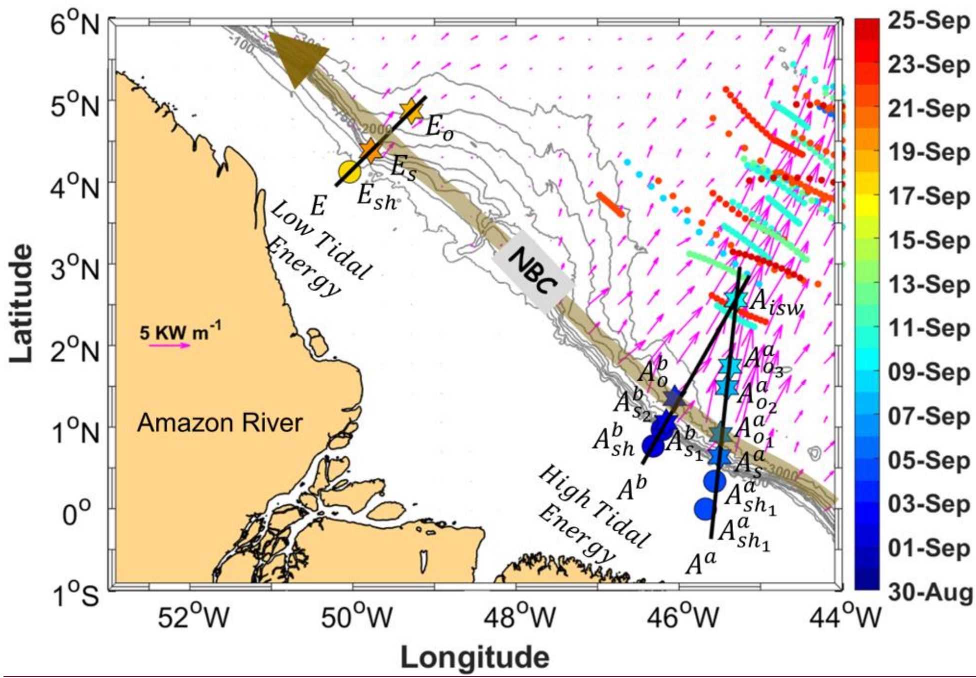

Figure 1: Map of a part of the AMAZOMIX 2021 cruise off the Amazon shelf, showing bathymetric contours (100 m, 750 m, 2000 m, and 3000 m isobaths) in gray. Magenta arrows show the 25-hour mean depth-integrated baroclinic IT energy flux (September 2015, from the NEMO model) originating from IT generation sites (A^a, A^b, and E) along the shelf break. Solid black lines depict transects (A^a, A^b, and E) defined on the high tidal energy (HTE) and low tidal energy (LTE) paths. The solid brown line represents the NBC pathways, illustrating background circulation. Shattered colored lines highlight ISW signatures. Colored circles and stars indicate short and long CTD-O2/L-S-ADCP stations, respectively, with the corresponding sampling dates represented by the color bar. The superscripts "a" and "b" on station names correspond to sites A^a and A^b, respectively. The subscripts "sh", "s", "o", and "isw" indicate station locations: shelf ($A^a_{sh_1}$, $A^a_{sh_2}$, A^b_{sh}, and Esh), slope (A^a_s, $A^b_{s_1}$, $A^b_{s_2}$, and Es), open ocean ($A^a_{o_1}$, $A^a_{o_2}$, $A^a_{o_3}$, A^b_o, and Eo), and ISW regions (Aisw) for sites A^a, A^b and E, respectively.

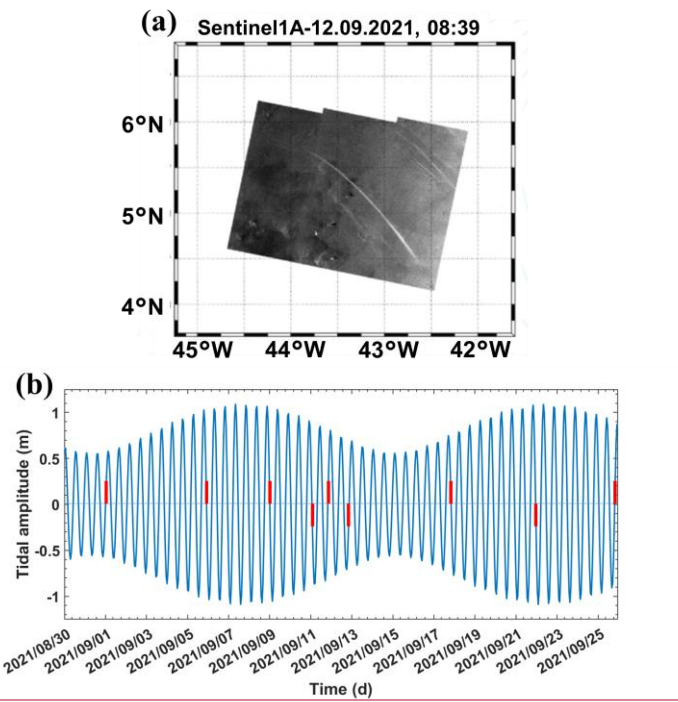

Figure 2: a) 1A Sentinel image acquired on 12th September 2021, showing ISW signatures. b) Tidal (M_2 and S_2) amplitude of the currents (at -45.5°W, 1°N) derived from the FES2014 model (Lyard et al., 2014). ISW signature dates are marked by red bars.

~~*Figure 1: a) Map of a part of the AMAZOMIX 2021 cruise off the Amazon shelf, showing bathymetric contours (100 m, 750 m, 2000 m, and 3000 m isobaths) in gray. Colored circles and stars indicate short and long CTD-O2/L-S-ADCP stations, respectively, with the corresponding sampling dates represented by the color bar. Solid black lines depict SADCP transects (for Aa, Ab, D, G, and E). Magenta arrows show the 25-hour mean depth-integrated baroclinic IT energy flux (September 2015, from the NEMO model) originating from IT generation sites (Aa, Ab, D, and E) along the shelf break. The solid brown line represents the NBC pathways illustrating background circulation. Shattered colored lines highlight ISW signatures. b) 1A*~~

~~*Sentinel image acquired on 12th September 2021, showing ISW signatures. c) Tidal range at AMAZOMIX stations, with ISW signature dates marked by red bars.*~~

2 Data and Methods

2.1 Data collection

The AMAZOMIX cruise (Bertrand et al., 2021) was performed over the shelf/slope areas off the AROC during August-October 2021 aboard the IRD vessel RV *ANTEA*. At each designated site, 12-hour stations were set up, with repeated casts (4-5 casts per site) of Conductivity-Temperature-Depth-Oxygen (CTD-O_2)/Lowered Acoustic Doppler Current Profiler (LADCP) and Velocity Microstructure Profiler (VMP) to measure the Turbulent Kinetic Energy (TKE) dissipation rates over a complete tidal (M_2) cycle, allowing the separation of the tidal component from the total current. A high-resolution (1/36°) NEMO (Nucleus for European Modeling of the Ocean) model (Madec et al., 2019) was used to determine station locations based on realistic IT generation and propagation maps (Tchilibou et al., 2022; Assene et al., 2024) and to estimate the mean background stratification. Measurement stations for short- and long-duration (~12 hrs) deployments were systematically named and organized by location along the HTE and LTE paths. Stations at sites A^a and A^b were marked with superscripts "a" and "b", respectively. Subscripts denoted specific regions: "sh" for shelf ($A^a_{sh_1}$, $A^a_{sh_2}$, A^b_{sh}, and Esh), "s" for slope (A^a_s, $A^b_{s_1}$, $A^b_{s_2}$, and Es), "o" for offshore/open ocean ($A^a_{o_1}$, $A^a_{o_2}$, $A^a_{o_3}$, A^b_o, and Eo), and "isw" for ISW regions (Aisw) (Fig. 1; Table A1, Appendix A). ~~Stations (Figs. 1a and 1c) were located inside the ITs fields, named "IN-ITs" (sites Aa, Ab and D: S2 to S14; site E: S19 to S21), and outside the ITs fields (S24 and S25), named "OUT-ITs", on the shelf-break generation (sites Aa, Ab, D and EF) and propagation along 5 transects (Aa, Ab, D, G, and E; Fig. 1).~~

CTD-O_2 measurements were obtained using a Seabird 911 Plus with dual sensors mounted in the rosette. The 24 Hz CTD-O_2 sensors were calibrated before and after the cruise to ensure accurate dissolved oxygen measurements throughout the survey. The temperature, salinity, and oxygen standard deviation between the CTD-O_2 sensors and the bottle samples was 0.003 °C, 0.003 PSU, and 0.05 ml l^{-1}, respectively. ~~The standard deviation of temperature (salinity; oxygen) was 0.003 °C (0.003 PSU; 0.05 ml l^{-1}) according to adjusted data.~~ CTD-O_2 data were averaged over 1-m bins to filter out spikes and missing points~~,~~ and aligned in time to correct the lag effects.

Two 300 kHz RDI LADCPs were mounted on the rosette to provide vertical current profiles with 8 m resolution, supplemented by 75 kHz shipboard ADCP (SADCP) profiles recorded continuously during the cruise. Vertical resolution of SADCP was adjusted according to bottom depth, e.g., 8 m for depths >150 m (at $A^b_{s_2}$, A^b_o, A^a_s, Aisw, Es and Eo) ~~(at S6, S7, S10-S14, S20, S21, and S24)~~ and 4 m for other depths. Data processing and quality control followed GO-SHIP Repeat Hydrography Manual protocols. In total, 71 CTD-O_2/LADCP profiles were collected during the AMAZOMIX cruise.

To characterize mixing, the TKE microstructure profiles were obtained from high-frequency (~2 mm resolution) measurements of temperature and velocity shear using a VMP-250 profiler (Rockland Scientific International, Inc.) capable of reaching depths up to 1000 m. The VMP-250 features two high-resolution thermistors (FP07) and two high-resolution velocity shear probes (probes 1 and 2; with 5%~~ %~~ signal accuracy), with a sampling rate of 1024 Hz. The profiler was deployed and retrieved via an electric winch and rope tether, with alternating deployments between the CTD-O_2/LADCP profiles at 33 stations, yielding a total of 201~~2~~ profiles. For this study, data from 14~~8~~ stations ~~(S2-S14, S19-S21, S24, and S25)~~ comprising SADCP data, 109 VMP profiles, and 54 CTD-O2/LADCP profiles will be analyzed.

2.2 Methods

2.2.1 TKE dissipation rates

The VMP data are processed using the ODAS Matlab library (developed by Rockland Scientific International, Inc.) to infer the TKE dissipation rate (ε). The processing methods for the VMP data are briefly described here and adhere to the recommendations of ATOMIX (Analyzing ocean Turbulence Observations to quantify MIXing), as reported by Lueck et al. (2024), and have been validated against the benchmark estimates (presented in Fer et al., 2024).

First, the VMP data are converted into physical shear units, and the time series are prepared. Continuous sections of the time series are selected for dissipation estimation. Before spectral estimation, the aberrant shear signals caused by vessel wake contamination are removed. Collisions of the shear probe with plankton and other particles are removed using the de-spiking routine. The records from each section are then high-pass filtered (e.g., at station $A^b_{s_2}$; Fig. 3~~S6 and S10; Fig. 2a, and Fig. A1, Appendix~~).

Shear spectra are estimated using record lengths (L) and Fast Fourier Transform segments of 2 s, which are cosine windowed and overlapped by 50%~~ %~~ (e.g., at station $A^b_{s_2}$; Fig. 3~~S6 and S10; Fig. 2b, and Fig. A1, Appendix~~). Additionally, vibration-coherent noise is removed. Different L and overlap (O) settings were selected and tested based on the environment (e.g., deep vs. shallow water), following Fer et al. (2024). For shallow stations, L (O) was shortened to 5 s (2.5 s), in contrast to the 8 s (4 s) used for deeper stations, due to evidence of overturns observed in AMAZOMIX acoustic measurements at deeper stations (A. Koch-Larrouy, personal communication, September 20, 2024)~~(Koch-Larrouy et al., 2024; in preparation)~~. This adjustment helped to optimize the spatial resolution of dissipation estimates in shallow water stations.

Finally, ε is determined using the spectral integration method and by comparison with the Nasmyth empirical spectrum (Nasmyth, 1970). Quality assurance tests are carried out in accordance with ATOMIX's recommendations (Lueck et al., 2024). A figure of merit < 1.4 is used to exclude bad data (e.g., at station $A^b_{s_2}$; Fig. 3~~S6 and S10; Fig. 2b, and Fig. A1, Appendix~~), and the fraction of data affected by de-spiking is < 0.05.

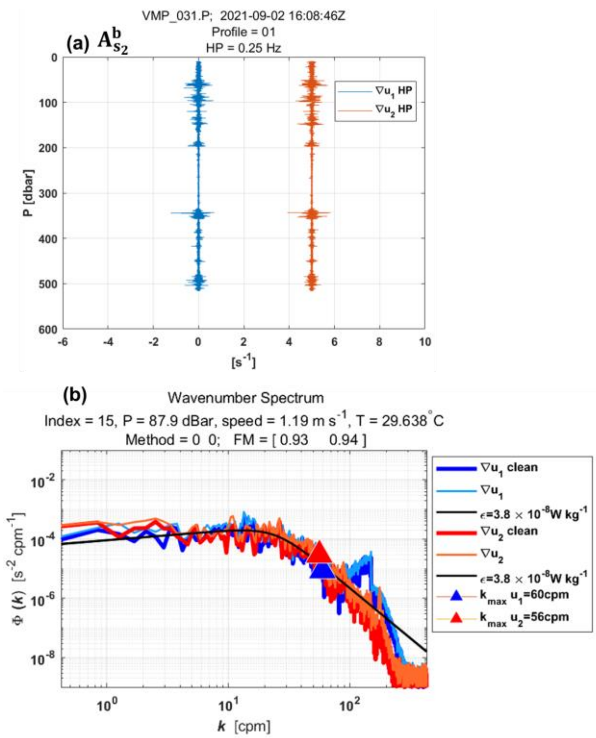

Figure 3~~2~~: Example of wavenumber spectra from a dissipation structure segment used to determine the dissipation rate at station $A^b_{s_2}$ ~~S6~~ at a pressure of 87.9 dBar. (a) Cleaned and high-pass filtered signals from shear probe 1 (blue) and shear probe 2 (red, offset by 5 s^{-1}). (b) Wavenumber spectra for shear probes 1 and 2. Thick lines (blue for probe 1, red for probe 2) show shear spectra with coherent noise correction, while thin lines (sky blue for probe 1, orange for probe 2) show spectra without correction. Triangles mark the maximum wavenumber used for dissipation rate estimation. Black lines represent Nasmyth reference spectra for an estimated dissipation rate of 3.8×10^{-8} W kg^{-1} for both shear probes. Dissipation rate estimates for shear probe 1 and shear probe 2 at a pressure of 87.9 dBar yielded a figure of merit of 0.93 and 0.94, respectively.

~~**The vertical eddy diffusivity coefficient**~~

~~The efficiency of turbulence in redistributing tracer varianceenergy is assessed through the calculation of the vertical eddy diffusivity coefficient (K_z). This diffusivitycoefficient is particularly significant in regions such as the pycnocline layerss, where stratification suppresses large-scale mixing, making turbulence-driven mixing a key mechanism for vertical energy transport across layers (Thorpe, 2007).~~

~~K_z is calculated from ε following the formulation of Osborn (1980), given by $K_z = \varepsilon\, \Gamma\, N^{-2}$. Here, N^2 is the buoyancy frequency squared, which is calculated using the sorted potential density profiles (σ_θ) obtained from CTD-O_2 data. It is given by $N^2 = -(g/\rho_0)\,(d\sigma_\theta/dz)$, where ρ_0 is a reference density (1025 kg m^{-3}) and g is the gravitational acceleration. Γ is the mixing efficiency, defined as the ratio between the buoyancy flux and the energy dissipation, and is typically set to 0.2, which corresponds to the critical Richardson number Ri = 0.17 (Osborn, 1980). ε is linearly interpolated into the depths of N^2.~~

~~Turbulence dissipation within the pycnocline can reduce stratification and increase vertical eddy diffusivity below the mixing layer (Thorpe, 2007). Subsurface mixing, driven by the breaking of ITs and shear instabilities, plays a particularly important role at the base ofbelow the mixed layer, especially in equatorial waters (Gregg et al., 2003).~~

Subsurface mixing, driven by IT breaking and shear instabilities, substantially influences the base of the mixed layer, particularly in equatorial waters (Gregg et al., 2003). To analyze midwater dissipation rates (excluding surface and bottom boundary layers), we define the following depths: Mixed Layer Depth (MLD), miXing Layer Depth (XLD), and Bottom Boundary Layer (BBL) thickness (HBBL).

There are several criteria for defining the ~~Mixed Layer Depth (~~MLD~~)~~. In this study, we use the commonly accepted density threshold criterion of 0.03 kg m^{-3}, as defined by de Boyer Montégut et al. (2004) and Sutherland et al. (2014), to estimate the MLD ~~for each CTD-O_2 profile~~ (Table A2, Appendix B). ~~Notably, comparisons with density thresholds of 0.01 and 0.02 kg m^{-3} revealed no major differences in MLD across the AMAZOMIX stations and transects (Fig. A2, Appendix).~~

The ~~miXing Layer Depth (~~XLD~~)~~ is defined as the depth at which ε decreases to a background level (Sutherland et al., 2014). Previous studies have applied various thresholds for background dissipation levels, such as~~,~~ 10^{-8} and 10^{-9} W kg^{-1} in higher latitudes based on in situ observations (Brainerd and Gregg, 1995; Lozovatsky et al., 2006; Cisewski et al., 2008; Sutherland et al., 2014~~; Lozovatsky et al., 2006; Cisewski et al., 2008; Brainerd and Gregg, 1995~~), and 10^{-5} m^2 s^{-1} using an ocean general circulation model (Noh and Lee, 2008). In this study, the XLD is specified as the depth where ε decreases~~drops~~ from the~~its~~ first minimum value (e.g., 10-9 W kg-1 for A_o^b) (Table A2, Appendix B). This aligns with previous dissipation thresholds and ensures that mixing is captured in midwater.~~outside the surfacecaptured surface and bottom boundary layerindependently of surface influences.~~ Huang et al. (2019) showed that the HBBL spatially varies between 15 and 123 m in the Atlantic Ocean, with a median of ~30-40 m in the North Atlantic. According to their findings, and based on bathymetry measurements and near-bottom current measurements from CTD-O2/LADCP, we define the HBBL in our study as 18 m for shallow stations and 40 m for deep stations. ~~The Upper (UTD) and Lower (LTD/LPD) Thermocline/Pycnocline Depth are delimited as defined by~~

~~Assunçao et al. (2020). UTD corresponded to the depth where the vertical temperature gradient □□/□□ = 0.1 °C m^{-1}, while LTD/LPD were the last depths below the UTD at which $N^2 \geq 10^{-4}$ s^{-2}.~~

2.2.2 **Baroclinic currents**

To analyze the processes explaining dissipation and mixing, particularly along ~~internal tidal (~~IT~~)~~ paths, we estimate shear instabilities associated with the semi-diurnal (M_2) ITs and mean circulation, as well as their contributions to mixing.

The M2 tidal component of the tidal current is derived by calculating the baroclinic (semi-diurnal) tidal velocity $[u'', v'']$ ~~(Fig. A3, Appendix)~~, following these equations:

$$[u', v'] = [u, v] - [u_{bt}, v_{bt}], \qquad (1)$$

$$[u_{bt}, v_{bt}] = \frac{1}{H}\int_{-H}^{0} [u, v]dz, \qquad (2)$$

$$[u'', v''] = [u', v'] - [\underline{u'}, \underline{v'}]. \qquad (3)$$

Here, $[u, v]$ represent total horizontal (zonal u and meridional v) velocities ~~(Fig. A3, Appendix)~~ obtained from SADCP data. The components $[u', v']$ and $[u_{bt}, v_{bt}]$ represent baroclinic and barotropic components of horizontal velocities, respectively ~~(Fig. A3, Appendix)~~. H is water depth. The baroclinic mean velocities $[\underline{u'}, \underline{v'}]$ ~~(Fig. A3, Appendix)~~, calculated to estimate mean circulation along IT paths, are decomposed into along-shore $\underline{u'_l}$ and cross-shore $\underline{u'_c}$ velocities. The overbar denotes the average over the~~a~~ M_2 tidal period. Similarly, the components $[u'', v'']$ are decomposed into along-shelf u''_l and cross-shelf u''_c velocities. The along-shelf velocity component is defined parallel to the 200 m isobath (treated as the coastline), with positive values indicating northwestward flow and negative values indicating southeastward flow. The cross-shelf velocity component is defined perpendicular to the 200 m isobath, with positive values indicating northeastward flow and negative values indicating southwestward flow.

Note that continuously collected SADCP for some stations ~~(e.g., S11)~~ are not sufficiently resolved due to gaps filled by interpolating between time points. The similar processing is applied to the CTD-O_2 data~~ collected alternately~~. SADCP time series data are less than 17 hours at all long stations, except for S14, which spans 42 hours. As a result, the diurnal and semidiurnal period fittings are not formally distinct (except at Aisw~~S14; Figs. A4 and A5, Appendix~~), and the inertial period (at least 5 days) cannot be resolved in our dataset. This limits our ability to separate currents by frequency and examine the associated dissipation.

The velocity profiles from LADCP are glued into our SADCP time series data below ~500 m depth at long stations.

To evaluate shear instabilities associated with ITs and the mean background circulation, we compute the baroclinic tidal vertical shear squared ($S^{2''}$) and mean shear squared ($\underline{S^{2'}}$) ~~(Fig. A3, Appendix)~~, as follows:

Formatted: Subscript

$$S^{2''} = (\partial u''/\partial z)^2 + (\partial v''/\partial z)^2, \quad (4)$$

$$S^{2'} = (\partial u'/\partial z)^2 + (\partial v'/\partial z)^2. \quad (5)$$

~~To evaluate the impact of bottom friction on mixing, we calculate kinetic energy $E\varepsilon_f = \frac{1}{2}\rho_s(u_f^2)$ near the bottom boundary layer at shallow stations using friction velocity $u_f = u_b\sqrt{C_d}$, where $C_d = 2.5 \times 10^{-3}$ is a drag coefficient obtained from the NEMO model. Huang et al. (2019) showed that the bottom boundary layer thickness spatially varies between 15 and 123 m in the Atlantic Ocean, with a median of ~ 30-40 m in the North Atlantic. We define bottom layer thicknesses in our study area based on measured bathymetry from CTD-O_2 and near-bottom currents measurements from ADCP at stations. Here, u_b is the total velocity averaged over a thickness of 1520 m above the seabed for shallow stations and 40 m for deep stations.~~

The individual contributions of semi-diurnal ITs and mean circulation are then expressed as follows: ~~$E''/(E' + E'')$~~ $S^{2''}/(S^{2'} + S^{2''})$ for tidal contribution and $S^{2'}/(S^{2'} + S^{2''})$ ~~$E'/(E' + E'')$~~ for mean circulation contribution. ~~Here, $E = N*S$. N is the buoyancy frequency and S is vertical shear. S can be substituted by $S^{2''}$ and $S^{2'}$.~~

2.2.3 Ray tracing calculation

Analyzing both the mean currents and the spatial dimension along the IT pathways offers another insight into the mechanisms responsible for observed mixing (Rainville and Pinkel, 2006). IT energy rays are generated in regions with steep topography, such as the shelf break, where the IT slope matches with the bottom slope (i.e., critical slopes) before propagating within the ocean interior. These rays, moving both downward and upward, encounter the seasonal pycnocline, resulting in beam scattering and the formation of large IT oscillations. As these oscillations steepen, they disintegrate into nonlinear ISWs, a process known as "local generation" of ISWs (New and Pingree, 1992). To explore IT paths, ray-tracing techniques are employed, as previously used by New and Da Silva (2002) and Muacho et al. (2014), to investigate the effectiveness and expected pathways of the IT beams off the Amazon shelf. One main assumption in our linear-theory-based hypothesis is that stratification remains horizontally uniform along the IT propagation path, although in reality, it may vary due to submesoscale and mesoscale variability. This limitation makes the ray tracing approach less realistic but still useful as a first-order estimate of energy distribution. The IT ray-tracing calculation assumes that in a continuously stratified fluid, IT's energy can be described by characteristic pathways of beams (or rays) with a slope c to the horizontal:

$$c = \pm\left(\frac{\sigma^2 - f^2}{N^2 - \sigma^2}\right)^{1/2}, \quad (6)$$

where σ is the M_2 tidal frequency (1.4052 x 10^{-4} rad s^{-1}), and f is the Coriolis parameter. Here, N2 is the buoyancy frequency squared, which is calculated using the sorted potential density profiles (σ_θ). It is given by N2 = - (g/ρ0) (dσ_θ/dz), where ρ0 is

a reference density (1025 kg m-3) and g is the gravitational acceleration. N^2 is~~are~~ obtained from time-averaged AMAZOMIX CTD-O_2 data, glued with monthly N^2 profiles from Amazon36 (NEMO model outputs, 2012-2016) below 1000 m depth. Amazon36 is a specific configuration, specifically designed to cover the western tropical Atlantic from the mouth of the Amazon River to the open sea (see Tchilibou et al., 2022; Assene et al., 2024; for configuration details and model description). The NEMO model's fine horizontal resolution (1/36°) and 75 vertical levels allow for accurate simulation of low-mode ITs generated along the Brazilian shelf break. Key inputs include bathymetric data from the 2020 General Bathymetric Chart of the Oceans, surface forcing from ERA-5 atmospheric reanalysis (Hersbach et al., 2020), and river runoff data from the ISBA (Interaction Sol-Biosphère-Atmosphère; https://www.umr-cnrm.fr/spip.php?article146&lang=en) model. Open boundary conditions were driven by 15 major tidal constituents (M2, S2, N2, K2, 2N2, MU2, NU2, L2, T2, K1, O1, Q1, P1, S1, and M4) and barotropic currents from the FES2014 atlas (Lyard et al., 2021), supplemented by temperature, salinity, and velocity data from the MERCATOR-GLORYS12v1 assimilation product (Lellouche et al., 2018). ~~Amazon36 is a NEMO configuration, specifically designed to cover the western tropical Atlantic from the mouth of the Amazon River to the open sea (see Tchilibou et al., 2022; Assene et al., 2024; for configuration details and model description)~~.
Using N2 profiles from both Amazomix and Amazon36, IT ray-tracing diagrams are performed along the transects. The Upper (UTD) and Lower (LTD/LPD) Thermocline/Pycnocline Depth are delimited as defined by Assunçao et al. (2020). UTD corresponded to the depth where the vertical temperature gradient □□/□□ = 0.1 °C m-1, while LTD/LPD were the last depths below the UTD at which N2 ≥ 10-4 s-2. Seasonal sensitivity tests of rays (August, September, October, and April) are conducted by varying the critical slope positions and N^2 to explore its influence and generate a set of ray paths consistent with characteristics of IT pathways ~~(Figs. A6 and A7, Appendix)~~.

3 Results

3.1 Mixing

3.1.1 Thermohaline and IT features

In this subsection, we analyze density profiles (up-cast and down-cast) taken approximately six hours apart (half the M2 tidal period) along three transects (A^a, A^b, and E) defined on the HTE and LTE paths. Our aim is to examine the effects of mixing on water mass and the signatures of wave propagation.

First, mixing effects are evidenced in the step-like features of the density profiles (Fig. 4), indicating homogeneous layers. The vertical extent of these layers (L_{ρ_c}; Fig. 4b) is determined where the density gradient falls below the homogeneous threshold (0.01 kg m⁻³) between 60–180 m depth, ranging from 4 to 41 m. These step-like features are more pronounced along the HTE transects (A^a and A^b), with examples including 10 m at A^a_s, 41 m at $A^a_{o_2}$, 13 m at $A^a_{o_3}$, and 20 m at Aisw, compared to the LTE transect E, where they are smaller (e.g., 4 m at Es).

Second, wave propagation signatures are inferred from vertical displacements of isopycnals (constant density surfaces) between the two sampling times (Fig. 4c). Displacements range from 10 to 61 m across transects (Figs. 4a-4c). Along the 25 kg m⁻³ isopycnal, the largest shifts occur on the slope of transect A^a, with 40 m at A^a_s and 58 m at $A^b_{s_2}$, compared to 24 m at Es on transect E. Displacements are smaller in the open ocean (e.g., 16 m at A^b_o and 15 m at $A^a_{o_1}$), except at Aisw (34 m) and $A^a_{o_3}$ (52 m). These displacements generally occur between 60–170 m depth, corresponding to the thermocline layer.

The presence of step-like structures and relevant vertical isopycnal displacements indicates strong shear-driven mixing in the mid-water column. These findings support the hypothesis of IT propagation, with higher amplitudes along the HTE paths (A^a and A^b) and lower amplitudes along the LTE transect E.~~In this subsection, we analyze the density profiles to gain insight into mixing processes and/or wave propagation. Step-like features are observed in the density profiles (Figs. 3a and 3b). During the M2 tidal period, step-like structures ~20-40 m in length occur at depths ranging from 80 to 160 m at stations S10, S12, S13, and S14 (Fig. 3a). These features are more pronounced along the IN-ITs transect Aa and Ab compared to the other transects (e.g., E and G; Figs. A8.a and A8.b, Appendix).~~

~~In this layer (between 60 and 170 m depth), significant vertical displacements, ranging from 20 to 60 m, are detected along transects Aa, Ab, and E (e.g., 40 m at S10, 48 m at S6, 52 m at S13, and 32 m at S14; Figs. 3a and 3b). The smallest displacements (~8 m at S25) are observed along the OUT-ITs transect G (Fig. A8.b, Appendix). These vertical displacements are also evident in the variability of the mixed layer depth (MLD), which fluctuates between 18 and 84 m over a semi-diurnal cycle (figure not shown).~~

~~In conclusion, the presence of step-like structures and isopycnal displacements suggests strong mixing in the water column, and supports the hypothesis of ITs propagating, with stronger energy along transects Aa and Ab, weaker energy along D and E, and almost absent along G (Fig. 1a).~~

362 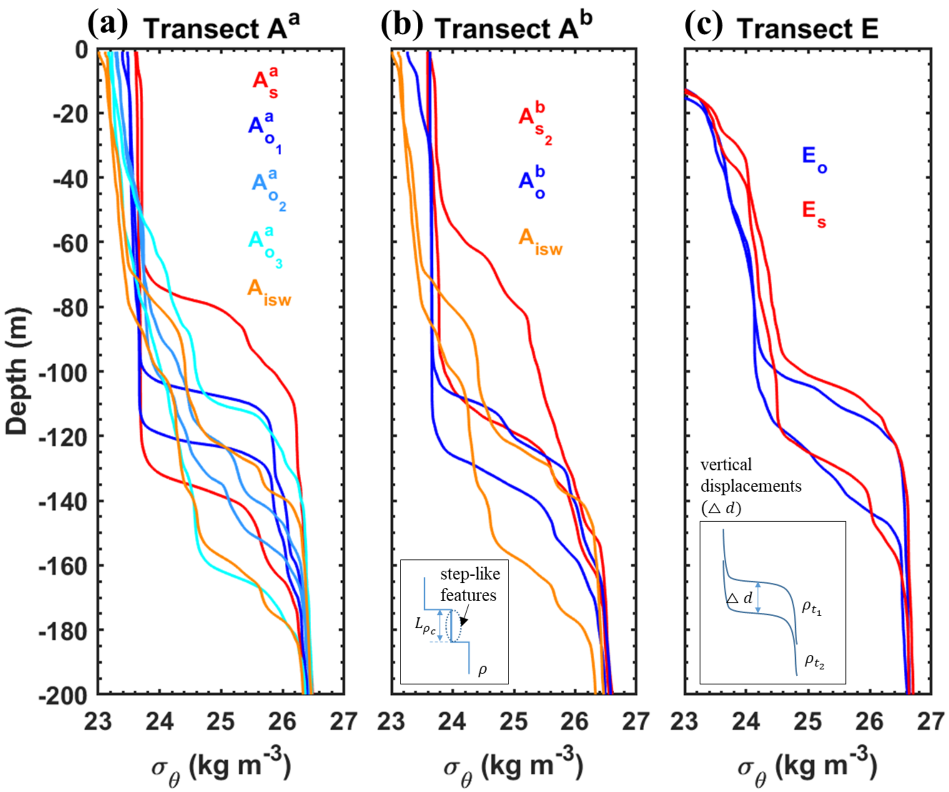

Formatted: Centered, Indent: Left: -0,01 cm, Right: 0,12 cm, Space After: 11,8 pt, Line spacing: Multiple 1,53 li

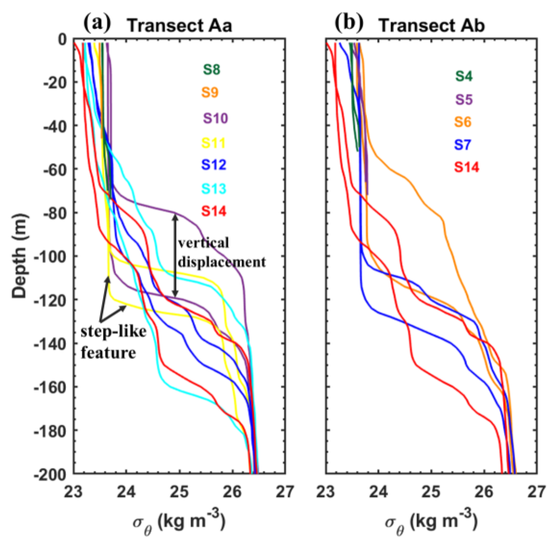

Figure 4~~3~~: Density profiles (σ_θ, kg m-3) from CTD-O2 measurements during the AMAZOMIX 2021 cruise along transects: (a) A^a, (b) A^b, and (c) E. For long stations ($A^b_{s_2}$, A^b_o, A^a_s, $A^a_{o_1}$, $A^a_{o_2}$, $A^a_{o_3}$, Aisw, Es, and Eo), two density profiles recorded ~6 hrs apart (half the M2 tidal period) are shown to highlight step-like structures and vertical isopycnal displacements along the transects. Colored lines represent stations on the slope (red) and open ocean (blue, sky-blue, cyan, and light-orange). The subpanel in panel b depicts a step-like structure, where L_{ρ_c} represents the vertical extent of homogeneous regions and ρc denotes the density structure. The subpanel in panel c illustrates vertical displacements (Δd) of density structures, with ρ_{t_1} and ρ_{t_2} representing density structures at times t1 and t2, respectively.~~Density profiles (σ_θ, kg m^{-3}) obtained from CTD-O$_2$ measurements during the AMAZOMIX 2021 cruise for stations S4 to S14 along transects (a) A_a and (b) A_b, located within IT fields. For long stations (S6, S7, and S10-S14), two density profiles are shown to highlight step-like structures and isopycnal vertical displacements (illustrated by black arrows) along the transects. Distinct colors are used to represent each station within each transect. The density values for stations S4, S5, S8, and S9 range between 23.4 and 23.8 kg m^{-3}~~.

Formatted: Subscript

Formatted: Subscript

3.1.2 TKE~~urbulent~~ dissipation rates and mixing

Following subsection 2.2, the vertical distribution of dissipation rates (ε) was estimated to examine the effects of mixing on water masses along transects A^a, A^b, and E. Station-averaged ε values, ranging from [10-10, 10-6] W kg-1, are presented in Figure 5.

Within the thermocline, the strongest ε values ([10-7, 10-6] W kg-1) are measured at slope stations ($A^b_{s_1}$, $A^b_{s_2}$, and A^a_s) of the HTE transects, whereas lower values ([10-9] W kg-1) are recorded at station Es (transect E). Elevated but relatively lower ε values ([10-8] W kg-1) are detected at open-ocean stations (e.g., A^b_o, $A^a_{o_2}$, and Eo) across all transects, except at station Aisw, where higher values ([10-7] W kg-1) are observed (Figs. 5a, 5c, and 5e).

Below the thermocline, elevated ε values ([10-8] W kg-1) persist at various depths at slope and open-ocean stations of the HTE transects (e.g., 375 m and 503 m for $A^b_{s_2}$; 390 m, 562 m, and 668 m for A^a_s; and 127 m and 192 m for A^b_o; Figs. 5a, 5c, and 5e), whereas on the LTE transect there is no evidence of such hotspots of mixing.

In the BBL, the highest ε values ([10-7] W kg-1) are found below 35 m depth at slope and shelf stations (A^b_{sh} and $A^b_{s_1}$) of transect A^b, while lower but still elevated values ([10-8] W kg-1) are observed at shelf stations of transects A^a and E (Figs. 5b, 5d, and 5f). Note that, at the base of MLD (between 15-30 m depth), elevated ε values (>10-7 W kg-1) are found at slope stations A^a_s and $A^b_{s_2}$, and open-ocean stations $A^a_{o_2}$ and A_{isw} compared to other stations (Figs. 5a and 5c).

In summary, the vertical distribution of ε exhibits distinct spatial patterns across transects A^a, A^b, and E. Slope stations of the HTE transects A^a and A^b show higher values than those of the LTE transect E. Open-ocean stations generally display lower but still elevated values, except for station Aisw, which has higher ε. The HTE transects A^a and A^b consistently exhibit higher ε than the LTE transect E, which could emphasize the role of localized shear-driven mixing along IT paths, particularly in the open ocean. To further investigate the processes driving mixing, we analyze shear instability arising from current dynamics.

~~Along the transects, we analyze the distribution of dissipation rates (ε) and vertical diffusivitymixing coefficient (K_z) estimated below the XLD (Table A1, Appendix) to characterize the mixing processes occurring off the Amazon shelf. It is important to note that the Defined XLD is typically deeper than the MLD at all stations (except at S8, S10, and S25), which is calculated using a density threshold 0.01, 0.02 or 0.03 kg m^{-3} (Fig. A2, Appendix).~~
~~Our results show that dissipation rates vary between [10^{-10}, 10^{-5}] W kg^{-1} from the continental shelf to the open sea (Fig. 4). Mapping the maximum value of ε over the water column (Fig. 4a) reveals that the strongest ε at the generation sites, within~~

~~the range of [10^{-6}, 10^{-5}] W kg^{-1}, occur at the IN-ITs transects except at E (S21), with even higher ε values found at the shelf-break (at stations S3, S5, and S10). Smaller ε values, within the range of [10^{-8}, 10^{-7}] W kg^{-1}, are observed away from the shelf-break (e.g., at S7, S9, S11, S19, S24, and S20), with the exception of some deep-sea stations (e.g., at S14 and S25) where ε are still high.~~

~~The vertical profile of ε (Figs. 4b and 4c, and Figs. A8c and A8d, Appendix) shows stronger dissipation (10^{-7}-10^{-6} W kg^{-1}), between 24-160 m depth, in the thermocline layers at stations on the shelf-break (S6 and S10) and in the open ocean (e.g., at S14, and S25). Hotspots of mixing, within the range of [10^{-8}, 10^{-7}] W kg^{-1}, are observed at various depths (e.g., 271 m and 375 m) at station S6, (e.g., 562 m, and 668 m) at S10, (e.g., 127 m, and 192 m) at S7 and (e.g., 138 m and 186 m) S24. For shelf/shallow stations within the ITs regions (S3 and S5; Fig. 4c, and Fig. A8.c, Appendix), mixing is more pronounced, between [10^{-6}, 10^{-5}] W kg^{-1}, near the bottom layer.~~

~~Similar to the dissipation patterns, higher K_z values are observed at IN-ITs stations (Figs. 4d and 4e, and Figs. A8e and A8f, Appendix), ranging from 10^{-3} to 10^{-1} m^2 s^{-1}, particularly in the upper layer (0-120 m) (e.g., at S6, S7, and S10), and also near the bottom layer (e.g., at S5, S8, and S9). Below 100 m depth, K_z decreases but remains significant, with values between [10^{-4}, 10^{-3}] m^2 s^{-1} (e.g., at S2, S10 S11, and S20). At OUT-ITs stations along transect G (Fig. A8f, Appendix), K_z reaches higher values (exceeding 10^{-4} m^2 s^{-1}) in the mixed layer (0-35 m) and below 200 m depth (at S25). Notably, the shallow station S3 exhibits the strongest mixing coefficient in this region, exceeding 10^{-0} m^2 s^{-1}.~~

~~In conclusion, the dissipation rates vary by 2-3 orders of magnitude over depth, with stronger mixing observed on the Amazon shelf and shelf-break compared to stations located farther from these areas. Additionally, the strongest mixing is observed in regions influenced by ITs. To further understand the heterogeneous distribution of ε, the next section will investigate the processes responsible for this variability, focusing on shear instability driven by the dynamics of the currents observed in this region~~.

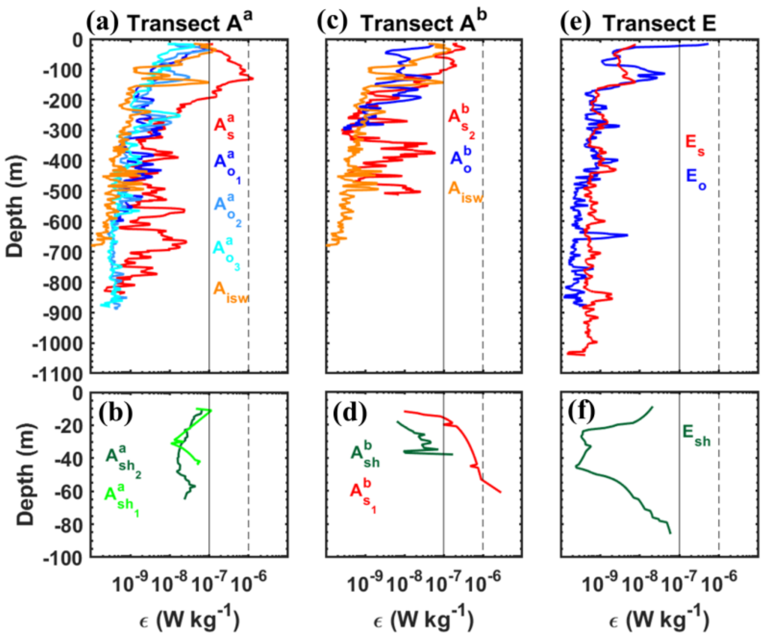

(a) Transcect A^a
(c) Transect A^b
(e) Transect E
Depth (m)
(b)
(d)
(f)
ϵ (W kg^-1)

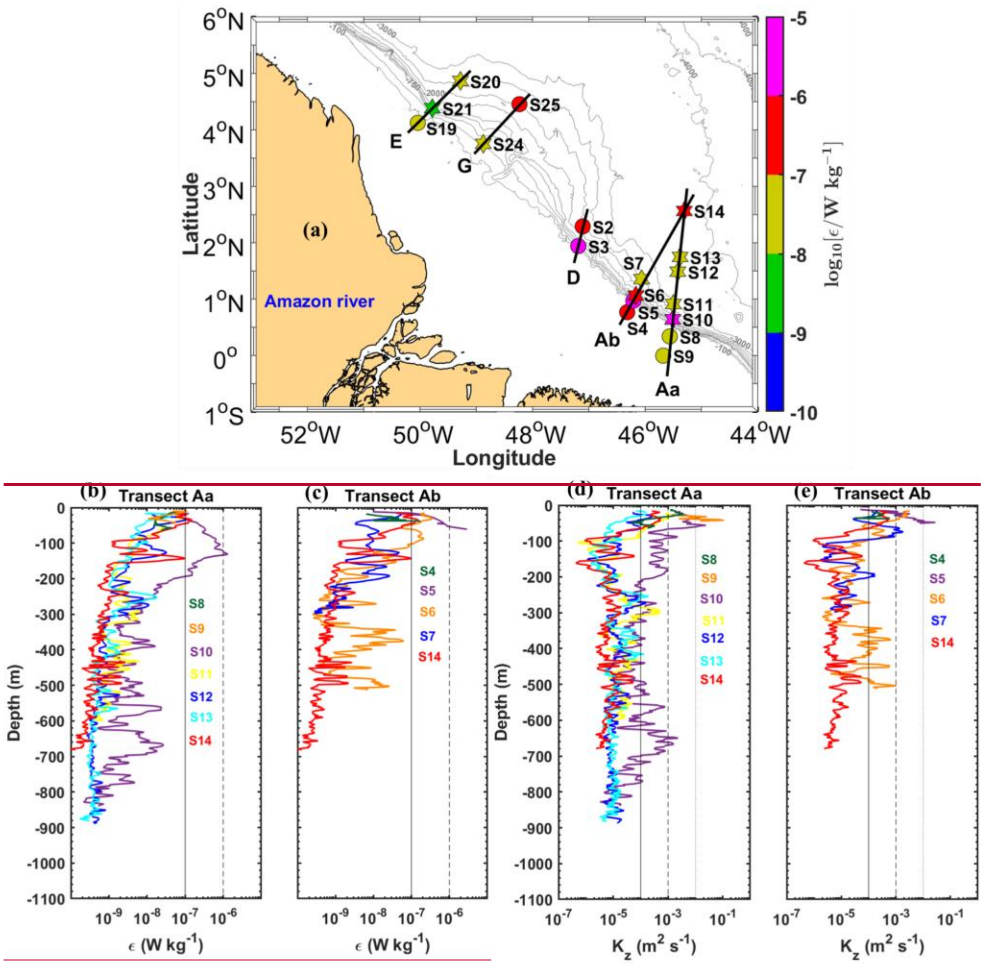

Figure 54: Station-averaged dissipation rate profiles (ε, in W kg-1, logarithmic scale) from VMP measurements during the AMAZOMIX 2021 cruise along transects: (a)-(b) A^a, (c)-(d) A^b, and (e)-(f) E. Colored lines represent stations on the shelf

(green, lime green), slope (red), and open ocean (blue, sky blue, cyan, and light orange). Vertical dashed and solid black lines are included for comparison.~~(a) Horizontal maximum dissipation rates (ε, in $W\ kg^{-1}$, on a logarithmic scale) measured with the VMP below the XLD during the AMAZOMIX 2021 cruise for all stations along transects Aa, Ab, D, E, and G. (b)-(c) Vertical dissipation profiles and (d)-(e) vertical diffusivity profiles (K_z, in $m^2\ s^{-1}$, on a logarithmic scale) for stations along transects Aa and Ab, respectively. Distinct colors are used to represent each station within each transect. Dashed and solid black lines in panels (b) to (e) are included for comparison purposes~~.

3.2 Processes contributing to mixing

In this subsection, we focus on the midwater layer, and we investigate the processes that might be responsible for the high mixing activity described in the previous section. In particular, we analyze the vertical structure of baroclinic currents and separate the contributions of baroclinic tidal currents and time-averaged currents (in the following mean currents) to dissipation. ~~In this subsection, we explore which processes among tides, general circulation, and friction are responsible for the high mixing activity observed off the Amazon shelf~~.

3.2.1 Mean baroclinic current

First, we focus on the mean baroclinic current. Following the method described in subsection 2.2.2 (Eqs. (1) and (5)), the vertical structure of the mean circulation is examined through the along-shelf components of the time-averaged (mean) baroclinic velocities. Indeed, the along-shelf current is the dominant component of the mean circulation in the region, primarily driven by the NBC. Note that the analysis of cross-shelf components does not alter the results (figures not shown). For three contrasting long stations–two on the HTE transects (A_s^{α} and A_{isw}; Figs. 6a, 6b, and 8a) and one on the LTE transect (E_o; Figs. 7a, 7b, and 9a)–we show the vertical structure of the along-shelf mean baroclinic currents and the associated mean shear.
In the upper 200 m (referred to as the surface layer), a northwestward surface flow is observed at all stations except at E_s, where the flow direction is reversed to southeastward. Strong surface flow velocities (67-98 cm s-1; Table A3, Appendix C) are recorded at all stations south of 3°N (e.g., at A_{isw}; Fig. 6b), except at A_s^{α}, where velocities are reduced (~30 cm s^{-1}; Fig. 6a). Strong vertical shear ([1.1, 1.7] × 10^{-4} s^{-2}; Table A3, Appendix C) is observed at stations south of 3°N (e.g., at A_{isw}; Fig. 8b), except at A_s^{α}, where shear is weaker ([10^{-5}] s^{-2}; Fig. 8a) in the surface layer. At stations further north (above 4°N) in the surface layer, lower along-shelf velocities are noted for both northwestward (~43 cm s^{-1} at E_o; Fig. 7a) and southeastward flows (~28 cm s^{-1} at E_s; Table A3, Appendix C). Strong vertical shear (2.7 × 10^{-4} s^{-2} at E_o; Fig. 8a) is associated with the northwestward flow, while lower vertical shear ([10^{-5}] s^{-2} at E_s; Table A3, Appendix C) is observed for the southeastward flow. Below 200 m, a potential subsurface flow is identified between 200-700 m, particularly at stations south of 3°N (e.g., A_s^{α}; Fig. 6a), with weak vertical shear ([10^{-5}] s^{-2}; Fig. 8a).

These findings suggest that the mean background circulation may play a substantial role in driving mixing mechanisms off the Amazon shelf.

3.2.1 Baroclinic tidal current

Second, we focus on baroclinic tidal currents. Following the method described in subsection 2.2.2 (Eqs. (3) and (4)), we examined the vertical structure of tidal currents using the cross-shelf components of semi-diurnal baroclinic velocities. The cross-shelf current is likely the dominant component of IT currents in the region. Note that the along-shelf velocity components were weaker than the cross-shelf components (figures not shown). For the same three contrasting long stations, we present time-depth sections of cross-shelf baroclinic tidal currents (Figs. 6c, 6d, and 7b) and their associated tidal shear (Figs. 8c, 8d, and 9b).

On the slope at A_s^a, strong tidal current reversals occur approximately every six hours within the pycnocline (70-180 m depth; 24–26 kg m^{-3} isopycnals; Fig. 6c), corresponding to the M_2 tidal component. These reversals reach amplitudes of up to 45 cm s^{-1} (Fig. 6c) and vertically exhibit 6-7 alternating velocity peaks, indicating high vertical eigenmodes (modes 6-7; Fig. 6c). Similar conditions are observed at $A_{s_2}^b$, where tidal amplitudes reach 35 cm s^{-1} (Table A3, Appendix C) with eigenmodes 6-7. In contrast, reduced amplitudes (20 cm s^{-1}) and slightly lower eigenmodes (mode 4) are recorded at Es. In the open ocean at E_o, tidal currents are weaker (up to 15 cm s^{-1}; Fig. 7b) with eigenmodes around mode 4. Other open-ocean stations ($A_{o_1}^a$, $A_{o_3}^a$, and A_o^b) show weak tidal amplitudes (15-25 cm s^{-1}; Table A3, Appendix C) and lower eigenmodes (modes 3-5). However, exceptions are noted at Aisw and $A_{o_2}^a$, where amplitudes remain high (40 cm s^{-1}; Table A3, Appendix C), particularly near the pycnocline.

On the slope, tidal vertical shear ranges between [1.2, 7.7] × 10^{-4} s^{-2}. The strongest shear (7.7 × 10^{-4} s^{-2}; Fig. 8c) occurs at A_s^a within the pycnocline, while the weakest (1.2 × 10^{-4} s^{-2}; Table A3, Appendix C) is at E_s. In the open ocean, shear varies between [2.0, 7.6] × 10^{-4} s^{-2} (Table A3, Appendix C), with lower values (3.5 × 10^{-4} s^{-2}; Fig. 9b) at E_o. Exceptions again occur at A_{isw} and $A_{o_2}^a$, where baroclinic tidal shear remains relatively strong (between [5.0, 7.6] × 10^{-4} s^{-2}; Fig. 8d; Table A3, Appendix C), particularly near the pycnocline.

Along the slope, baroclinic tidal currents and shear are stronger along the HTE transects compared to LTE. In the open ocean, they are generally weaker, except at A_{isw} and $A_{o_2}^a$, where they remain high. These tidal currents and their associated shear coincide with strong vertical displacements of *N²* maxima (subsection 3.1.1) and high dissipation rates (subsection 3.1.2), raising the question of whether high mixing activity is primarily driven by IT or mean currents.

~~The contribution of ITs to the baroclinic velocity structure is analyzed using the time series of baroclinic tidal currents (Figs.~~

~~The baroclinic tidal velocities reveal a superposition of 3-5 tidal modes at IN-ITs stations (Figs. 5a, 5c, and 5e, and Figs. A9 to A15, Appendix). A greater number of modes is observed near the shelf-break (e.g., 4 modes at S6 and 5 modes at S10), while fewer modes are detected far from (e.g., 3 modes at S7, S12 and S14). Higher tidal velocities ranging from 25-50 cm s^{-1} are found between 80-350 m along transects Aa and Ab (e.g., at S6, and S10). In contrast, lower tidal velocities, typically below 25 cm s^{-1}, are more pronounced along transect E (e.g., at S20, and S21) to OUT-ITs stations along transect G (e.g., at S24).~~

~~Consistent with the tidal signal patterns, the strongest vertical tidal shear, reaching up to 10^{-3} s^{-2} is observed at IN-ITs stations where the large vertical displacements in N^2 maxima are detected (e.g., S6, S10, and S14), except at S7, S11, S20, and S21 (Figs. 6a, 6c, and 6e, and Figs. A16 to A18, Appendix). These latter stations, and the OUT-ITs station S24, exhibit lower but still notable shear, reaching to 10^{-4} s^{-2}. Dissipation rates, previously presented in subsection 3.1.2 and shown in Fig. 4, are found to be 2-3 orders of magnitude higher in the pycnocline compared at greater depths.~~

~~The analysis of baroclinic tidal currents reveals significant contributions from ITs, particularly in the pycnocline, with strong vertical shears observed near the shelf-break. Dissipation rates are notably higher in the pycnocline than at greater depths, especially in regions influenced by ITs. These findings underscore the role of internal tides in driving mixing processes in the Amazon shelf area~~.

Commented [1]: rajouter E

Commented [1]: rajouter E

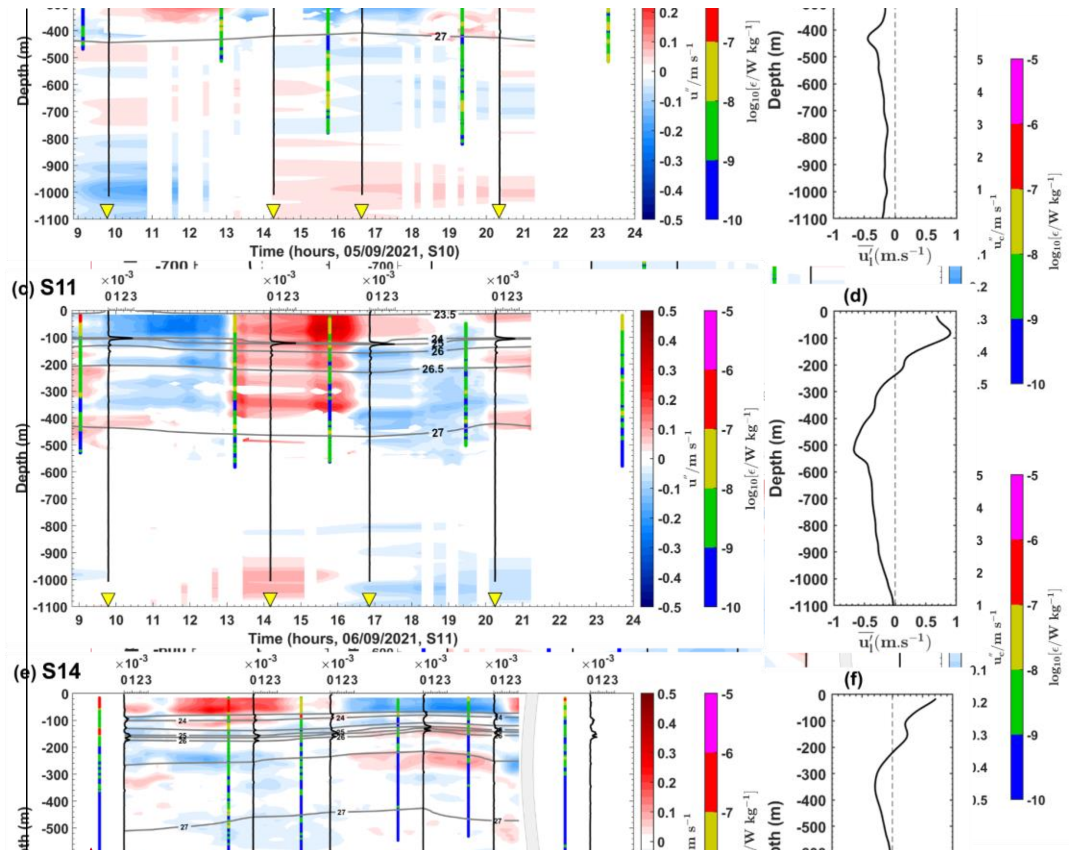

Figure 6~~5~~: (a)-(b) Along-shelf mean baroclinic currents (u'_l, in m s-1) and (c)-(d) cross-shelf semi-diurnal baroclinic currents (u''_c, in m s-1) from the ADCP for stations (a)-(c) A_s^a and (b)-(d) Aisw. Panels (c) and (d) also show the buoyancy frequency squared (N2, in s-2) as vertical black lines, potential density (σ_θ, kg m-3) as grey contours, and dissipation rate profiles (ε, in W kg-1, logarithmic scale) as vertical colored bars.

Formatted: Font: 12 pt

Formatted: Font: 12 pt

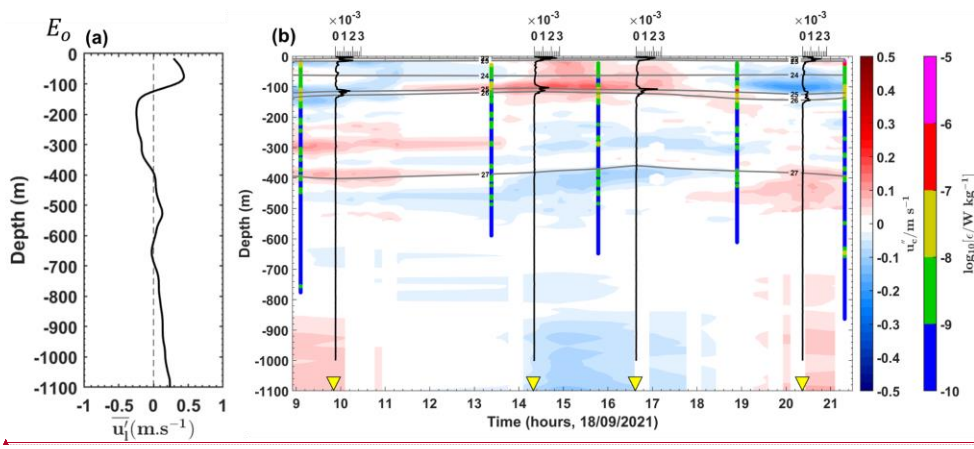

Figure 7: Panels follow the same format as in Figure 6 but correspond to station Eo.

~~Semi-diurnal baroclinic zonal currents (*u*'', in m s-1) from the ADCP for stations (a) S10, (c) S11, and (e) S14. Panels (a), (c),~~

Formatted: Font: Not Italic

Formatted: Font: Not Italic

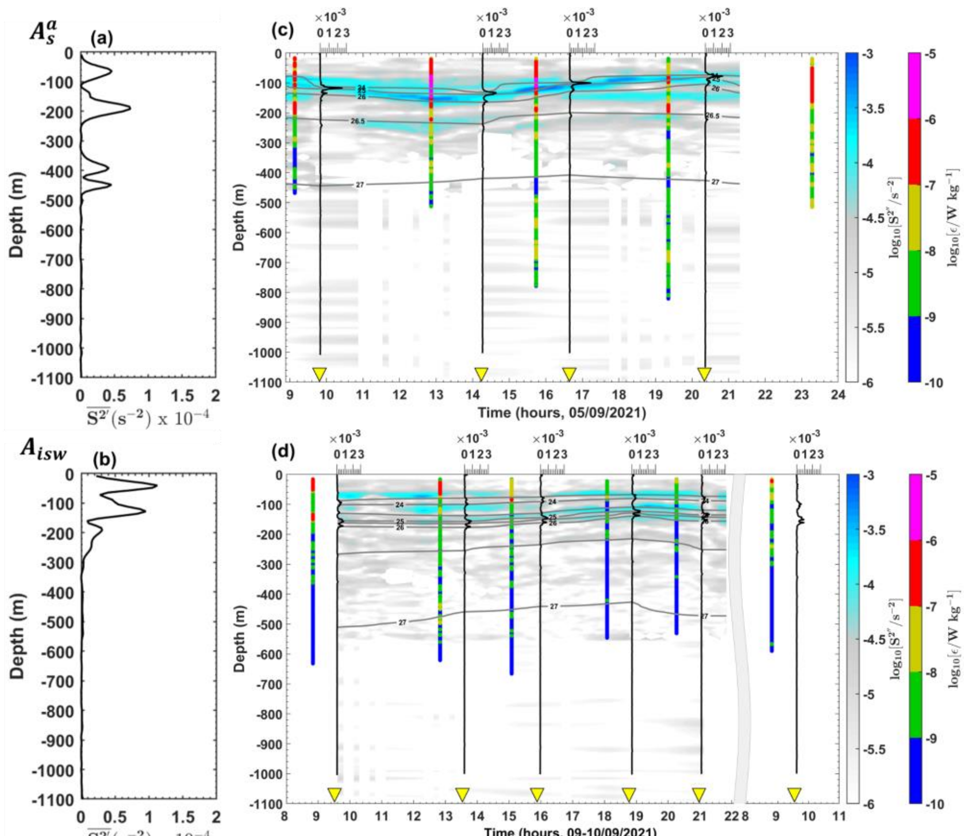

A_s^a
(a)
Depth (m)
$\overline{S^{2'}}(s^{-2})$ x 10^{-4}
A_{isw}
(b)
Depth (m)
$\overline{S^{2'}}(s^{-2})$ x 10^{-4}
(c)
Depth (m)
Time (hours, 05/09/2021)
(d)
Depth (m)
Time (hours, 09-10/09/2021)
$\times10^{-3}$
$\log_{10}[S^{2'}/s^{-2}]$
$\log_{10}[\epsilon/\mathrm{W\ kg^{-1}}]$

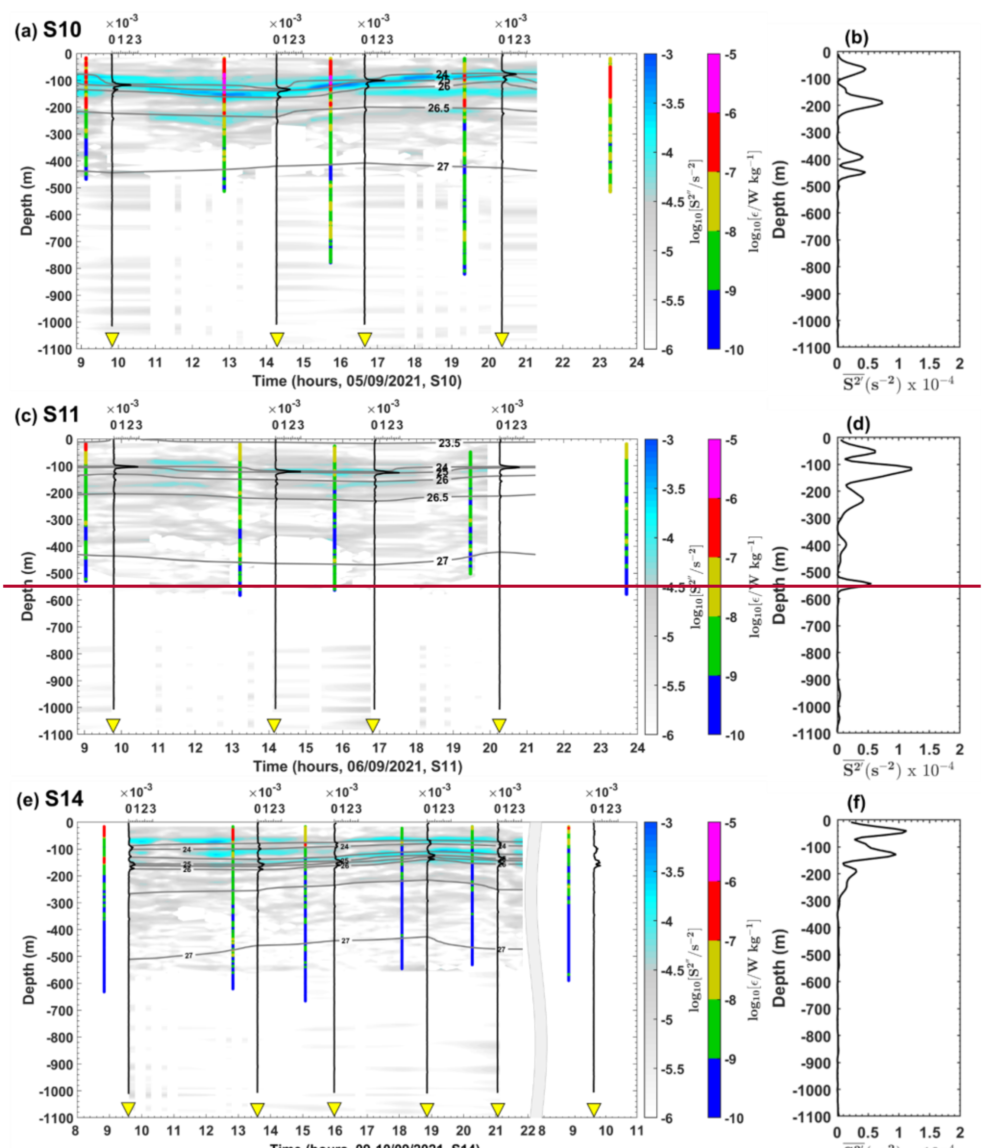

(a) S10
(b)
(c) S11
(d)
(e) S14
(f)
$\times10^{-3}$
0123
Depth (m)
Time (hours, 05/09/2021, S10)
Time (hours, 06/09/2021, S11)
Time (hours, 09-10/09/2021, S14)
$\log_{10}[S^{2'}/s^{-2}]$
$\log_{10}[\epsilon/\mathrm{W\ kg^{-1}}]$
$\overline{S^{2'}}(s^{-2})$ x 10^{-4}
23.5
24
26
26.5
27

Figure 8~~6~~: (a)-(b) Mean baroclinic vertical shear squared ($\overline{S^{2\prime}}$, in s^{-2}) and (c)-(d) semi-diurnal baroclinic vertical shear squared ($S^{2''}$, in s^{-2}, logarithmic scale) from the ADCP for stations (a)-(c) A_s^a and (b)-(d) Aisw. Panels (c) and (d) also show the buoyancy frequency squared (N2, in s-2) as vertical black lines, potential density (σ_θ, kg m-3) as grey contours, and dissipation rate profiles (ε, in W kg-1, logarithmic scale) as vertical colored bars.

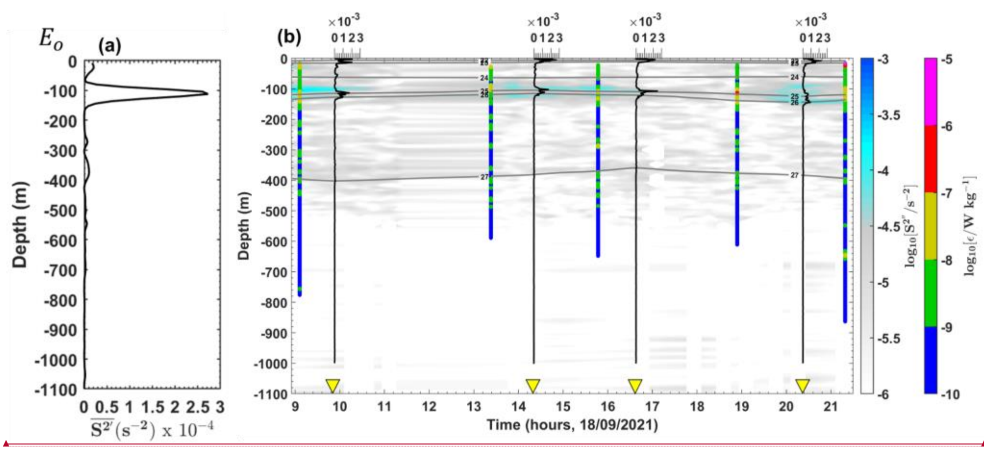

Figure 9: Panels follow the same format as in Figure 8 but correspond to station Eo.

~~Semi-diurnal baroclinic vertical shear squared ($S^{2''}$, in m s-21, on a logarithmic scale) for stations (a) S10, (c) S11, and (e) S14. Panels (a), (c), and (e) also display the buoyancy frequency squared (N2, in s-2) represented by vertical black lines,~~

~~**3.2.2 Mean baroclinic current**~~

~~The contribution of the mean baroclinic current is diagnosed through the across- and along-shore components of mean baroclinic velocities, defined parallel and perpendicular to the 200 m depth isobath, respectively, as proxies for the main circulation patterns in the region. Along-shelf velocities are defined as positive northwestward and negative southeastward, while across-shelf velocities are positive northeastward and negative southwestward (Figs. 5b, 5d, and 5f, and Figs. A9 to A15, Appendix).~~

~~A strong surface flow is observed crossing transects Aa and Ab (e.g., at S6, S7, S11-S14), with along-shore northwestward velocities exceeding 68 cm s-1 in the upper layer of 200 m (Fig 5, and Figs. A9, A10, A12, A13, A14, and A19, Appendix).~~

Formatted: Font: Not Italic

Formatted: Font: Not Italic

Formatted: Font: Not Italic

Formatted: Font: Not Italic, Not Superscript/ Subscript

Formatted: Font: Not Italic

Formatted: Font: Not Italic, Not Superscript/ Subscript

Formatted: Font: Not Italic

Formatted: Font: Not Italic, Not Superscript/ Subscript

Formatted: Font: Not Italic

Formatted: Not Superscript/ Subscript

~~This flow is notably stronger compared to the across-shore velocities and decreases in strength with depth, transitioning towards the subsurface layer. Below 200 m depth along transects Aa and Ab, a southeastward along-shore flow emerges with velocities below 30 cm s-1, but increases up to 50 cm s-1 between 400 and 550 m depth at stations S6, S7, and S11. This southeastward baroclinic flow becomes weakly unstable at IN-ITs stations S13 and S14 below 500 m depth.~~

~~Similar dominant along-shore flows are observed along transect G (Figs. A11, A15, and A19, Appendix). At the OUT-ITs station S24, northwestward velocities reach up to 50 cm s-1 above 80 m depth, while southeastward velocities below 80 m remain weaker (< 30 cm s-1).~~

~~Above 4°N along transect E, the flow directions reverse throughout the water column, with the along-shore component dominating (Figs. A11, A15, and A19, Appendix). In the upper layer of 120 m, the along-shore flow is stronger (~ 45 cm s-1) and directed northwestward at S20, while at S21, it is weaker and shifts southeastward. Below this layer, between 120–400 m depth, the flows become more unstable and opposing, with the along-shore velocities being stronger (~28 cm s-1) at S21 compared to S20.~~

~~The mean baroclinic flows exhibit various peaks of mean shear instability, ranging from 10-5 to 10-3 s-2, in the first 600 m depth along transects (Figs. 6b, 6d, and 6f, and Figs. A16 to A18, Appendix). Vertical shear is more pronounced within the range of [0.5, 1.5] x 10-4 s-2 around the pycnocline, between 40 and 200 m depth along transects Aa, Ab and G (e.g., at S6, S7, S10, S11, S14, and S24). This shear strength increases further along transects E, reaching up to 2.5 x 10-4 s-2 at the base of the pycnocline, around 112 m depth at S20~~.

3.2.3 Competitive processes to generate mixing

Our aim in this subsection is to associate midwater mixing events with either baroclinic tidal currents or time-averaged (mean) currents. To achieve this, we map depth-integrated and maximum values of station-averaged ε and plot all ε values on a (time-mean shear $S^{2\prime}$, tidal shear $S^{2''}$) diagram across five regions (As, Ao, Aisw, Es, and Eo; Figs. 10 and 11). These regions are selected to contrast slope and open-ocean dynamics, with data included from the HTE and LTE transects. All data are collected from below the wind-influenced surface layer (defined as the maximum of XLD or MLD; see subsection 2.2.1) and above the friction-dominated bottom boundary layer (HBBL; defined in subsection 2.2.1).

Mixing hotspots (ε = [10-6, 10-7] W kg-1; magenta and red circles in Fig. 11 and Fig. 10) are observed under strong vertical baroclinic shear ([10-4, 10-5] s-2), driven by either tidal or time-mean currents.

On the slope (As and Es), high ε values in As are associated with stronger $S^{2''}$ than $S^{2\prime}$ (magenta, red, and grey stars in Fig. 11a correspond to $S^{2''}$ ≈ 10-4 > $S^{2\prime}$ ≈ 10-5), indicating that tidal shear explains ~60% of high ε values (Table A3, Appendix

Formatted: Not Superscript/ Subscript
Formatted: Not Superscript/ Subscript
Formatted: Not Superscript/ Subscript
Formatted: Not Superscript/ Subscript
Formatted: Not Superscript/ Subscript
Formatted: Not Superscript/ Subscript
Formatted: Not Superscript/ Subscript
Formatted: Not Superscript/ Subscript
Formatted: Not Superscript/ Subscript
Formatted: Not Superscript/ Subscript
Formatted: Not Superscript/ Subscript
Formatted: Not Superscript/ Subscript
Formatted: Not Superscript/ Subscript
Formatted: Right: 0,12 cm
Formatted: Not Superscript/ Subscript
Formatted: Not Superscript/ Subscript

C). Similarly, in Es, moderate ε values (yellow and grey stars in Fig. 11d) are primarily driven by tidal shear, which accounts for ~60% of the observed mixing (Table A3, Appendix C).

In the open ocean (Ao, Eo, and Aisw), moderate ε values in Ao and Eo are found when $S^{2''}$ is nearly equal to $S^{2'}$ (yellow, red, and grey stars in Fig. 11b and 11e correspond to $S^{2''} \approx S^{2'} \approx$ 10-4 s-2), suggesting tidal and time-mean shear each contribute ~50% to mixing (Table A3, Appendix C). An exception is observed in Aisw, where high ε values coincide with slightly stronger tidal shear (red and grey stars in Fig. 11c correspond to $S^{2''} \approx 2$ x $S^{2'} \approx 2$ x 10-4 s-2), suggesting that tidal shear explains ~60 % of mixing hotspots (Table A3, Appendix C).

These results suggest that mixing on the slope is slightly dominated by ITs, while offshore mixing is equally balanced by mean circulation and ITs. However, exceptions exist in the open ocean, particularly at stations Aisw and A_o^b, where tidal shear contributes ~60% and ~30% to mixing, respectively. The mixing at A_o^b is attributed to NBC. A key question remains: why does Aisw exhibit strong IT-driven mixing ~230 km from IT generation sites, with mixing hotspots observed at various depths throughout the water column? To address this, we employ ray-tracing techniques to investigate potential IT propagation paths.

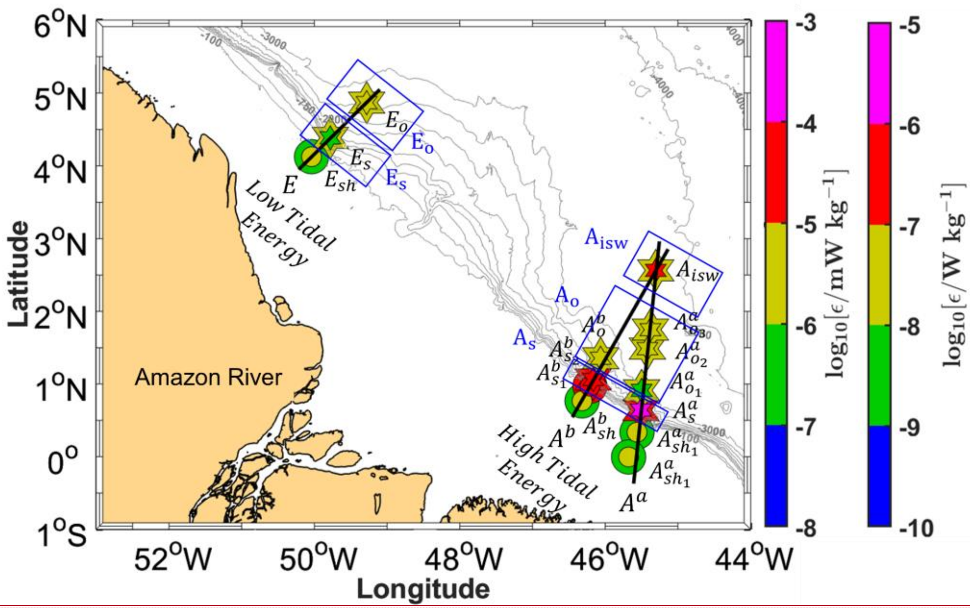

Formatted: Font color: Auto, Not Superscript/ Subscript

Formatted: Font color: Auto

Formatted: Not Superscript/ Subscript

Formatted: Not Superscript/ Subscript

Formatted: Not Superscript/ Subscript

Formatted: Not Superscript/ Subscript

Formatted: Not Superscript/ Subscript

Formatted: Font color: Auto

Formatted: Font color: Auto

Formatted: Font color: Auto

Formatted: Font color: Auto

Formatted: Font color: Auto

Formatted: Font color: Auto

Figure 10: Depth-integrated (in mW kg-1, logarithmic scale) and maximum values (in W kg-1, logarithmic scale) of station-averaged dissipation rates (ε) from VMP measurements during the AMAZOMIX 2021 cruise. Solid black lines depict transects (A^a, A^b, and E) along high tidal energy (HTE) and low tidal energy (LTE) paths. Data are from below the wind-influenced surface layer and above the friction-dominated bottom boundary layer. Colored circles and stars represent short and long stations, respectively. Small and large colored circles indicate depth-integrated and maximum values of ε, respectively, with ranges shown by the color bar. Similarly, small and large colored stars indicate depth-integrated and maximum values of ε, respectively, with ranges shown by the color bar. Stations are grouped into five areas: As (A_s^a and $A_{s_2}^b$), Ao (A_o^b, $A_{o_1}^a$, $A_{o_2}^a$, and $A_{o_3}^a$), Aisw (Aisw), Es (Es), and Eo (Eo). The five blue boxes indicate these defined areas. Subscripts denote locations: "s" for slope (As), "o" for offshore (Ao and Eo), and "isw" for ISW regions (Aisw).

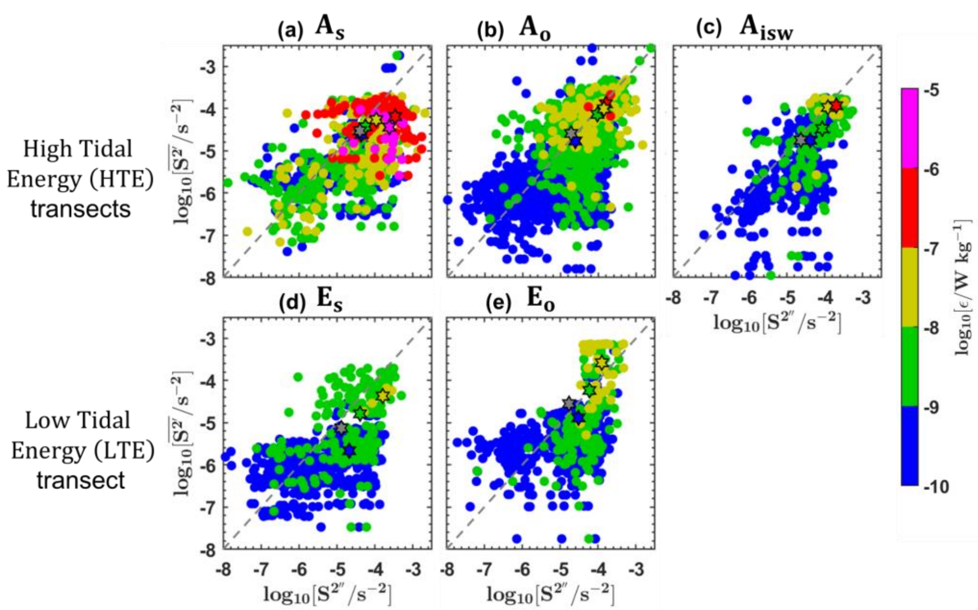

~~Our aim is to distinctly associate each mixing event with either tidal activity or time-averaged currents. To achieve this, we~~

~~Along the transects (Fig. 7, and Figs. A20 and A21, Appendix), stronger mixing, with ε ranging between [10-7, 10-5] W kg-1, occurs at stations S6 and S10. At these locations, there is significant stratification (N^2 exceeding [10-5, 10-3] s-2), strong tidal shear ($S^{2''}$ within [10-4, 10-3] s-2), and low gradient Richardson number (Ri < 0.25).~~

~~In contrast, at stations S7, S11, S13, and S14, mixing events with similar ε values are observed under comparable stratification conditions but with relatively weaker tidal shear and higher Ri (ranging from 0.25 to 1). Stations S12, S20, S21, and S24 show lower dissipation rates, reaching up to [10-8] W kg-1. These values are found in regions with significant stratification (N^2 exceeding 10-4 s-2) and Ri > 1.~~

~~This analysis reveals that vertical tidal shear is sufficiently strong at stations S6 and S10 to overcome stratification and generate hotspots of mixing. At stations S7, S11, S13, and S14, the tidal shear is comparatively weaker, and it is even less pronounced at S12, S20, S21, and S24, limiting its ability to cross stratification and generate mixing.~~

~~When comparing the influence of mean shear $\underline{S}^{2\prime}$ with mixing events, we observe that stronger $\underline{S}^{2\prime}$, within the range [10-5, 10-3] s-2, aligns with mixing hotspots characterized by dissipation rates between [10-8, 10-5] W kg-1 along the transects (e.g., at S7, S11, and S14). This suggests that the baroclinic mean shear also plays an significant role in driving mixing in the water column.~~

~~To better clarify which of the tidal vs mean vertical shear is dominating to explain the hotspots of mixing, we compare the contribution of $S^{2''}$ and $\underline{S}^{2\prime}$ to the total vertical shear (Table A1, Appendix).~~

~~Along transects Aa and Ab, tidal shear exhibits a stronger contribution relative to mean shear ($S^{2''}$/$\underline{S}^{2\prime}$) at specific shelf-break locations: (61.4/38.6% %) at S6, (65.8/34.2% %) at S10, and (58.5/41.5% %) at S21. This contribution decreases a few kilometers from these locations, with minimums observed at S7 (47.6% %) and S11 (48.2% %). Interestingly, along transect Aa, tidal shear contribution rises from 48.2% % at S11 to 58.5% % at S14 in the open ocean. Conversely, along transect E, it decreases from 58.5% % at S21 to 52.1% % at S20. Overall, tidal and mean shear contributions are nearly equal (~ 50/50% %) away from the shelf-break and along the OUT-ITs transect G (e.g., at S24), except at S14, where tidal shear remains dominant.~~

~~These contributions to the total shear instability support the hypothesis that mixing is dominated by ITs on the shelf-break, by both the mean circulation and ITs away from the shelf-break and far IT fields.~~

Formatted: Not Superscript/ Subscript

Formatted: Not Superscript/ Subscript

Formatted: Not Superscript/ Subscript

Formatted: Not Superscript/ Subscript

Formatted: Not Superscript/ Subscript

Formatted: Not Superscript/ Subscript

Formatted: Not Superscript/ Subscript

Formatted: Not Superscript/ Subscript

Formatted: Not Superscript/ Subscript

Formatted: Not Superscript/ Subscript

Formatted: Not Superscript/ Subscript

Formatted: Not Superscript/ Subscript

Formatted: Not Superscript/ Subscript

Formatted: Not Superscript/ Subscript

Formatted: Not Superscript/ Subscript

Formatted: Not Superscript/ Subscript

Formatted: Not Superscript/ Subscript

Formatted: Not Superscript/ Subscript

Formatted: Not Superscript/ Subscript

Formatted: Not Superscript/ Subscript

Formatted: Indent: Left: 0 cm, Right: 0 cm, Space Before: 12 pt, After: 12 pt

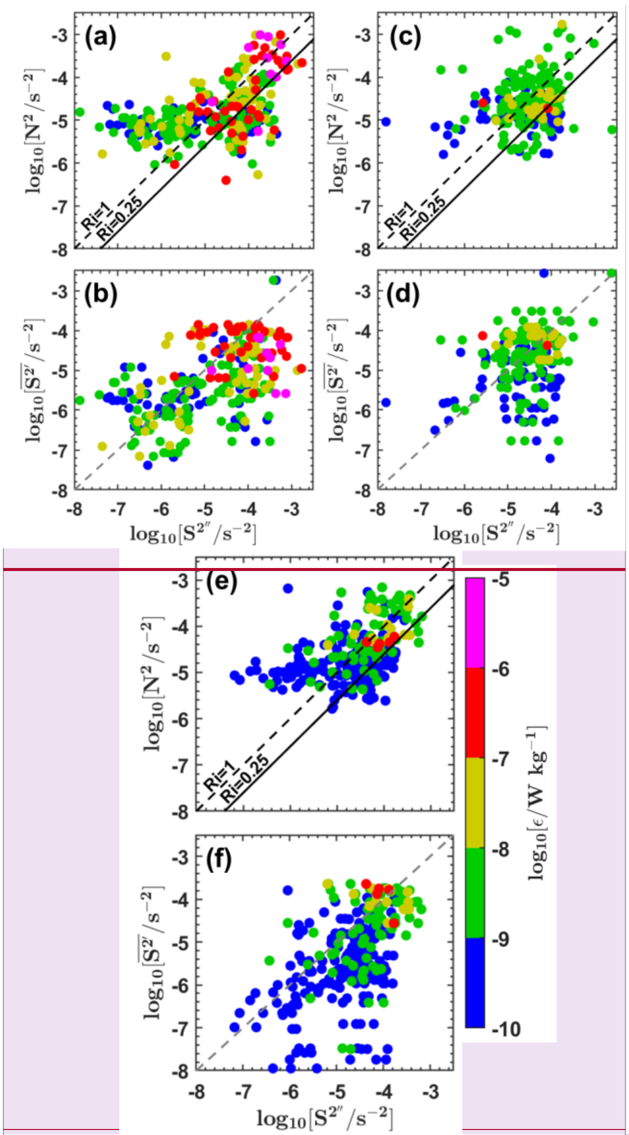

Commented [2]: rajouter station sur chaque subplot

Figure 11~~7~~: Dissipation rates (ε, in W kg-1, logarithmic scale), measured below the wind-influenced surface layer (max [XLD, MLD]) and above the friction-dominated BBL (HBBL), plotted as a function of the mean baroclinic vertical shear squared ($\underline{S}^{2\prime}$, in s-2, logarithmic scale) and semi-diurnal baroclinic vertical shear squared ($S^{2''}$, in s-2, logarithmic scale). Data are from defined areas: (a) A_s (A_s^a and $A_{s_2}^b$), (b) A_o (A_o^b, $A_{o_1}^a$, $A_{o_2}^a$, and $A_{o_3}^a$), (c) A_{isw} (A_{isw}), (d) E_s (E_s), and (e) E_o (E_o). ε are represented by colored circles, with their ranges indicated on the color bar. Each panel also includes vertical shear averages for specific ε ranges ([10^{-6}], [10^{-7}], [10^{-8}], [10^{-9}], and [10^{-10}] W kg^{-1}), depicted as colored stars with black edges, grey stars with black edges represents the vertical shear averaged across all ε values. Dashed grey lines are included for comparison.~~Dissipation rates (ε, in W kg⁻¹, on a logarithmic scale) below the XLD as a function of the buoyancy frequency squared (N^2, in s^{-2}, on a logarithmic scale) and semi-diurnal baroclinic vertical shear squared ($S^{2''}$, in m s^{-1}, on a logarithmic scale) for stations (a) S10, (c) S11, and (e) S14. Dissipation rates (ε, in W kg^{-1}, on a logarithmic scale) below the XLD as a function of mean baroclinic vertical shear squared ($\underline{S}^{2\prime}$, in m s^{-1}, on a logarithmic scale) and semi-diurnal baroclinic vertical shear squared ($S^{2''}$, in m s^{-1}, on a logarithmic scale) for stations (b) S10, (d) S11, and (f) S14. N^2 was linearly interpolated into the depths of $S^{2''}$ to have the same vertical scales. Panels (a), (c), and (e) also display two solid black lines corresponding to Richardson number Ri = 0.25 and Ri = 1, respectively. Dashed grey lines in panels (b), (d), and (f) are included for comparison purposes.~~

Commented [3]: a corriger

Commented [4]: ok.

3.2.4 IT ray-~~-~~tracing

In this subsection, IT ray paths are computed for the M_2 tidal frequency, following the method described in subsection 2.2.3 (Eqs. (6)). These computations provide insights into linear theoretical energy flux paths in the vertical dimension (Rainville and Pinkel, 2006). The results will be compared to previously estimated dissipation rates to explain the intense mixing hotspot observed at Aisw, which contrasts with values typically found in the open ocean (Gille et al., 2012).

Figures 12 and 13 show that linear IT rays, derived from both model and observed density data, are generated at the critical slope near the 93 m and 121 m isobaths on the HTE and LTE transects, respectively. After generation, the rays propagate downward through the water column, reflect at the seabed, and then propagate upward, where they are expected to reflect at the surface. This pattern continues seaward (Figs. 12 and 13). In reality, part of the IT beam may also reflect within the pycnocline. Surface reflections are observed at large distances from the ray generation sites: ~105 km and ~230 km on transect A^a (Fig. 12a) and ~100 km and ~220 km on transect A^b (Fig. 12b). These large distances may result from the greater orientation angle between the IT propagation direction and the transects. In contrast, surface reflections on transect E occur at shorter distances (~80 km and ~205 km; Fig. 13), possibly due to eddy activity (Dosssa et al.,). The linear rays suggest horizontal wavelengths of ~90–125 km, consistent with mode-1 IT. Differences between transects may arise from variations in density, ocean depth, or the angle between the IT propagation path and the transect orientation. The curvature of the rays becomes more pronounced as they interact with the pycnocline, particularly between 20–207 m depth, defined by the upper and lower thermocline depths (UTD and LTD; Figs. 12 and 13).

Tracking the IT rays along the transects reveals their possible alignment with mixing hotspots (Figs. 12 and 13). On the slope, mixing hotspots (between 60-180 m depth; Fig. 12a-b) at A_s^a and $A_{s_2}^b$ likely result from their proximity to the ray generation sites. In the open ocean, the surface mixing (at 34 m depth; Fig. 12a) at $A_{o_2}^a$ may arise from surface reflections of the rays. Meanwhile, mixing hotspots between 130–152 m depth at Aisw could result from either ray interference creating instabilities at multiple depths or the arrival of rays from transect A^a (at 87 m and 150 m depth; Fig. 12a) and transect A^b (at 275 and 523 m depth; Fig. 12b) at Aisw.

~~An alternative approach to understanding the two primary processes driving the observed mixing is to examine the vertical profiles of the mean total currents (both along- and across-shore), with the spatial dimension along the transects of IT ray propagation. For this analysis, IT ray paths are computed for the M2 tidal frequency, with the rays for September illustrated along the ITs-IN transects (Aa, Ab, D, and E).~~

~~IT rays are generated at the critical slope, located between 32-104 km from the coast on the Amazon shelf-break (Figs. 8, and Figs. A6, A7, A22 and A23, Appendix). These rays propagate downward into the deep ocean, where they first reflect within a depth range of 1250-3900 m and at distances between 54-222 km. After bottom reflection and subsequent interaction with the pycnocline, the rays are expected to reflect seaward at the surface, typically at distances between 115-400 km. The curvature of the rays becomes more pronounced as they interact with the pycnocline, particularly between 20-207 m depth, defined by the upper (UTD) and lower (LTD) thermocline depths.~~

~~Along transects Aa and Ab (Fig. 8, and Figs. A6 and A22, Appendix), the total along-shore flow is stronger in the upper layer of 150 m, with velocities exceeding 80 cm s^{-1} (observed at S6, S7, S10, and S11). This flow becomes unstable between 150-185 km from the ray generation along transect Aa, and between 200-450 km and 500-1000 m depth along both transects Aa and Ab. In contrast, along transect E, the first 100 m depth reveals an opposing surface and subsurface along-shore flow at stations S20 and S21, with flow instability occurring between 120-500 m depth (Figs. A7 and A23, Appendix).~~

~~Tracking the IT rays along the transects (Fig. 8, and Figs. A6, A7, A22 and A23, Appendix), hotspots of mixing are identified where ray paths potentially interfere with each other or with the mean flow. Mixing are observed at various depths, including the surface, between 70-180 m, and below 300 m along transects Aa (e.g., at S10, S12, S14) and Ab (e.g., at S6). Stronger~~

~~mixing, ranging from [10^{-7} to 10^{-5}] W kg^{-1}, is observed near the ray generation site (e.g., at S5, S6, and S10), as well as along the ray paths (e.g., at S14) along transects Aa and Ab, compared to transect E.~~

~~These findings suggest that turbulent dissipation occurs along the IT ray paths, particularly where the rays interfere with one another and interact with the strong mean background circulation.~~

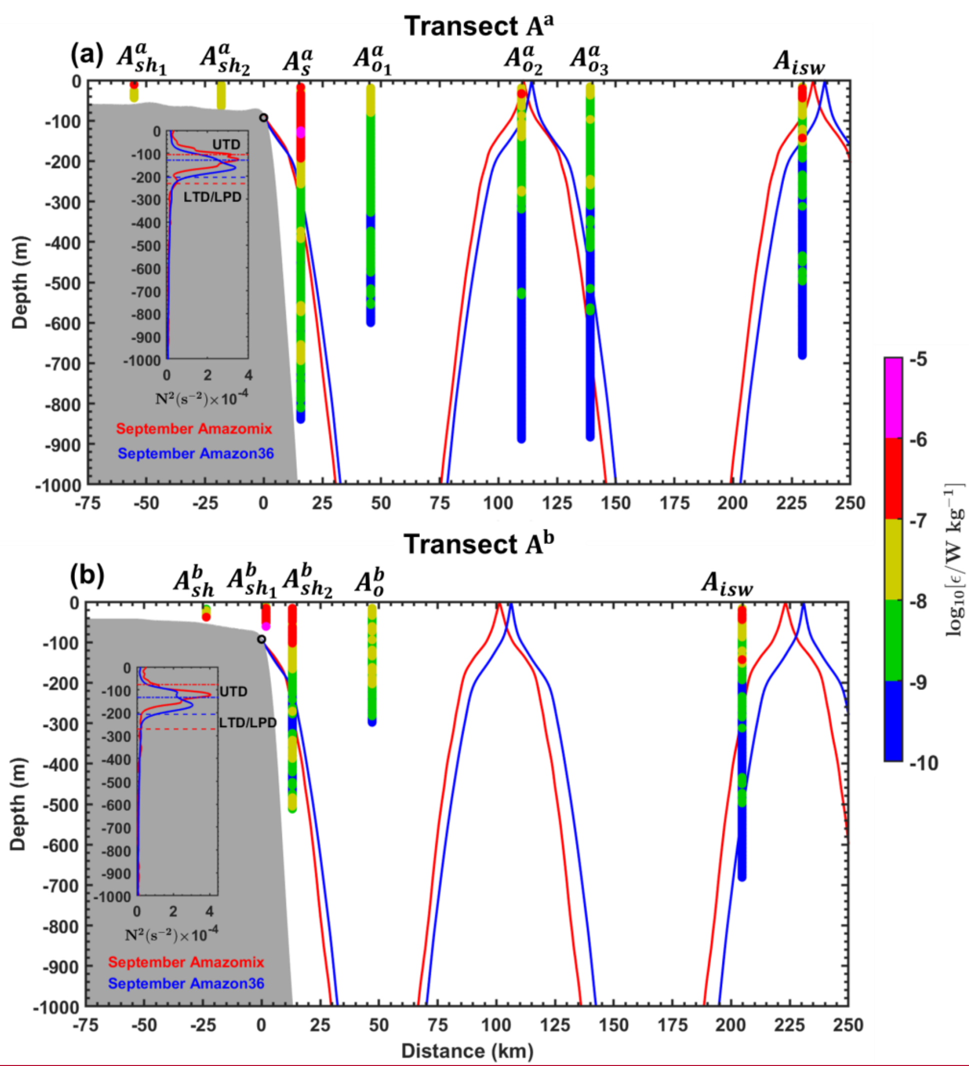

Transcect A^a
(a)
$A^a_{sh_1}$
$A^a_{sh_2}$
A^a_s
$A^a_{o_1}$
$A^a_{o_2}$
$A^a_{o_3}$
A_{isw}
UTD
LTD/LPD
September Amazomix
September Amazon36
Depth (m)
Transect A^b
(b)
A^b_{sh}
$A^b_{sh_1}$
$A^b_{sh_2}$
A^b_o
A_{isw}
Distance (km)
$N^2(s^{-2})\times10^{-4}$
$\log_{10}[\epsilon/\mathrm{W\ kg^{-1}}]$

671

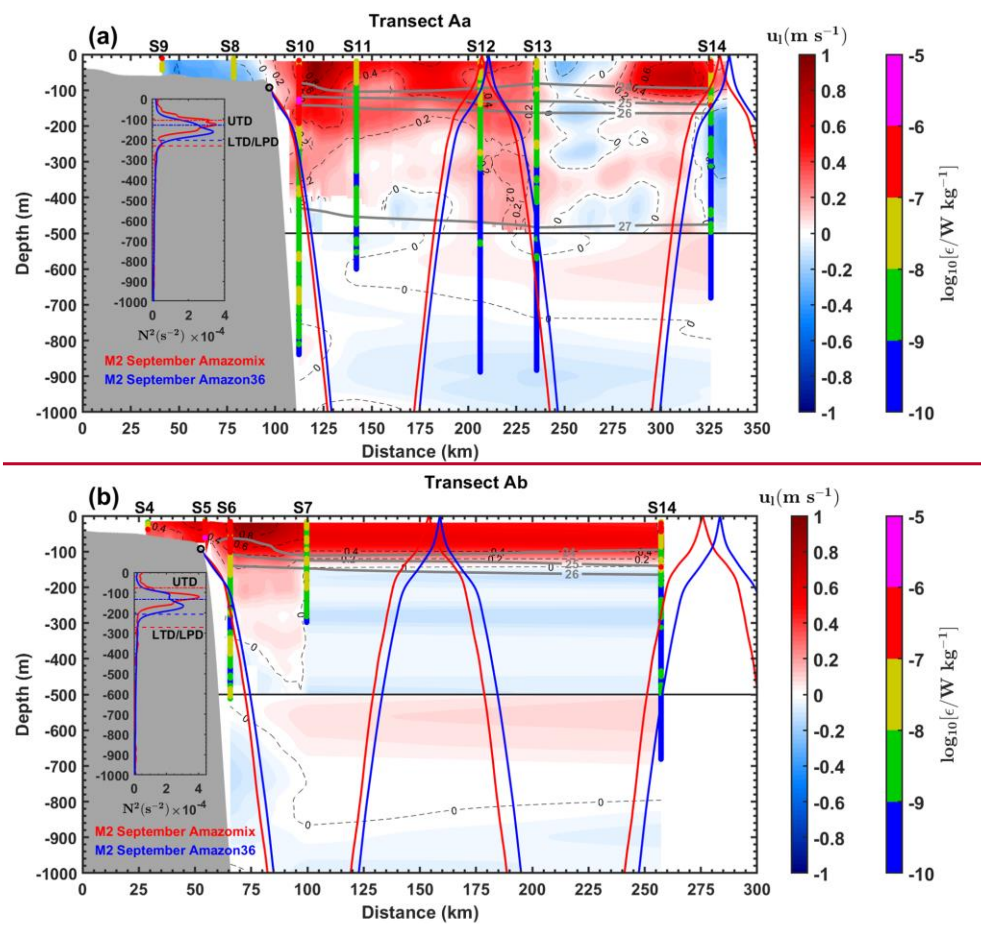

Figure 12~~8~~: Ray-tracing diagrams for M_2 constituent of IT~~IT ray-tracing diagrams for the M2 tidal constituent~~ along transects (a) A^a and (b) A^b~~(a) Aa and (b) Ab~~. Ray~~The~~ calculations were performed using the mean buoyancy frequency squared (N^2, in s^{-2}) derived~~obtained~~ from CTD-O_2 data (red ray~~ray in red~~) and NEMO-Amazon36 model data (blue ray~~ray in blue~~) for

September. Grey areas represent local topography, and black circles indicate the critical topography slopes (ray generation sites). ~~*Panels (a) and (b) also show along the transects Aa and Ab: along-shore mean total currents (u_t, in m s^{-1}) from ADCP (Dashed black lines), potential density from CTD-O_2 (grey contours), and dissipation rate profiles (ε, in W kg^{-1}, on a logarithmic scale) from the VMP (vertical colored bars).*~~ *Subpanels show*~~*within each panel illustrate the*~~ *N^2 profiles from AMAZOMIX (red line) and the NEMO-Amazon36 model (blue line), used for ray-tracing calculations. Upper Thermocline Depth (UTD, dotted lines) and Lower Thermocline/Pycnocline Depth (LTD/LPD, dashed lines) are also indicated in the subpanels.*

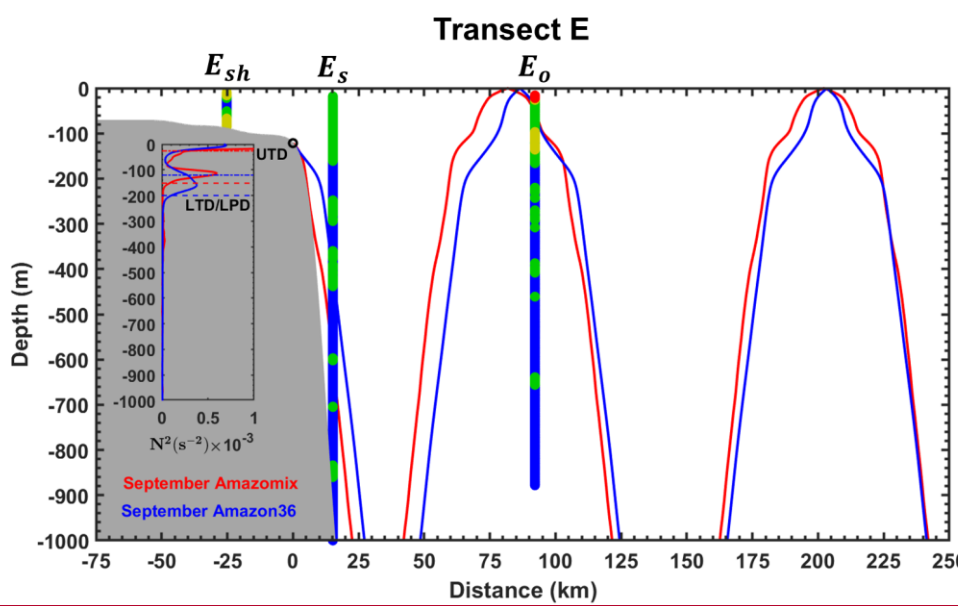

Figure 13: Panels follow the same format as in Figure 12 but correspond to transect E.

4 Discussion and Conclusion

The AMAZOMIX 2021 cruise provided, to the best of our knowledge, for the first time, direct measurements of turbulent dissipation using a ~~velocity microstructure profiler (~~VMP~~)~~ at multiple stations along contrasting IT paths~~both inside and outside the influence of ITs~~. These measurements enabled the study of mixing processes at the Amazon Shelf break and the

Formatted: Font: Not Italic

Formatted: Font: Not Italic

adjacent open ocean. To capture a full tidal cycle, data on turbulent dissipation rates, hydrography, and currents were collected alternately over 12 hours, with 4 to 5 profiles taken per station (see section 2). The locations of the 12-hour sampling stations were selected based on modeling results that provided realistic maps of IT generation, propagation and dissipation (Fig. 1~~1a~~; Tchilibou et al., 2022). Stations were located along the HTE paths A^a and A^b ($A^a_{sh_1}$ $A^a_{sh_2}$, A^a_s, $A^a_{o_1}$, $A^a_{o_2}$, $A^a_{o_3}$, Aisw, A^b_{sh}, $A^b_{s_1}$, $A^b_{s_2}$, and A^b_o) and LTE path E (Esh, Es, and Eo).~~Stations were located in the most energetic regions of IT, specifically at sites Aa, Ab, and D, covering stations S2 to S14, as identified in previous studies (Magalhaes et al., 2016; Tchilibou et al., 2022; Assene et al., 2024). Stations S19 to S21 were positioned in less energetic IT generation areas at site E, while stations S24 and S25 were located outside the influence of the IT fields (site G). Stations were distributed across different areas, including the shelf (e.g., S4, S9, and S19), the shelf-break (e.g., S3, S6, and S10), and the open ocean (e.g., S14, S24, and S20).~~

Vertical d~~D~~isplacements, homogeneous layers

First, step-like features were found in the density profile that characterized homogenized layers stacked atop one another, indicating intense mixing hotspots at various depths in the water column. Their vertical extent ranged between 4 and 41, consistent with step-like structures observed in other IT regions (Nash et al., 2007; Koch-Larrouy et al., 2015; Bouruet-Aubertot et al., 2018). Our results show that along the HTE paths (A^a and A^b), step-like structures were larger in the open ocean (up to 41 m) than over the (up to 10 m). In contrast, along the LTE path (E), they were smaller (4 m) and uniform across both the slope and open ocean, indicating weaker mixing.

Second, vertical isopycnal displacements ranged from 10 to 61 m, aligning with observations from other IT regions (Stansfield et al., 2001; Simpson and Sharples, 2012; Bordois, 2015; Koch-Larrouy et al., 2015; Zhao et al., 2016; Bouruet-Aubertot et al., 2018; Xu et al., 2020) that show similar order of magnitude. On the HTE paths, the strongest displacements occurred over the slope (up to 58 m), with substantial variability in the open ocean (15–52 m). On the LTE path, displacements were weaker (24 m) and confined to the slope.

The differences between the open ocean and slope, as well as between HTE and LTE paths, are seemingly associated with IT propagation, which induces vertical displacements at tidal frequencies, promoting mixing and forming the step-like density features observed. ~~The results revealed that, over a semi-diurnal tidal cycle, relevant amplitudes of vertical displacements (up to 60 m in length) and pronounced step-like structures (up to 40 m thick) were observed along transects Aa and Ab. In contrast, smaller and thinner structures were identified along other transects, such as E. These differences are likely related to the propagation of ITs, which induce vertical displacements at tidal frequencies and promote mixing by creating homogeneous layers visible as step-like features in the density structure. The isopycnal displacements and step-like structures observed within the pycnocline are consistent with findings from other IT regions (e.g., Stansfield et al., 2001; Simpson and Sharples, 2012; Bordois, 2015; Koch-Larrouy et al., 2015; Zhao et al., 2016; Bouruet-Aubertot et al., 2018; Xu et al., 2020). Furthermore, IT~~

~~propagation appears to have stronger energy along transects Aa and Ab compared to others, consistent with prior modeling studies (Tchilibou et al., 2022; Assene et al., 2024).~~

Direct measurements of dissipation rates

The station-averaged dissipation rate (ε) ranged from 10-10 to 10-6 W kg-1, with distinct spatial patterns across paths A^a, A^b, and E. The highest ε values (10-7 to 10-6 W kg-1) were observed at slope stations of the HTE paths, while lower ε values (10-9 W kg-1) were found at slope stations of the LTE path (Figure 14). Open ocean ε values were generally lower (10-8 W kg-1) but still elevated, especially at Aisw, where values reached 10-7 W kg-1 near the pycnocline. The elevated ε near slopes on the HTE paths aligns with observations from other energetic IT generation sites (e.g., the Hawaiian Ridge, Klymak et al., 2008; Halmahera Sea, Koch-Larrouy et al., 2015; Bouruet-Aubertot et al., 2018). In contrast, lower ε values near slopes on the LTE path are comparable to those in less energetic IT regions (e.g., Takahashi and Hibiya, 2019). In the open ocean, ε values–though lower than slope measurements–remain elevated, particularly at Aisw, where they exceed typical background levels (10-10-10-8 W kg-1; e.g., Southern Ocean, Gille et al., 2012; Banda Sea, Bouruet-Aubertot et al., 2018). This suggests localized turbulent mixing, likely driven by ITs or mesoscale currents.

~~Dissipation rates measured with the VMP ranged from between [10^{-10}, 10^{-5}] W kg^{-1} below the XLD, spanning from the continental shelf to the open ocean.~~

~~The highest dissipation rates, within [10^{-6}, 10^{-5}] W kg^{-1}, were observed primarily at generation sites Aa, Ab, and D (e.g., at stations S6, S10, and S3), as represented for A region in Fig. 9 (red zigzags). Slightly lower but still substantial dissipation rates, ranging from 10^{-8} to 10^{-7} W kg^{-1}, occurred a few kilometers (~40 km) from these generation sites (e.g., at S11 and S7), along IT pathways (e.g., at S12, S13, and S20), and even in regions farther from IT influence (e.g., at S24). Interestingly, dissipation rates were higher within [10^{-7}, 10^{-6}] W kg^{-1} in the open ocean, such as at station S14, located ~230 km from generation site Aa, as summarized in Fig. 9 (orange zigzags).~~

~~Using dissipation measurements, we calculated the XLD, defined as the depth where the dissipation rate drops from its first minimum value. The XLD was found to be greater than the MLD at all stations except S8, S10, and S25. This exception may reflect larger mixing events at those stations that were not captured during the VMP deployment. For the other, it is consistent with regions exhibiting strong subsurface shear, such as the Equatorial Ocean and western boundary current areas (Noh and Lee, 2008).~~

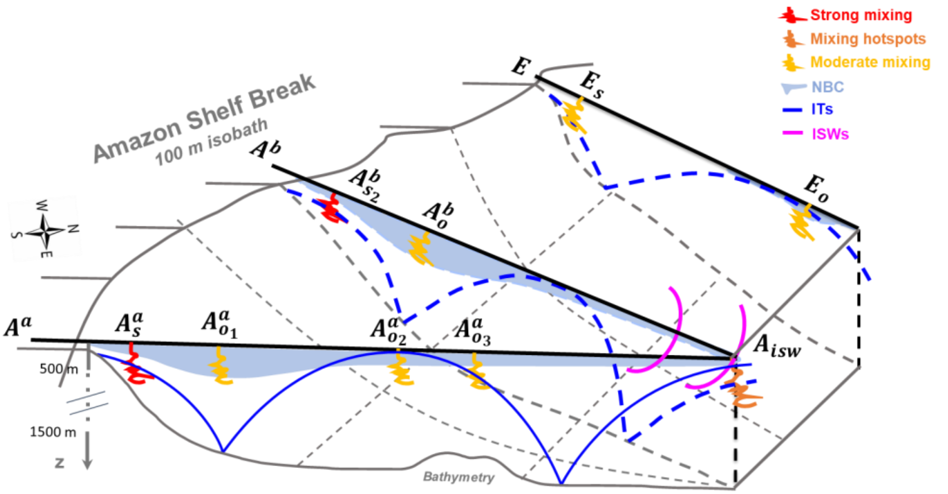

748

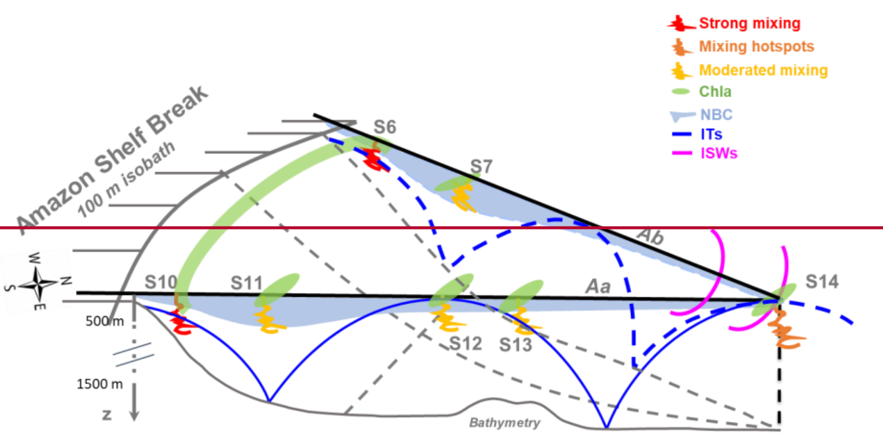

749

750

Formatted: Indent: Left: 0 cm, Right: 0 cm, Space Before: 12 pt, After: 12 pt, Line spacing: Multiple 1,54

Figure 14~~9~~: Summary diagram illustrating the key processes driving mixing across the HTE paths (A^a and A^b) and LTE path (E) off the Amazon shelf. At IT generation sites (stations A^a_s, $A^b_{s_2}$, and E_s), mixing is generally stronger (red zigzags), except at Es, where it is moderated (yellow zigzags). At these generation sites, ITs contribute ~60% of the mixing, exceeding the contribution of the mean circulation (NBC). Away from generation sites in the open ocean (e.g., A^b_o, $A^a_{o_1}$, and Eo; yellow zigzags), mixing decreases but remains substantial, driven by nearly equal contributions from ITs and mean circulation. A key observation is the increased mixing ~230 km from the generation sites, forming a hotspot at Aisw (orange zigzags). This coincides with the surfacing of IT rays (blue lines) from two distinct generation sites on the HTE paths, the vanishing of the NBC (sky-blue shaded areas), and the presence of ISWs (magenta lines). These observations suggest that constructive interference of IT rays may generate ISWs, amplifying mixing at Aisw.~~summary diagram illustrating the key processes driving mixing along the AMAZOMIX transects (e.g., Aa and Ab). At IT generation sites (e.g., S6 and S10; red zigzags), mixing rates are stronger, with ITs contributing around 65%, compared to mean circulation (NBC). Along IT pathways (e.g., S7 and S11; yellow zigzags), mixing decreases but remains notable, driven by nearly equal contributions from ITs and mean circulation. A key observation is the increased mixing ~ 230 km from two distinct IT generation sites at the shelf break. This hotspot at S14 (orange zigzags) coincides with the surfacing of IT rays (blue lines) from different sites, vanishing of the NBC (sky blue shaded areas) and the presence of ISWs (magenta lines), suggesting possible constructive interferences of IT rays may generate ISWs, amplifying mixing at S14. IT mixing observed close enough to the surface at these sites could influence the chlorophyll content (green shaded areas) off the Amazon shelf.~~

~~In other regions, dissipation rates exhibit values comparable to those observed in this study. For instance, at IT generation sites (S6 and S10), dissipation rates align with the range of [10^{-7}, 10^{-5}] W kg^{-1} reported for the Halmahera Sea, Indonesia (Koch-Larrouy et al., 2015; Bouruet-Aubertot et al., 2018), Kaena Ridge, Hawaii (Klymak et al., 2008), and the Changjiang Estuary (Yang et al., 2020). Conversely, along IT pathways off the Amazon shelf (e.g., S11 and S7), dissipation rates are higher ([10^{-8}] W kg^{-1}) than those documented in other regions, such as [10^{-10}, 10^{-8}] W kg^{-1} in the Southern Ocean (Gille et al., 2012) and the Halmahera Sea (Bouruet-Aubertot et al., 2018), that might be due to the cumulative effect of IT and NBC mixing and/or to their interaction that might intensified the local mixing. Lastly, in the open ocean, elevated dissipation rates were observed compared to previous studies. For instance, values of [10^{-9}, 10^{-8}] W kg^{-1} around 100 m depth at S25 were higher than values of [10^{-11}, 10^{-10}] W kg^{-1} reported by Takahashi and Hibiya (2019) for sites far from IT influence and under geostrophic current conditions. This discrepancy may be attributed to the strong mean background circulation investigated off the Amazon shelf (Dossa et al., in preparation).~~

~~Our study also found the highest dissipation rates at stations S3 and S5 of [10^{-6}, 10^{-4}] W kg^{-1} on the Amazon shelf, increasing near the bottom boundary layer. These findings compare well with values reaching up to 10^{-9} W kg^{-1} within a kilometer of the seabed in the Southern Ocean (Sheen et al., 2013) and up to 10^{-6} W kg^{-1} within a few meters from bottom topography off the Changjiang Estuary (Yang et al. 2020). This may indicate the presence of an active bottom boundary layer. Thus, kinetic energy of bottom flow was estimated using friction velocity, that was computed from total velocity averaged over the bottom-most 15 m for shallow stations. It showed bottom friction energy stronger between 16-35 J m^{-2} at S3 and S5 mainly and lower (< 3 J m^{-2}) in the other stations on shelf (e.g., at S8). These results are smaller but still important on the Amazon shelf and comparable to values (517 kJ m^{-2}) in the Drake Passage region (on the continental slope) of the Southern Ocean (Laurent et al., 2012). The bottom mixing at S3 and S5 can indirectly exert a control on pycnocline mixing on the Amazon shelf (Inall et al., 2021).~~

~~Enhanced surface mixing~~

~~The vertical eddy diffusivity coefficients were highest at the shelf break (e.g., at S3, S5, and S10), ranging from 10^{-3} to 10^{-0} m^2 s^{-1}. Away from the shelf break, diffusivity values were lower but remained substantial, within the range of 10^{-4} to 10^{-3} m^2 s^{-1} (e.g., at S2, S7, and S11). These mixing coefficients align with values reported in other regions. For instance, vertical diffusivity falls within the range of 10^{-5} to 10^{-3} m^2 s^{-1}, as observed in the Luzon Strait (Tian et al., 2009), the Indonesian Sea (Koch-Larrouy et al., 2015; Bouruet-Aubertot et al., 2018), and the southern Yellow Sea (Xu et al., 2020).~~

~~Close to the surface, mixing coefficients remained significant, reaching up to 10^{-3} m^2 s^{-1} between 100-200 m depth and up to 10^{-2} m^2 s^{-1} above this layer at stations S6 and S10. These surface values are of the same order of magnitude as, but slightly higher than, those reported for the Halmahera Sea, Indonesia (Koch-Larrouy et al., 2015; Bouruet-Aubertot et al., 2018). In the open ocean, under the influence of ITs, mixing near the surface reached 10^{-4} m^2 s^{-1} at S14.~~

~~This elevated vertical eddy diffusivity close enough to the surface along IT paths may play a critical role in modulating heat transfer (e.g., Assene et al., 2024) and chlorophyll distribution (see green shaded areas in Fig. 9) (de Macedo et al., 2023; M'Hamdi et al., in preparation) observed off the Amazon shelf, as documented in the Indonesian region (Nugroho et al. 2018; Koch-Larrouy et al., 2010; Sprintall et al., 2014; Zaron et al., 2023).~~

Enhanced mixing at the base of the MLD

Near the base of the MLD (15–30 m depth), high ε values (>10^{-7} W kg^{-1}) were observed at slope stations (A_s^a and $A_{s_2}^b$) and open-ocean stations ($A_{o_2}^a$ and Aisw) along the HTE paths. These findings agree with model results from Tchilibou et al. (2022) and Assene et al. (2024), which identified similar near-surface ε hotspots in the HTE regions.

Contribution of b~~B~~ackground circulation and ITs to mixing

To identify the processes driving the observed high mixing activity, we analyzed shear instabilities in both mean and semi-diurnal baroclinic currents and quantified their relative mixing contributions.

Mean baroclinic current shear

First, we analyzed the along-shelf component of the mean baroclinic current (MBC), as it dominates the mean circulation in the region. MBC was primarily observed in the surface layer (0-200 m depth), driven by a northwestward flow with strong velocities (67-98 cm s-1) and shear instability (between [1.1, 1.7] × 10-4 s-2) at all stations south of 3°N. This flow is associated with the NBC, which moves northwestward along the Brazilian coast (Bourlès et al., 1999; Johns et al., 1998; Schott et al., 2002). However, at slope station A_s^a, NBC velocities were lower (~30 cm s-1) with weak NBC vertical shear (~10-5 s-2), likely due to topographic effects that weaken NBC near the continental slope (Silveira et al., 1994). Further north (above 4°N), the surface layer exhibited weak MBC with low shear instability (~10-5 s-2) in the open ocean, except near the slope, where MBC reversed to southeastward with strong shear (2.7 × 10-4 s-2). This reversal could be related to subsurface eddy activity (Dossa et al., in preparation) and the retroflection of the NBC, both common features in the region (Goni & Johns, 2001; Fratantoni et al., 1995). Below the surface layer (200-700 m depth), a potential southeastward flow beneath the NBC was observed, with weak shear instability (~10-5 s-2), particularly near the slope south of 3°N (e.g., at A_s^a). This flow may be associated with a subsurface countercurrent (Dossa et al., in preparation).~~Another important aspect addressed in this study was quantifying the contributions of different processes to the observed heterogeneous mixing.~~

~~First, we analyse the mean baroclinic current (BC), a proxy for the background circulation. The BC was predominantly structured into a northwestward surface flow and a southeastward subsurface flow along the IT pathways. The strong surface flow toward the northwest is associated with the North Brazil Current (NBC), which originates from the northeastern coast of Brazil (e.g., Bourlès et al., 1999) and propagates along the Amazon shelf-break (e.g., at stations S7, S10, S11, S14, and S24). Conversely, the southeastward subsurface flow observed at stations such as S7 and S11 might result from NBC instability or the presence of a countercurrent at depth (Dossa et al., in preparation). At site E, the flow reversal observed at S21 - characterized by a southeastward surface flow and a northwestward subsurface flow - was located inside of the outer path of the Amazon plume. This reversal could be related with the influence of AWL formed by continental inputs (Prestes et al., 2018).~~

~~Both baroclinic flows demonstrated an significant potential for shear instability, with vertical shear ranging from 10^{-5} to 10^{-3} s^{-2} off the Amazon shelf. The shear associated with the NBC was particularly pronounced around the pycnocline (between 40 and 200 m depth) at sites Aa, Ab, and G (e.g., at S6, S7, S10, S11, S14, and S24). At site E, the shear instability was stronger (>~~

~~2.5 x 10^{-4} s^{-2}) at the base of the pycnocline (e.g., at S20), potentially associated with NBC retroflection near [5-6°N, 50°W] during the fall season (Didden and Schott, 1993). The higher BC shear observed at S21, where flow direction reversals occurred, could be associated with the presence of a subsurface cyclonic eddy (Dossa et al., in preparation).~~

ITs shear

Second, the semi-diurnal (M2) baroclinic currents were extracted from the total baroclinic current, revealing pronounced IT signatures and associated tidal shear on the slope compared to the open ocean. Tidal amplitudes, eigenmodes, and shear were stronger along the HTE paths compared to the LTE path. At slope stations on the HTE paths, tidal amplitudes were high (35-45 cm s-1) with dominant modes 6-7, whereas at slope stations on the LTE path, amplitudes were reduced (20 cm s-1) with mode 4. In the open ocean, tidal amplitudes and modes were generally lower (15-25 cm s-1; modes 3-5), except at Aisw and $A^{a}_{o_2}$, where amplitudes remained elevated (40 cm s-1), particularly near the pycnocline. Vertical shear associated with baroclinic tidal currents was also stronger along the HTE paths, with values of 5.5-7.7 × 10-4 s-2 at slope stations, compared to 1.2 × 10-4 s-2 along the LTE path. In the open ocean, shear values were generally weaker (2.0–3.5 × 10-4 s-2), except at Aisw and $A^{a}_{o_2}$, where they remained high (5.0–7.6 × 10-4 s-2), particularly around the pycnocline. Strong IT signals–observed in amplitudes, modes, and associated shear–near slopes along the HTE paths align with measurements at other generation sites (e.g., Hawaiian Ridge, Zhao et al., 2016; Ombai Strait and Halmahera Sea, Bouruet-Aubertot et al., 2018). In contrast, slightly weaker IT signals near slopes along the LTE path are consistent with observations from regions of low IT activity (e.g., Banda Sea, Bouruet-Aubertot et al., 2018). Offshore, IT signals are typically weak, consistent with areas distant from generation sites (e.g., Halmahera Sea, Bouruet-Aubertot et al., 2018), except at stations Aisw and $A^{a}_{o_2}$, where there are IT signal hotspots.

These results suggest that shear instabilities–driven by the mean flow and IT–may lead to mixing off the Amazon shelf, raising the question of whether MBC or IT dominates the mixing process.

~~Second, the baroclinic tidal current was extracted from the total baroclinic current, revealing significant semi-diurnal (M2) component signals around the pycnocline. These signals, characterized by higher tidal modes (3-5), were more pronounced at generation and propagation sites Aa and Ab (e.g., at S6, S10, and S14) compared to other sites. The tidal shear within the pycnocline layer (80-120 m) is consistent with the observed IT signal patterns and large vertical displacements. It was stronger, reaching up to 10^{-3} s^{-2}, near the generation sites Aa and Ab (at S6 and S10) and in the open ocean at S14. Further from the generation sites (e.g., at S7, S11, and S20), the IT shear was smaller but still notable (reaching up to 10^{-4} s^{-2}). This highlights the significant role of ITs in driving mixing processes, particularly within the pycnocline, where strong vertical shears were observed near the shelf-break compared to regions far away. Outside the IT fields, such as at S24, the persistent high vertical shear near the bottom topography could be attributed to the active bottom boundary layer (Inall et al., 2021).~~

IT/MBC ratio

Through direct quantification, we determined the relative contributions of MBC and IT to mixing. The results showed that both IT and MBC shear contribute to mixing, with their relative dominance varying across the HTE paths and LTE path. Near generation sites at slope stations (A_s^a, $A_{s_2}^b$, and Es), IT shear dominated the IT/MBC shear ratio, contributing approximately ~60% to mixing. At open-ocean stations farther from generation sites (e.g., at $A_{o_2}^a$, $A_{o_3}^a$, and Eo), the contributions were nearly balanced, with each contributing around 50%. Exceptions in the open ocean were observed at station Aisw, where IT shear became dominant again (contributing ~60%), and at station A_o^b, where IT shear contribution decreased to ~30%. These results show that strong mixing near IT generation sites is primarily driven by IT shear instability, coherent with other sites (Klymak et al., 2006; Koch-Larrouy et al., 2015; Bouruet-Aubertot et al., 2018). Offshore, weaker mixing along IT paths is due to both IT and mean flow shear instability. This reduced mixing could result from ITs interacting with background flows, which advect energy away, or from effective offshore radiation (Whalen et al., 2012). At A_o^b, away from generation sites, the lower IT shear contribution to mixing was attributed to the strong influence of the MBC, dominated by the NBC.

The most relevant finding of this study was an increased mixing near the pycnocline layer, which surfaces at Aisw in the open ocean. This supports the results of Assene et al. (2024) and Macedo et al. (2025).

~~Both IT and BC shear contribute to mixing, with their relative dominance varying across sites. Near the generation sites on the shelf break, IT shear dominated the IT/BC shear ratio, such as at S6 (61.4/38.6% %), S10 (65.8/34.2% %), and S21 (58.5/41.5% %). Along the IT paths, the contributions were nearly equal (~50/50% %) at locations farther from the generation sites (e.g., at S20, S7, S11, and S13), except at S14 in the open ocean, where IT shear remained dominant (58.5/41.5% %). These findings align with the presence of ITs at generation sites Aa, Ab, and E (Tchilibou et al., 2022; Assene et al., 2024) and the stronger energy associated with NBC cores, particularly at S7 and S11.~~

~~These results are consistent with previous studies that identified strong tidal shear near IT generation sites, such as the Halmahera Sea (Bouruet-Aubertot et al., 2018), the Changjiang Estuary (Yang et al., 2020), the northwest European continental shelf seas (Rippeth et al., 2005), and the southern Yellow Sea (Xu et al., 2020).~~

~~The most relevant finding of this study was the relative increase in mixing within the pycnocline layer, observed at S14 in the open ocean, far from the IT generation sites.~~

Unexpected strong open-ocean mixing at Aisw~~Discussion on the strong mixing at S14~~

Along the HTE paths at station Aisw, elevated remote dissipation rates (~10-7 W kg-1) were detected ~230 km from the shelf break. This region has been modeled as a surface-reaching IT dissipation hotspot (Tchilibou et al., 2022; Assene et al., 2024), driving sea surface temperature cooling (Assene et al., 2024). Observations also link this area to chlorophyll blooms (de

Macedo et al., 2025; M'Hamdi et al., 2025) and the generation of large-amplitude (>100 m) nonlinear IT-induced (Brandt et al., 2002; de Macedo et al., 2023).

Our key findings quantify mixing hotspots in the water column at Aisw, including intensified mixing at the mixed-layer base, providing in situ validation for prior model hypotheses (Tchilibou et al., 2022; Assene et al., 2024). We further propose that IT disintegration into nonlinear, more dissipative baroclinic flux may occur here. At Aisw, IT rays from two distinct generation sites (A^a and A^b) surface alongside documented ISWs, coinciding with the vanishing point of NBC. This interaction zone may foster constructive interference of IT rays, potentially creating higher tidal modes (New & Pingree, 1992; Silva et al., 2015; Barbot et al., 2022; Solano et al., 2023). Such modes could enhance nonlinear ISW generation (e.g., Jackson et al., 2012) and explain the observed elevated dissipation rates (Xie et al., 2013).

~~Along the HTE paths, elevated remote dissipation rates ([10^{-7}] W kg^{-1}) were identified approximately 230 km from the shelf break at station Aisw. This region has been pointed out previously by models for exhibiting intense IT dissipation up to the surface (Tchilibou et al., 2022; Assene et al., 2024), that induces SST cooling (Assene et al. 2024). Furthermore, in observations studies, this region has been recently shown to create chlorophyll blooms (de Macedo et al. 2025, M'Hamdi et al. 2025). Finally, the region is the starting point of non linear IT-induced ISWs (Fig. 1a; de Macedo et al., 2023), which often exceed 100 m in amplitude (Brandt et al., 2002, M'Hamdi et al. 2025). Our results provide a key finding, by quantifying the hot spots of mixing all along the water column at station Aisw, including intensified mixing at the base of mixed layer, that could provide an in-situ validation to the model hypothesis (Tchilibou et al., 2022; Assene et al., 2024). in additio, in our study, we provide a complement interpretation of possible disintegration into nonlinear and more disspative baroclinic flux. Indeed, IT rays surface from two distinct generation sites (Aa and Ab) coincide with the appearance of ISWs and mark the location where the NBC vanishes. This region of wave-wave interactions may lead to the constructive interference of IT rays, potentially facilitating the emergence of higher tidal modes (New & Pingree, 1992; Silva et al., 2015; Barbot et al., 2022; Solano et al., 2023). These higher modes could enhance the generation of nonlinear ISWs (e.g., Jackson et al., 2012) and contribute to the elevated dissipation rates observed at this station (Xie et al., 2013).~~

~~Along the IT paths, elevated remote dissipation rates (within [10^{-7}, 10^{-6}] W kg^{-1}) were identified ~ 230 km from the shelf-break at S14.~~

~~This region is well known for intense IT dissipation, as shown by a realistic model (Tchilibou et al., 2022; Assene et al., 2024), and for the highest occurrences of IT-induced ISWs generated by ITs (Fig. 1a; de Macedo et al., 2023), with a largewith large_-amplitude ISWs exceeding 100 m clearly visible in satellite records (Brandt et al., 2002). These ISWs have a large amplitude exceeding 100 m clearly visible in satellite records (Brandt et al., 2002).~~

~~At station S14, where relative mixing increases, IT rays surfacing from two distinct IT generation sites coincide with the appearance of ISWs and mark the location where the NBC vanishes.~~

~~This region of wave-wave interactions can lead to the constructive interference of IT rays, potentially facilitating the emergence of higher tidal modes (New & Pingree, 1992; Silva et al., 2015; Barbot et al., 2022; Solano et al., 2023). These higher modes, in turn, could enhance the generation of nonlinear ISWs (e.g., Jackson et al., 2012) and contribute to the elevated dissipation rates (Xie et al., 2013), as observed at this station.~~

Appendix A

The AMAZOMIX measurement sites and stations were systematically named and organized by location. Each site received a unique identifier based on its position along the HTE and LTE paths. Stations were categorized by site and region: superscripts 'a' and 'b' denoted stations at sites A^a and A^b, respectively, while subscripts indicated location—'sh' for shelf, 's' for slope, 'o' for offshore/open ocean, and 'isw' for ISW regions (Table A1). This structured naming system ensured clear identification and logical grouping of stations for consistent data analysis.

<table>
<tr><th rowspan="2">Paths / Transects</th><th rowspan="2">Sites</th><th colspan="8">Stations</th></tr>
<tr><th colspan="2">Shelf</th><th colspan="2">Slope</th><th colspan="3">Offshore/Open ocean</th><th>ISWs</th></tr>
<tr><td rowspan="2">High Tidal Energy (HTE) paths</td><td>A^a</td><td>$A^a_{sh_1}$</td><td>$A^a_{sh_2}$</td><td colspan="2">A^a_s</td><td>$A^a_{o_1}$</td><td>$A^a_{o_2}$</td><td>$A^a_{o_3}$</td><td rowspan="2">Aisw</td></tr>
<tr><td>A^b</td><td colspan="2">A^b_{sh}</td><td>$A^b_{s_1}$</td><td>$A^b_{s_2}$</td><td colspan="3">A^b_o</td></tr>
<tr><td>Low Tidal Energy (LTE) path</td><td>E</td><td colspan="2">Esh</td><td colspan="2">Es</td><td colspan="3">Eo</td><td>-</td></tr>
</table>

Table A1: The naming system of the AMAZOMIX cruise measurement sites and stations.

Appendix B

To relate each mixing event with either tidal or mean (time-averaged) currents along the HTE transects (A^a and A^b) and the LTE transect (E), we quantify the relative contributions of mean baroclinic vertical shear squared $S^{2\prime}$ and semi-diurnal baroclinic vertical shear squared $S^{2''}$ at transect stations (see Table A2).

Table A2: miXing Layer Depth (XLD), Mixed Layer Depth (MLD), Contribution (mean and standard deviation) of the Semi-diurnal (CSBS), and Mean Baroclinic (CMBS) Shear to total baroclinic shear.

Stations	XLD (m)	MLD (m)	CSBS (mean ± SD) (%)	CMBS (mean ± SD) (%)
A^b_{sh}	27	25.0	-	-
$A^b_{s_1}$	20	5.0	-	-
$A^b_{s_2}$	57	17.8	66.2 ± 0.3	33.8 ± 0.3
A^b_{o}	46	22.5	36.7 ± 3.7	63.3 ± 3.7
$A^a_{sh_2}$	23	44.5	-	-
$A^a_{sh_1}$	29	21.0	-	-
A^a_{s}	26	32.5	60.0 ± 4.0	40.0 ± 4.0
$A^a_{o_1}$	104	15.5	47.6 ± 4.9	52.4 ± 4.9
$A^a_{o_2}$	75	11.3	56.6 ± 3.3	43.4 ± 3.3
$A^a_{o_3}$	82	12.3	59.1 ± 3.4	40.9 ± 3.4
Aisw	97	12.3	63.6 ± 4.8	36.4 ± 4.8
Esh	45	1.0	-	-
Eo	73	1.8	56.6 ± 3.9	43.4 ± 3.9
Es	53	1.0	60.2 ± 2.8	39.8 ± 2.8

SD = Standard Deviation.

Appendix C

Following subsection 2.2.2, we examined the cross-shelf component of baroclinic tidal currents to investigate IT amplitude (current strength) and shear instability around the pycnocline (70–180 m depth; see Table A3). Additionally, the along-shelf component of mean baroclinic currents (MBC) was analyzed to evaluate the strength of the mean flow and its associated shear instability in the upper 200 m (see Table A3).

Table A3: Strength of baroclinic tidal and mean baroclinic *currents*.

Stations	IT amplitudes (cm s-1; maximum)	Estimated number of IT eigenmodes	IT vertical shears (s-2 x 10-4; **maximum**)	**MBC velocities (cm s-1; maximum)**	**MBC vertical shear (s-2 x 10^{-4}; maximum)**
$A^{b}_{s_2}$	35	6-7	5.5	90	1.2
A^{b}_{o}	15	4-5	2.5	98	1.7
A^{a}_{s}	45	6-7	7.7	30	0.7
$A^{a}_{o_1}$	25	4	2.0	90	1.2
$A^{a}_{o_2}$	40	3	7.6	67	1.2
$A^{a}_{o_3}$	25	3	3.3	69	1.3
Aisw	40	4.5	5.0	71	1.1
Eo	15	4	3.5	43	2.7
Es	20	4	1.2	28	0.8

Formatted: Normal, Indent: Left: 0 cm, Line spacing: 1,5 lines

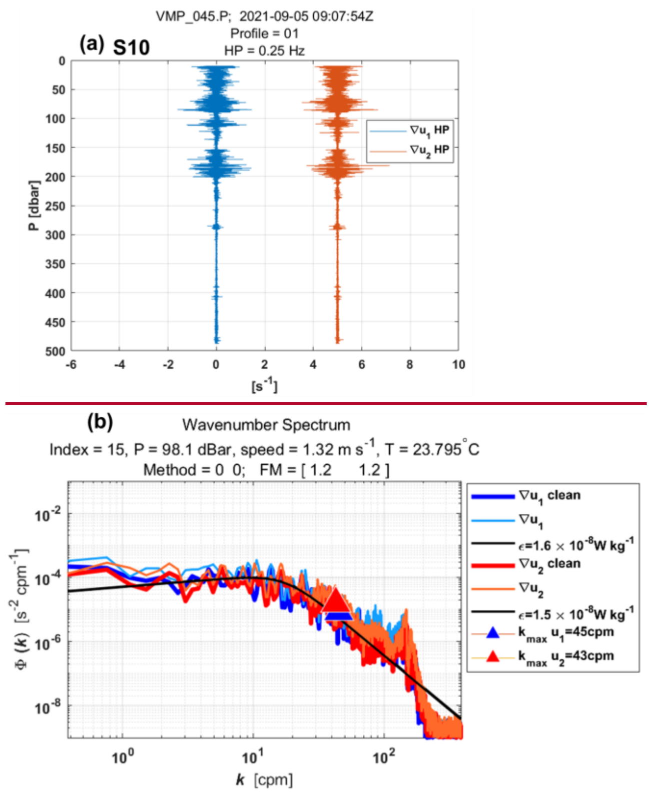

~~*Figure A1: Example of wavenumber spectra from a dissipation structure segment recorded at station S10 at a pressure of 98.1 dBar. (a) Cleaned and high-pass filtered signals from shear probe 1 (blue) and shear probe 2 (red, offset by 5 s^{-1}). (b) Wavenumber spectra for shear probes 1 and 2. Thick lines (blue for probe 1, red for probe 2) show shear spectra with coherent noise correction, while thin lines (sky blue for probe 1, orange for probe 2) show spectra without correction. Triangles mark the maximum wavenumber used for dissipation rate estimation. Black lines represent Nasmyth reference spectra for estimated dissipation rates of 1.6 x 10^{-8} W kg^{-1} (probe 1) and 1.5 x 10^{-8} W kg^{-1} (probe 2). Dissipation rate estimates for both shear probes at a pressure of 98.1 dBar yielded a figure of merit of 1.2.*~~

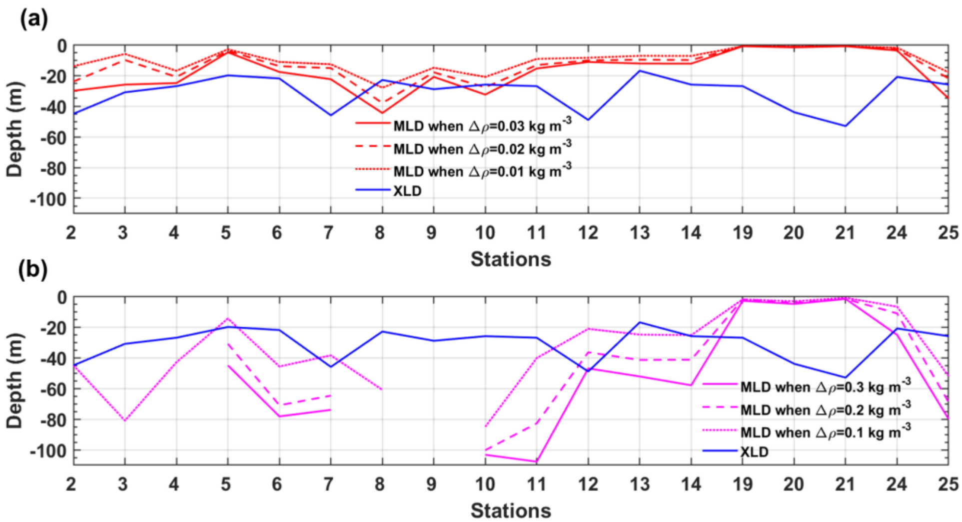

~~*Figure A2: Comparison of Mixing Layer Depths (XLD, blue line) with Mixed Layer Depths (MLD) defined using (a) larger and (b) smaller density thresholds (Δ□). In panel (a), dotted, dashed, and solid red lines represent MLDs defined by Δ□ =* 0.01, 0.02, 0.03 kg m^{-3}, *respectively. In panel (b), dotted, dashed, and solid magenta lines represent MLDs defined by Δ□ =* 0.1, 0.2, 0.3 kg m^{-3}, *respectively.*~~

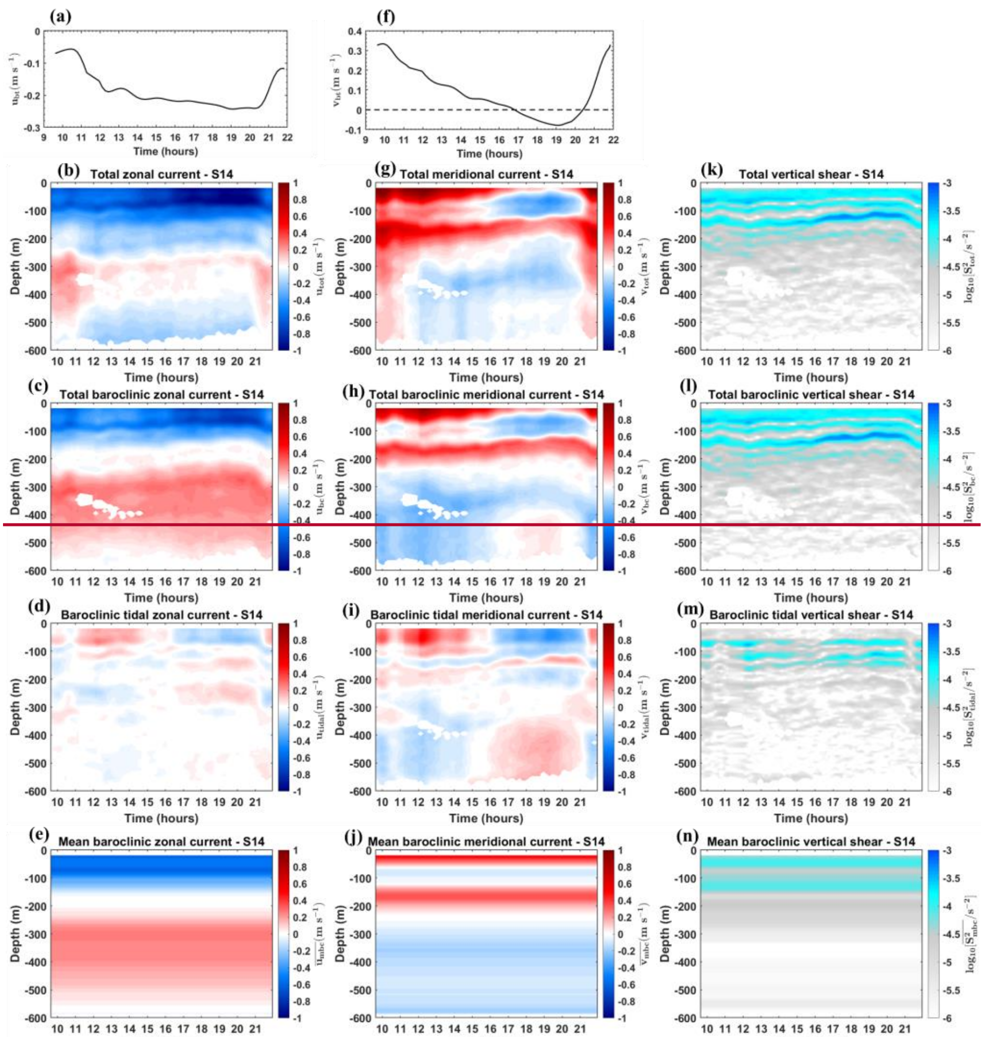
(a)
$u_{bt}(m\ s^{-1})$
Time (hours)
(f)
$v_{bt}(m\ s^{-1})$
Time (hours)
(b) Total zonal current - S14
$u_{tot}(m\ s^{-1})$
(g) Total meridional current - S14
$v_{tot}(m\ s^{-1})$
(k) Total vertical shear - S14
$\log_{10}[S^2_{tot}/s^{-2}]$
(c) Total baroclinic zonal current - S14
$u_{bc}(m\ s^{-1})$
(h) Total baroclinic meridional current - S14
$v_{bc}(m\ s^{-1})$
(l) Total baroclinic vertical shear - S14
$\log_{10}[S^2_{bc}/s^{-2}]$
(d) Baroclinic tidal zonal current - S14
$u_{tidal}(m\ s^{-1})$
(i) Baroclinic tidal meridional current - S14
$v_{tidal}(m\ s^{-1})$
(m) Baroclinic tidal vertical shear - S14
$\log_{10}[S^2_{tidal}/s^{-2}]$
(e) Mean baroclinic zonal current - S14
$\overline{u_{mbc}}(m\ s^{-1})$
(j) Mean baroclinic meridional current - S14
$\overline{v_{mbc}}(m\ s^{-1})$
(n) Mean baroclinic vertical shear - S14
$\log_{10}[\overline{S^2_{mbc}}/s^{-2}]$
Depth (m)
Time (hours)

~~*Figure A3: For Station S14. zonal currents for (b) total, (a) barotropic, (c) total baroclinic, (d) semi-diurnal baroclinic tidal, and (e) mean baroclinic. Meridional currents for (g) total, (f) barotropic, (h) total baroclinic, (i) semi-diurnal baroclinic tidal, and (j) mean baroclinic. Vertical shear for (k) total, (l) total baroclinic, (m) semi-diurnal baroclinic tidal, and (n) mean baroclinic.*~~

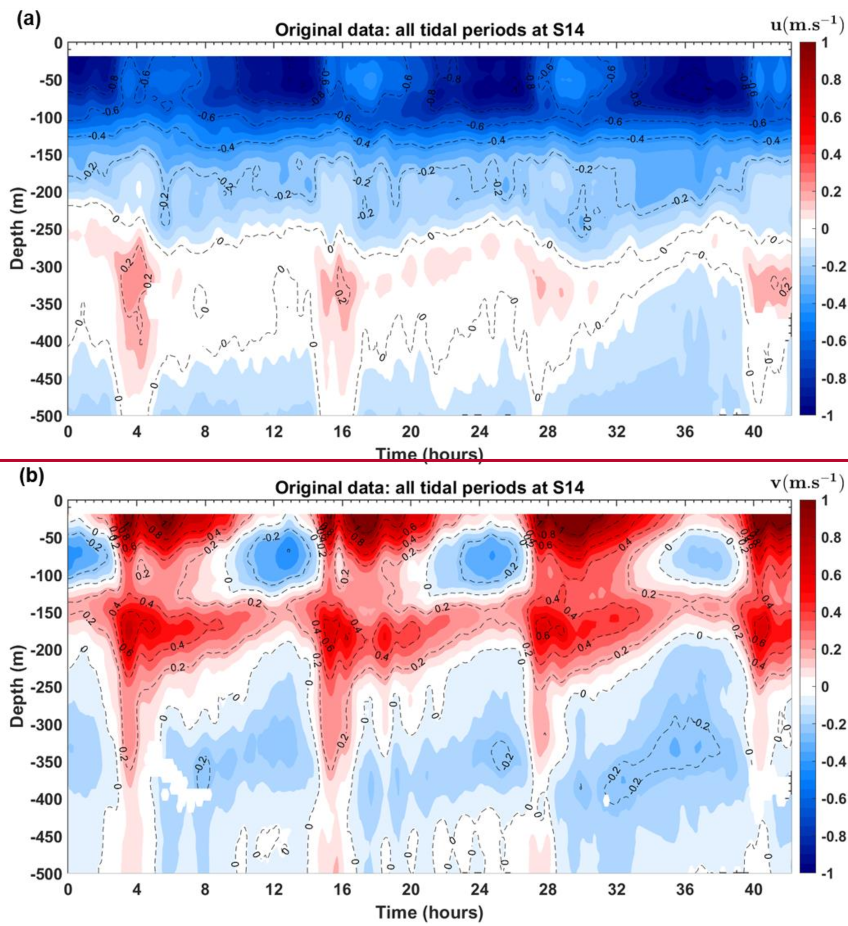

~~*Figure A4: Time series of (a) total zonal and (b) meridional current from SADCP data at station S14. Time is scaled to start at t=0.*~~

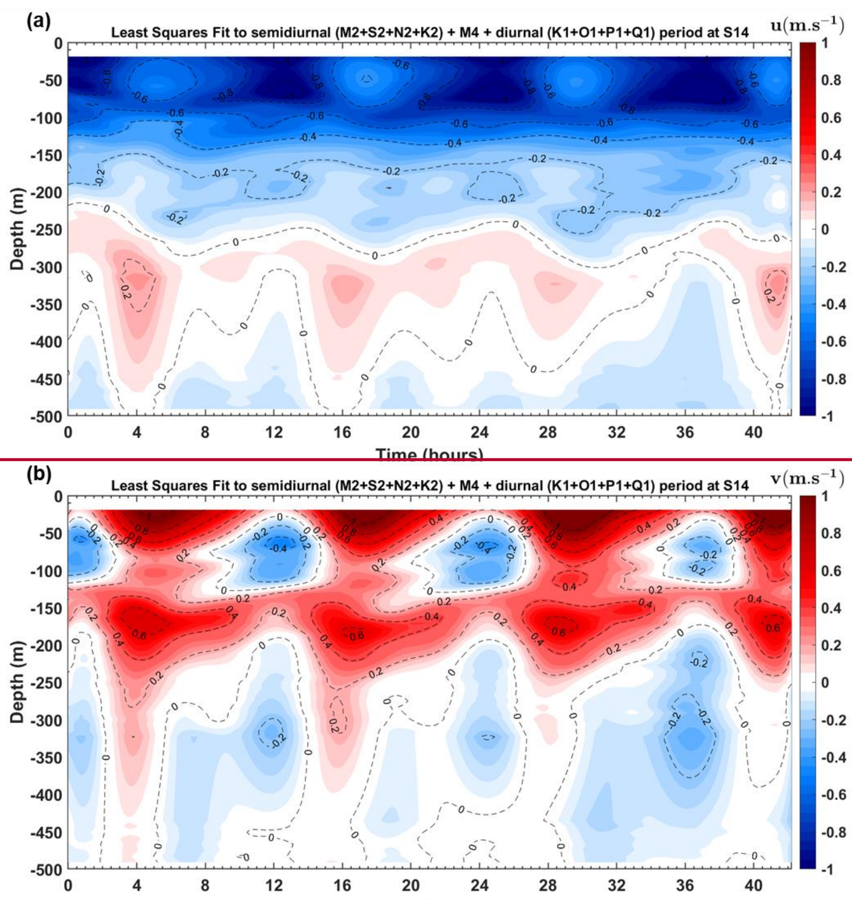

~~*Figure A5: Least squares fit of sines and cosines to semidiurnal (M2+S2+N2+K2) + M4 + diurnal (K1+O1+P1+Q1) periods for total (a) zonal and (b) meridional current at station S14. Time is scaled to start at t=0.*~~

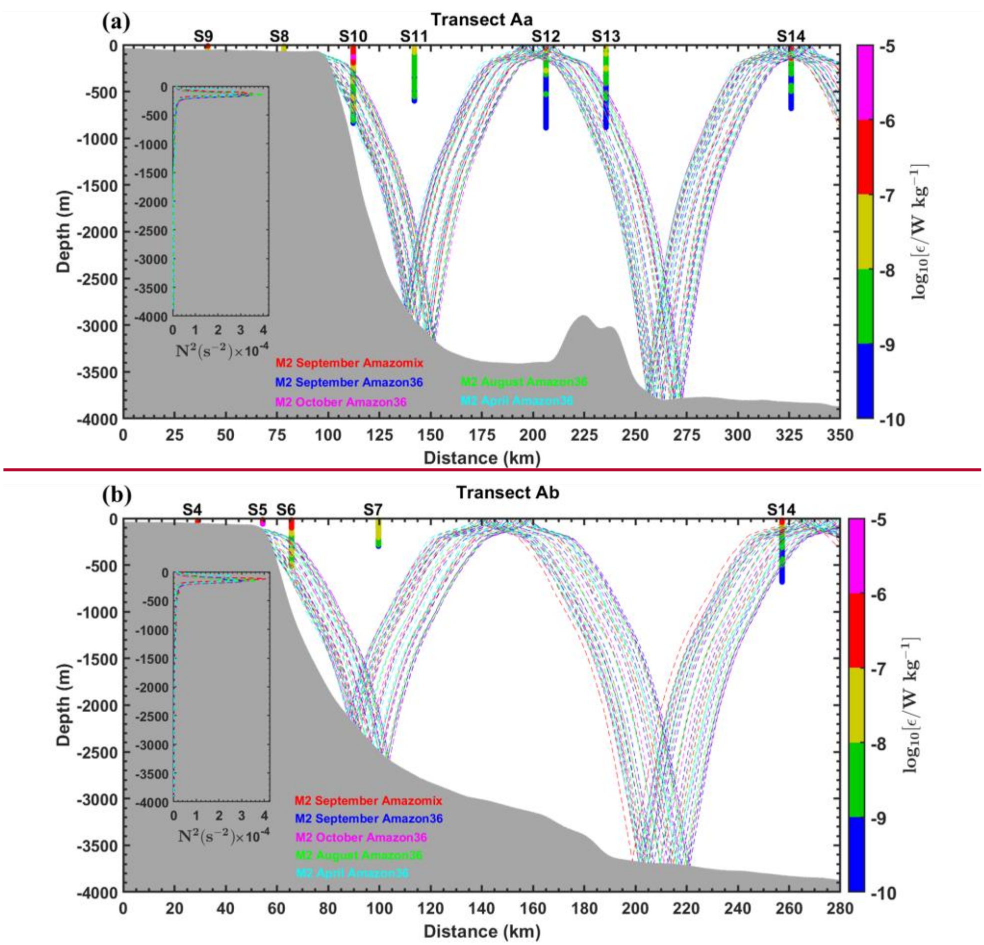

~~*Figure A6: Sensitivity tests of M2 IT ray-tracing along the transects (a) Aa and (b) Ab, conducted by varying the location of the critical topography slope. The tests use mean buoyancy frequency squared (N^2, in s^{-2}) obtained from CTD-O_2 data (September 2021) and NEMO-Amazon36 model data (2012-2016). Dashed colored lines represent IT beams calculated for*~~

~~*different seasons (April, August, October, and September) and for varying locations of the critical topography slope. Grey areas indicate local topography. Panels (a) and (b) also include dissipation rate profiles (ε, in W kg^{-1}, shown as vertical colored bars on a logarithmic scale) from the VMP measurements. Subpanels within each panel illustrate the N^2 profiles derived from AMAZOMIX and the NEMO-Amazon36 model, which were used in the ray-tracing calculations. For comparison, sensitivity tests using different N^2 measurements from individual stations along the corresponding transect (e.g., at S10 and S14) revealed similar ray paths (not shown), consistent with the set of rays obtained using the mean N^2.*~~

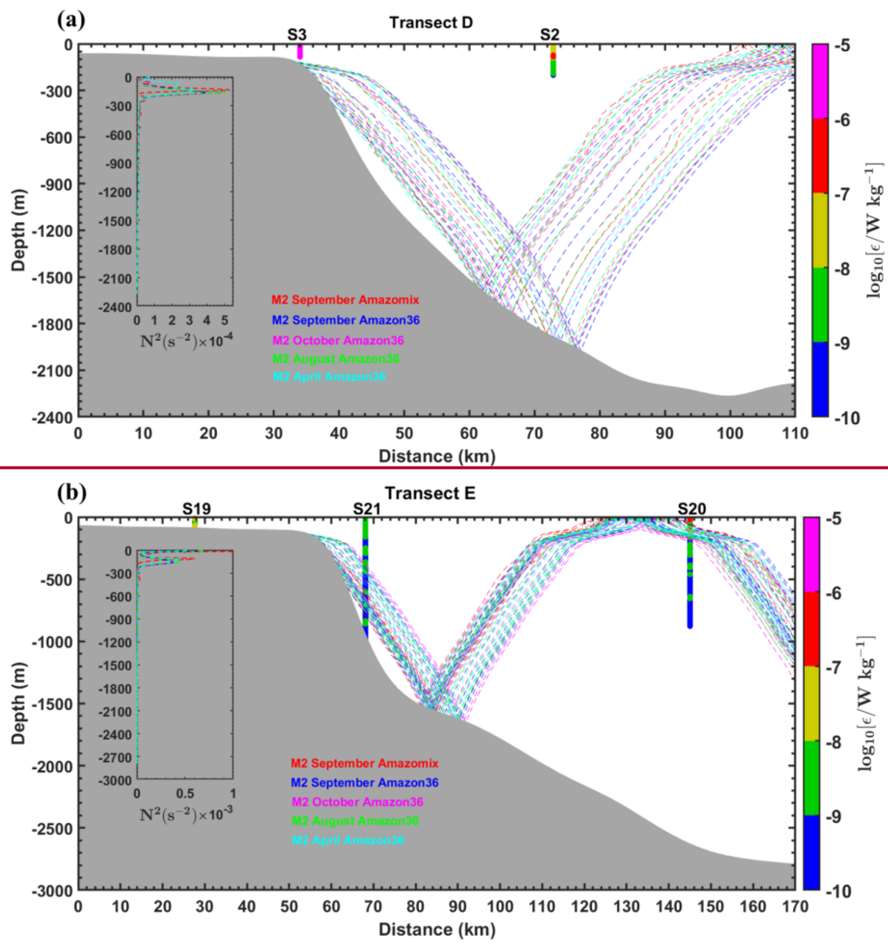

~~*Figure A7: Panels are similar to Fig. A19 but for transects D and E.*~~

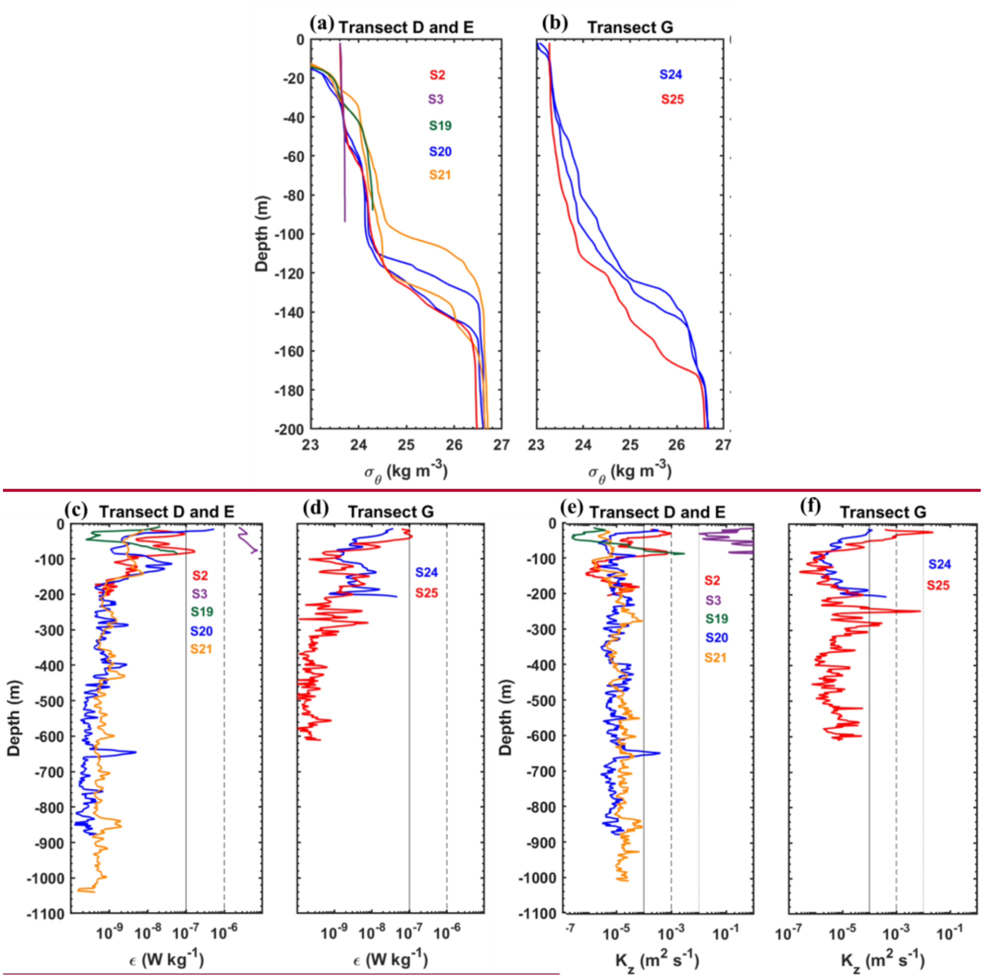
(a) Transect D and E
(b) Transect G
(c) Transect D and E
(d) Transect G
(e) Transect D and E
(f) Transect G
S2
S3
S19
S20
S21
S24
S25
Depth (m)
σ_θ (kg m^{-3})
ϵ (W kg^{-1})
K_z (m^2 s^{-1})

~~*Figure A8: (a)-(b) Density profiles (σ_θ, kg m^{-3}) obtained from CTD-O_2 measurements during the AMAZOMIX 2021 cruise for stations (S2, S3, S19, S20, S21, S24, and S25) along transects D and E, and G, respectively. For long stations (S20, S21, and S25), two density profiles are shown to highlight step-like structures and isopycnal vertical displacements along the transects. The density values for station S3 range between 23.6 and 23.8 kg m^{-3}. (c)-(d) Vertical dissipation profiles (ϵ, in W kg^{-1}, on a logarithmic scale) from VMP and (e)-(f) vertical diffusivity profiles (K_z, in m^2 s^{-1}, on a logarithmic scale) for stations along transects D and E, and G, respectively. Distinct colors are used to represent each station within each transect. Dashed and solid black lines in panels (c) to (f) are included for comparison purposes.*~~

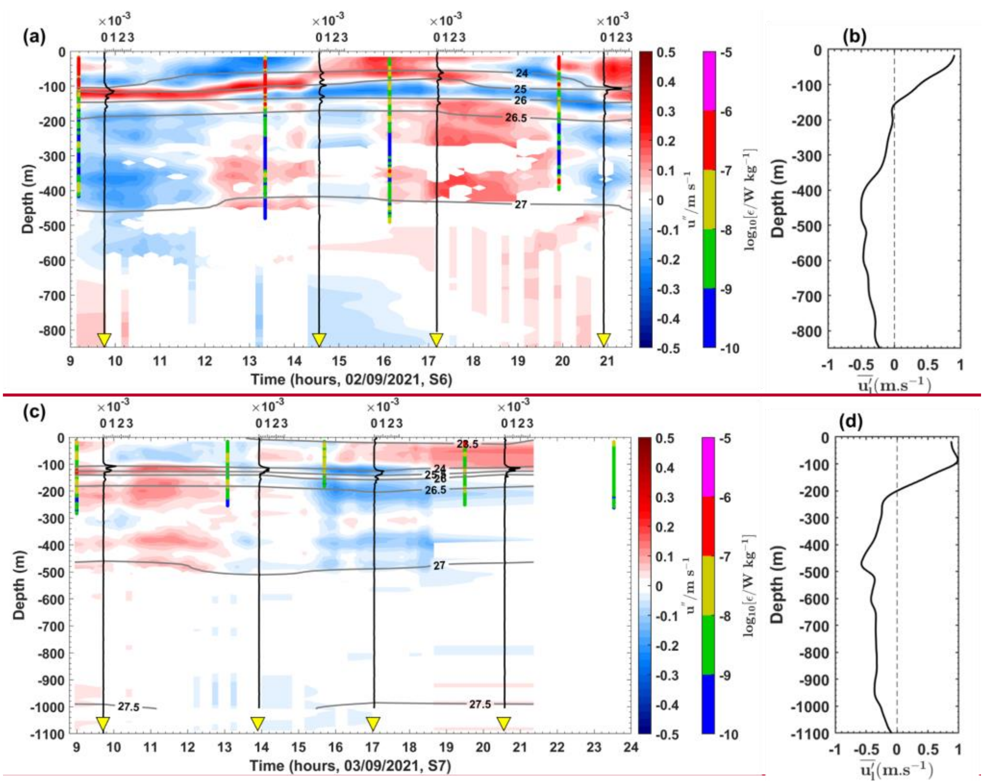

~~*Figure A9: Semi-diurnal baroclinic zonal currents (u'', in m s^{-1}) from the ADCP for stations (a) S6 and (c) S7. Panels (a) and (c) also display the buoyancy frequency squared (N^2, in s^{-2}) represented by vertical black lines, potential density represented by grey contours, and dissipation rate profiles (ϵ, in W kg^{-1}, on a logarithmic scale) represented by vertical colored bars. Along-shore mean baroclinic currents ($\underline{u'_l}$, in m s^{-1}) from the ADCP for stations (b) S6 and (d) S7.*~~

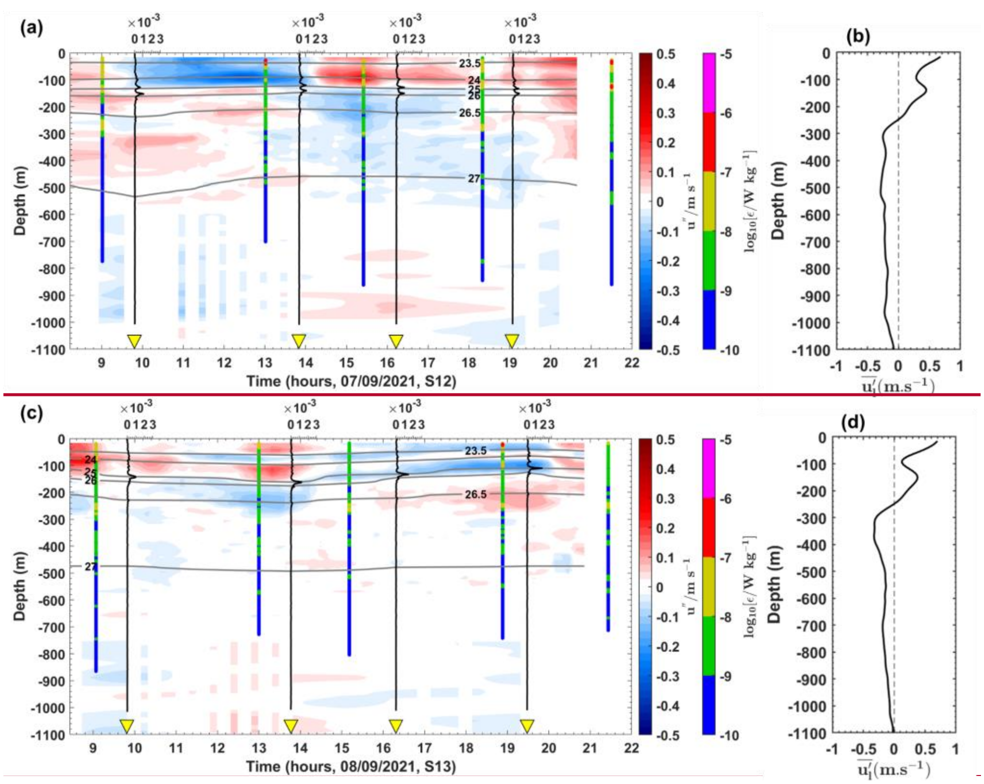

~~*Figure A10: Panels are similar to Fig. A9 but for stations (a)-(b) S12 and (c)-(d) S13.*~~

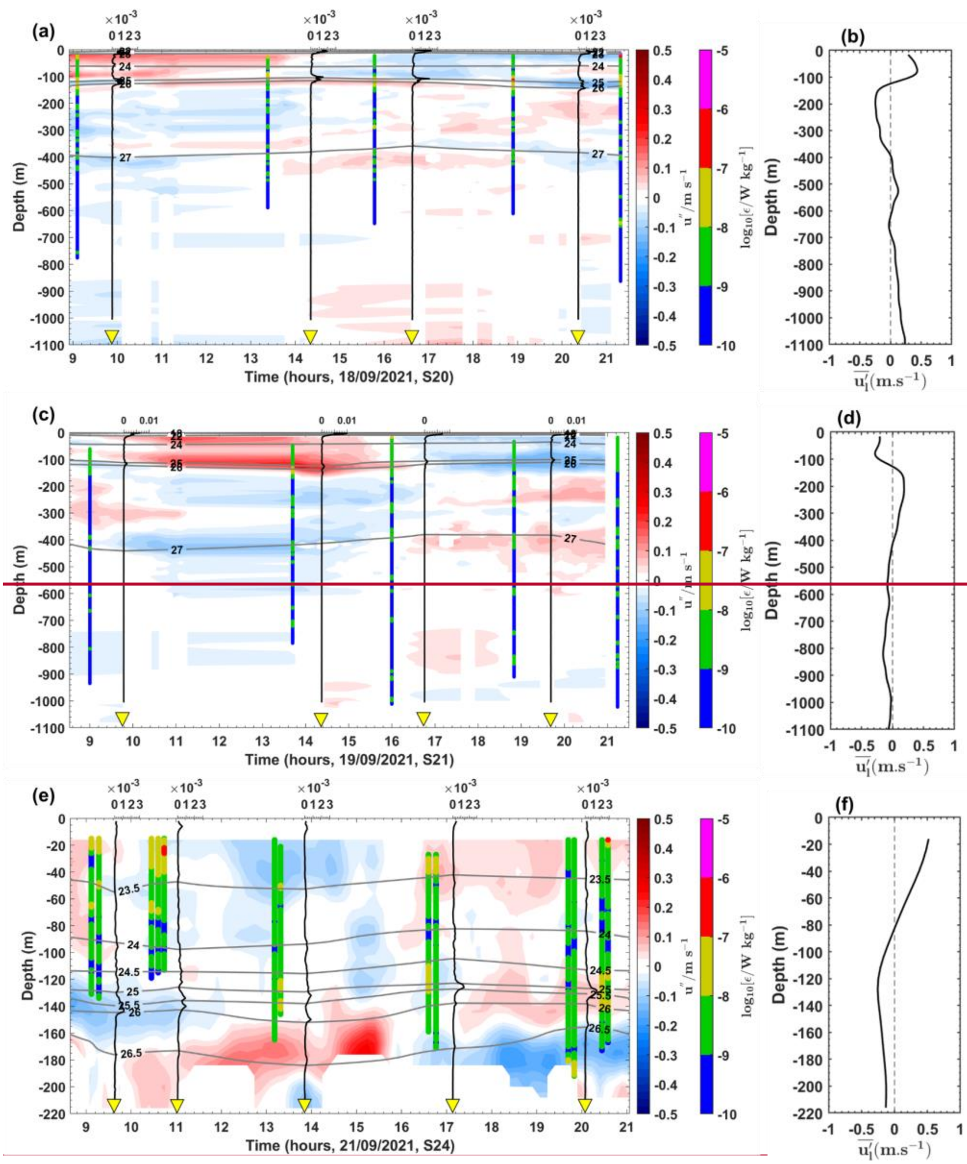
(a)
Depth (m)
Time (hours, 18/09/2021, S20)
(b)
Depth (m)
(c)
Depth (m)
Time (hours, 19/09/2021, S21)
(d)
Depth (m)
(e)
Depth (m)
Time (hours, 21/09/2021, S24)
(f)
Depth (m)

~~*Figure A11: Panels are similar to Fig. A9 but for stations (a)-(b) S20, (c)-(d) S21, and (e)-(f) S24.*~~

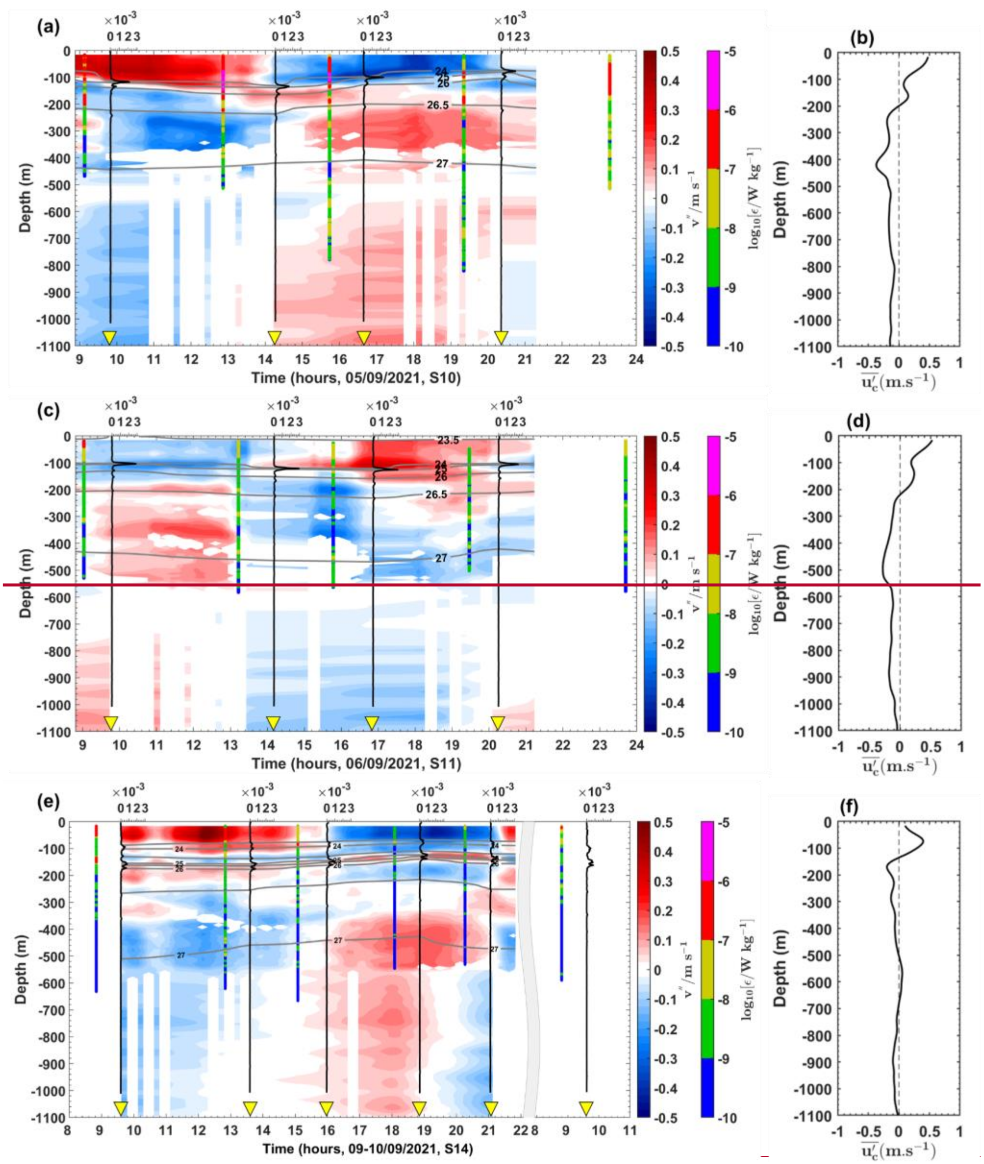
(a)
(b)
(c)
(d)
(e)
(f)
Depth (m)
Time (hours, 05/09/2021, S10)
Time (hours, 06/09/2021, S11)
Time (hours, 09-10/09/2021, S14)
$\times 10^{-3}$
0123
26.5
27
23.5
$v^{s}/\mathrm{m\,s^{-1}}$
$\log_{10}[\epsilon/\mathrm{W\,kg^{-1}}]$
$\overline{u'_c}(\mathrm{m.s^{-1}})$

~~*Figure A12: Semi-diurnal baroclinic meridional currents (u'', in m s^{-1}) from the ADCP for stations (a) S10, (c) S11, and (e) S14. Panels (a), (c), and (e) also display the buoyancy frequency squared (N^2, in s^{-2}) represented by vertical black lines, potential density represented by grey contours, and dissipation rate profiles (ϵ, in W kg^{-1}, on a logarithmic scale) represented by vertical colored bars. Cross-shore mean baroclinic currents ($\overline{u'_c}$, in m s^{-1}) from the ADCP for stations (b) S10, (d) S11, and (f) S14.*~~

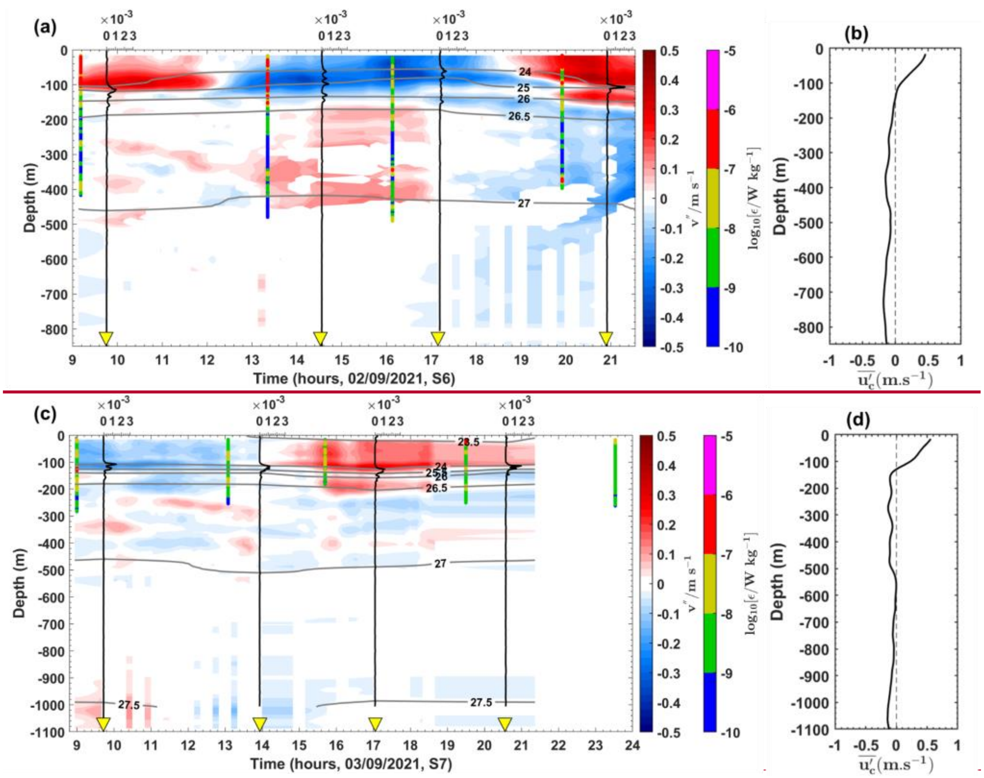

~~*Figure A13: Panels are similar to Fig. A12 but for stations (a)-(b) S6 and (c)-(d) S7.*~~

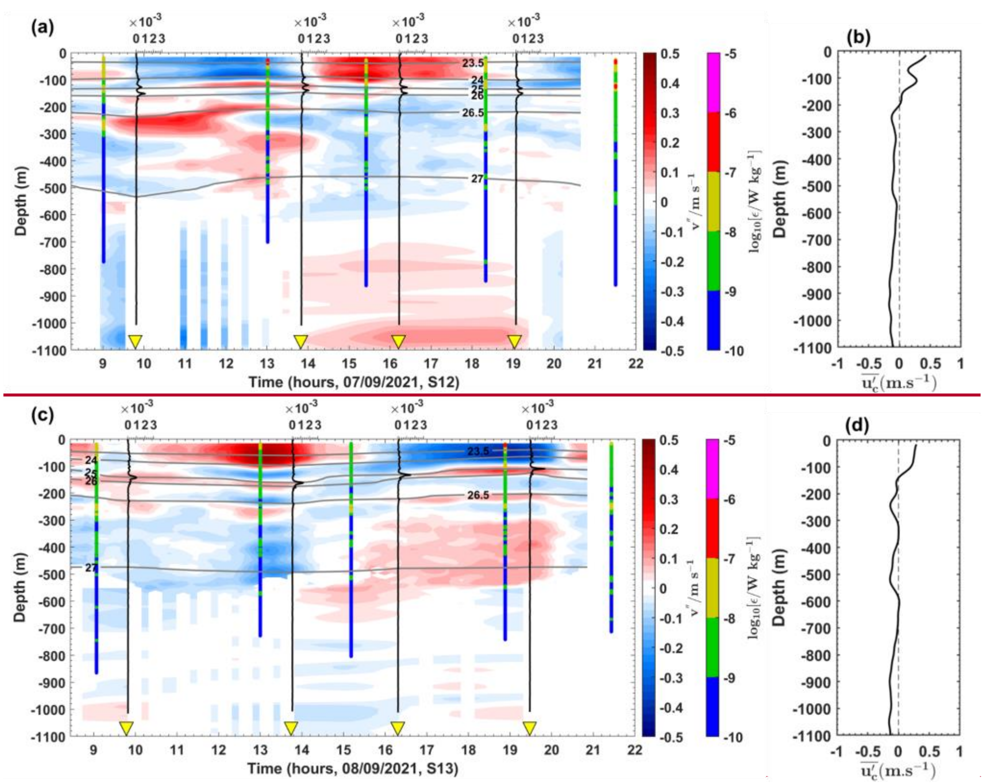

~~Figure A14: Panels are similar to Fig. A12 but for stations (a)-(b) S12 and (c)-(d) S13.~~

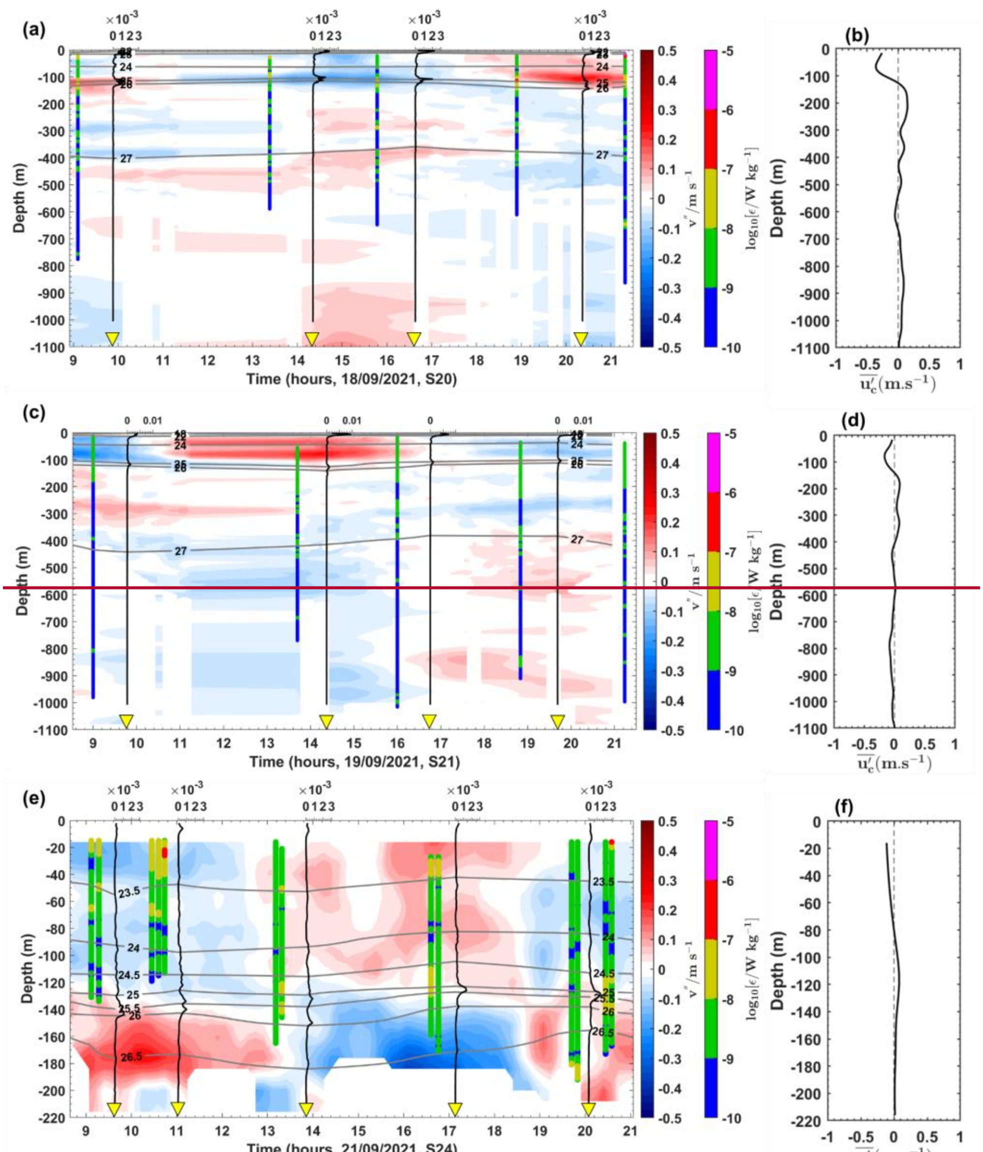
(a)
(b)
(c)
(d)
(e)
(f)
Depth (m)
Time (hours, 18/09/2021, S20)
Time (hours, 19/09/2021, S21)
Time (hours, 21/09/2021, S24)
$v''/\mathrm{m\,s^{-1}}$
$\log_{10}[\epsilon/\mathrm{W\,kg^{-1}}]$
$\overline{u'_c}(\mathrm{m.s^{-1}})$

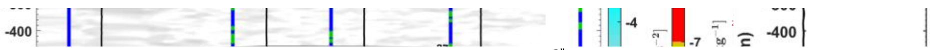

~~) (f) S24.~~

~~*Figure A16: Semi-diurnal baroclinic vertical shear squared ($S^{2''}$, in m s^{-1}, on a logarithmic scale) for stations (a) S6 and (c) S7. Panels (a) and (c) also display the buoyancy frequency squared (N^2, in s^{-2}) represented by vertical black lines, potential density represented by grey contours, and dissipation rate profiles (ϵ, in W kg^{-1}, on a logarithmic scale) represented by vertical colored bars. Mean baroclinic vertical shear squared ($\underline{S}^{2\prime}$, in m s^{-1}) for stations (b) S6 and (d) S7.*~~

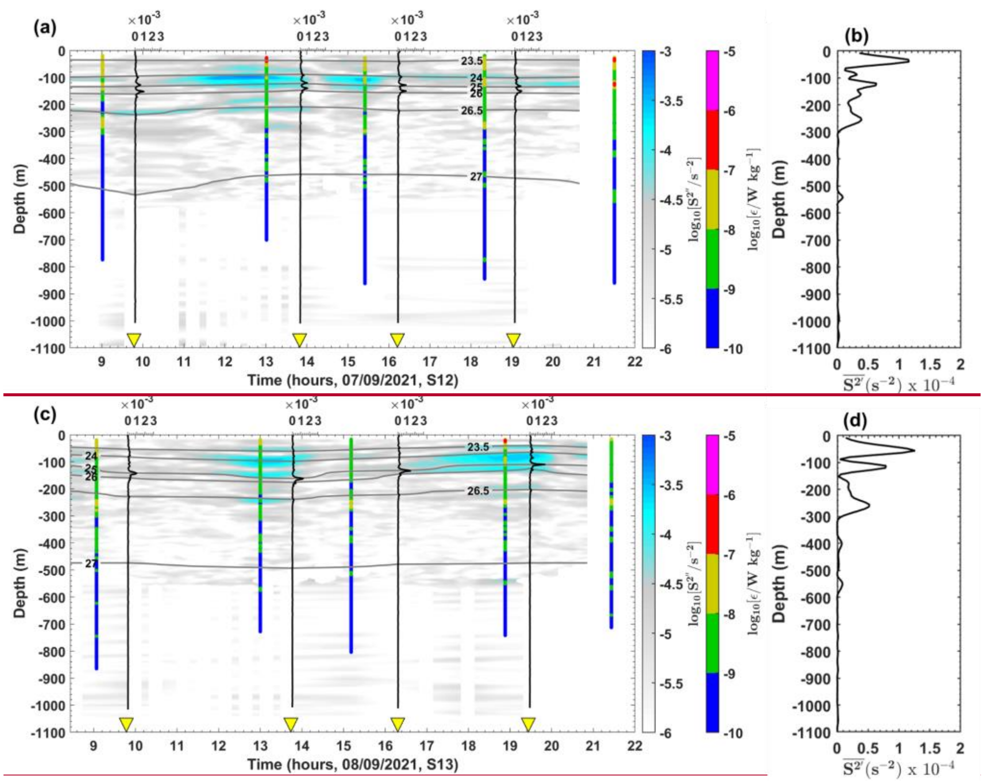

~~*Figure A17: Panels are similar to Fig. A16 but for stations (a)-(b) S12 and (c)-(d) S13.*~~

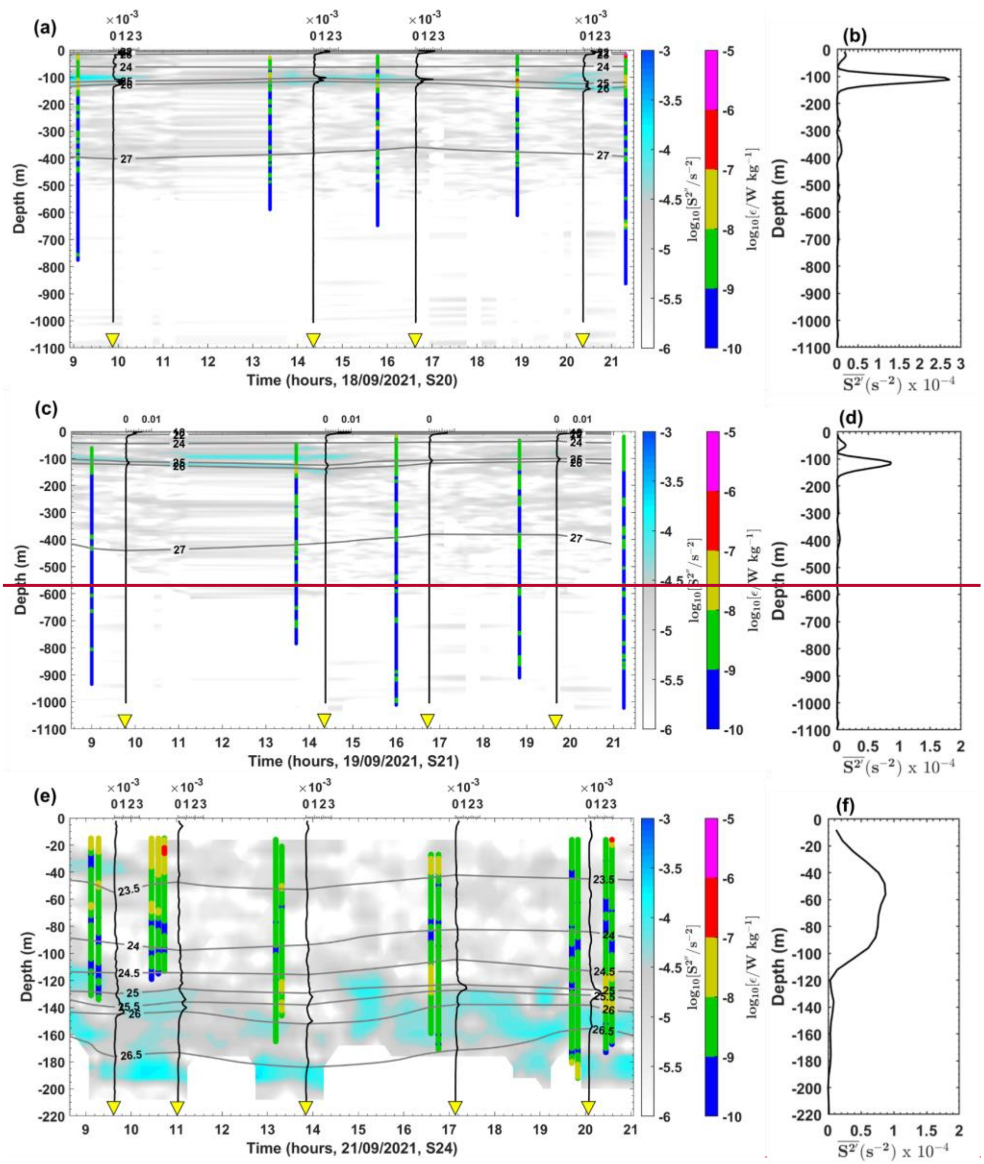
(a)
(b)
(c)
(d)
(e)
(f)
Depth (m)
Time (hours, 18/09/2021, S20)
Time (hours, 19/09/2021, S21)
Time (hours, 21/09/2021, S24)
$\log_{10}[S^{2'}/s^{-2}]$
$\log_{10}[\epsilon/W\ kg^{-1}]$
$\overline{S^{2'}}(s^{-2})$ x 10^{-4}

~~*Figure A18: Panels are similar to Fig. A16 but for stations (a)-(b) S20, (c)-(d) S21, and (e)-(f) S24.*~~

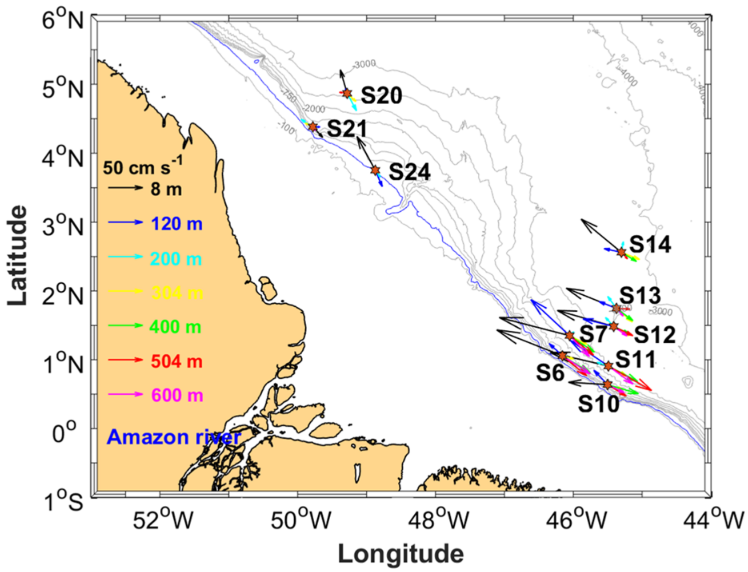

~~*Figure A19: Map of mean baroclinic currents (vectors) at stations, with colored arrows representing currents at different depths. The blue line indicates the 200 m isobath.*~~

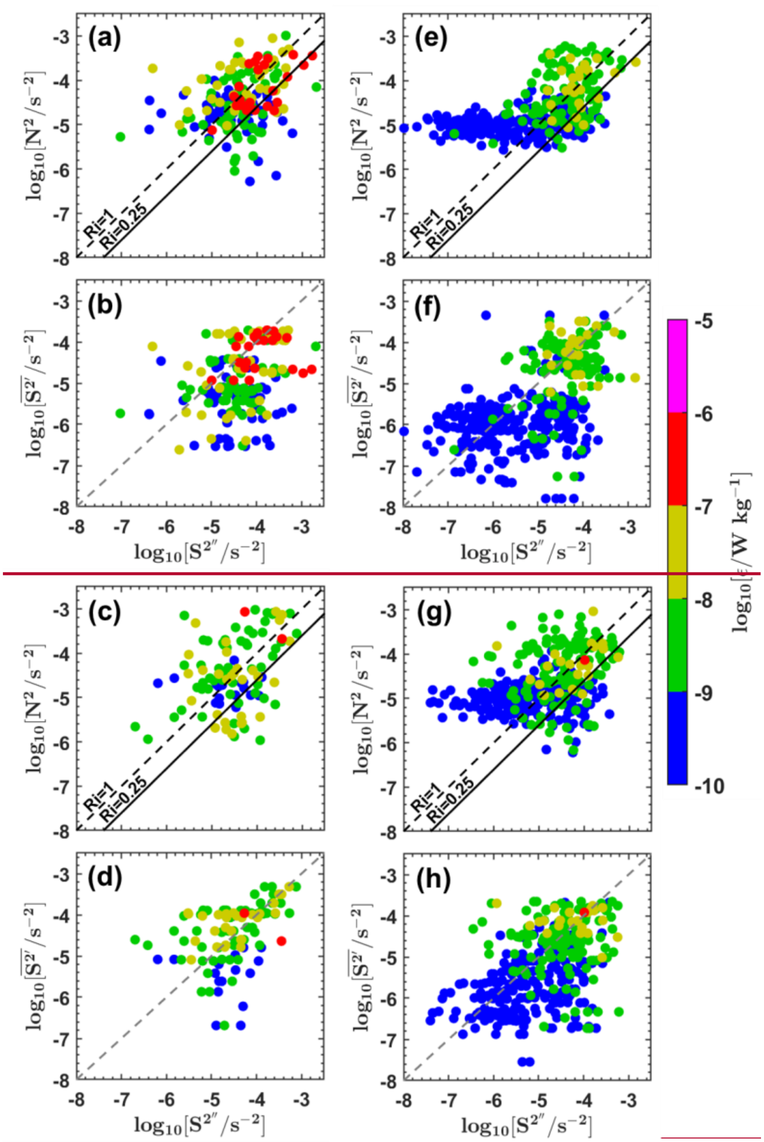
(a)
(b)
(c)
(d)
(e)
(f)
(g)
(h)
Ri=1
Ri=0.25
$\log_{10}[N^2/s^{-2}]$
$\log_{10}[\overline{S^{2\prime}}/s^{-2}]$
$\log_{10}[S^{2\prime\prime}/s^{-2}]$
$\log_{10}[\epsilon/\mathrm{W\ kg^{-1}}]$
-5
-6
-7
-8
-9
-10

~~Figure A20: Dissipation rates (ε, in W kg^{-1}, on a logarithmic scale) below the XLD as a function of the buoyancy frequency squared (N^2, in s^{-2}, on a logarithmic scale) and semi-diurnal baroclinic vertical shear squared ($S^{2''}$, in m s^{-1}, on a logarithmic scale) for stations (a) S6, (c) S7, (e) S12, and (g) S13. Dissipation rates (ε, in W kg^{-1}, on a logarithmic scale) below the XLD as a function of mean baroclinic vertical shear squared ($\underline{S}^{2'}$, in m s^{-1}, on a logarithmic scale) and semi-diurnal baroclinic vertical shear squared ($S^{2''}$, in m s^{-1}, on a logarithmic scale) for stations (b) S6, (d) S7, (f) S12, and (h) S13. N^2 was linearly interpolated into the depths of $S^{2''}$ to have same vertical scales. Panels (a), (c), (e), and (g) also display two solid black lines corresponding to Richardson number Ri = 0.25 and Ri = 1, respectively. Dashed grey lines in panels (b), (d), (f), and (h) are included for comparison purposes.~~

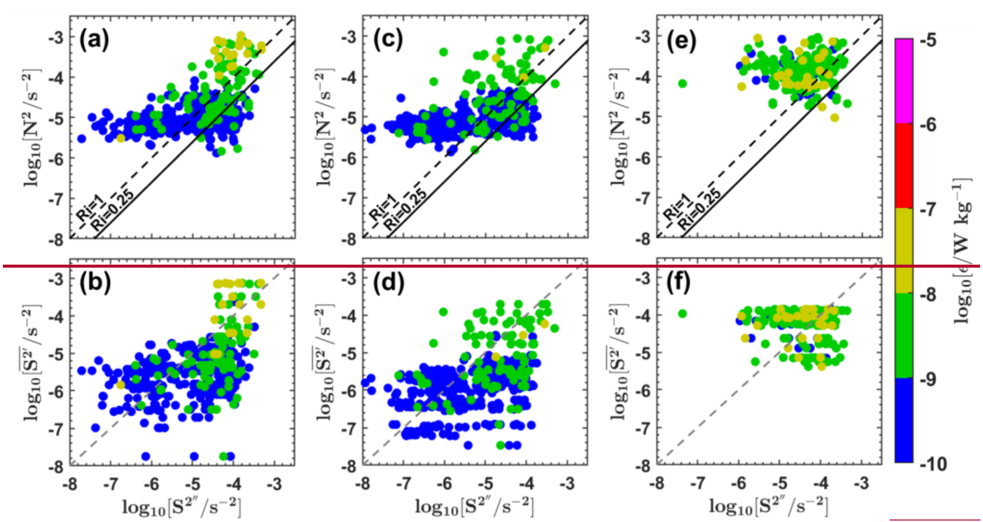

~~Figure A21: Panels are similar to Fig. A20 but for stations (a)-(b) S20, (c)-(d) S21, and (e)-(f) S24.~~

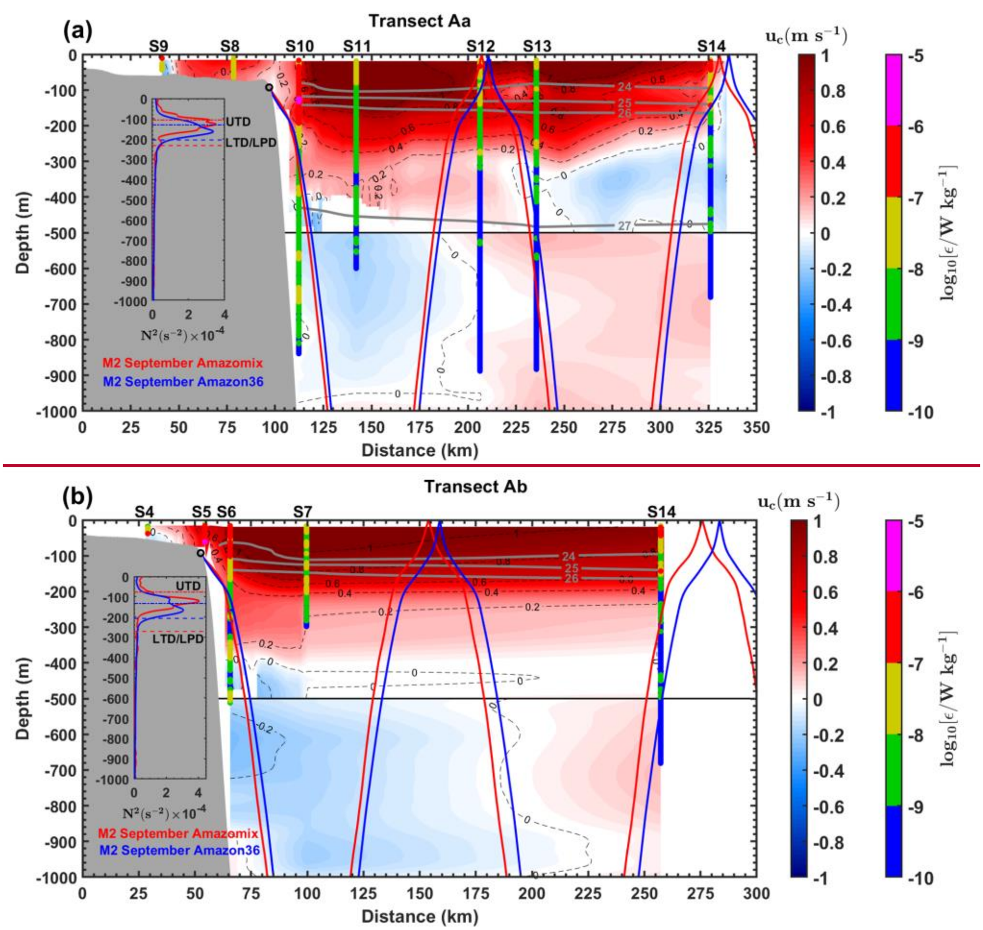

~~*Figure A22: Panels are similar to Fig. 8 but for cross-shore mean total currents (u_c, in m s^{-1}) from ADCP (Dashed black lines).*~~

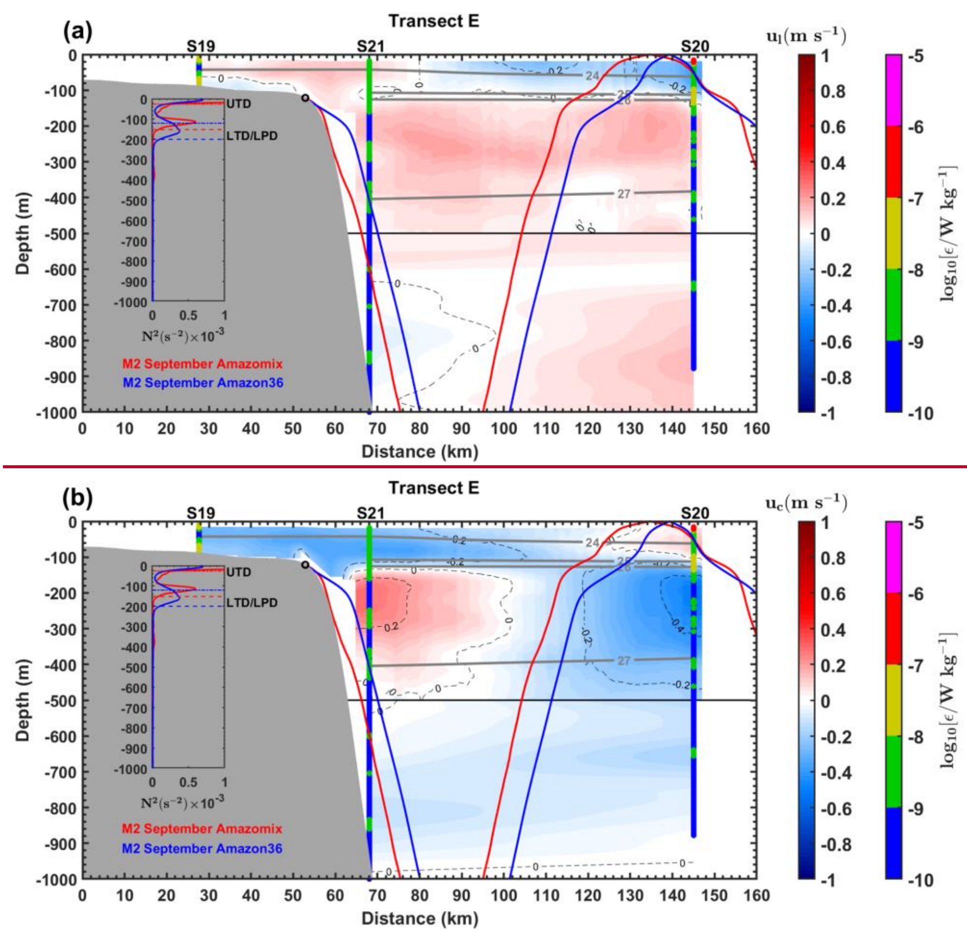

~~*Figure A23: (a) Similar to Fig. 8 but for transect E. (b) Similar to Fig. A22 but for transect E.*~~

~~N° Stations~~	~~XLD (m)~~	~~BKE (J.m^{-2})~~	~~CSBS (mean ± SD) (%)~~	~~CMBS (mean ± SD) (%)~~
~~S2~~	~~45~~	~~-~~	~~-~~	~~-~~
~~S3~~	~~31~~	~~35.4~~	~~-~~	~~-~~
~~S4~~	~~27~~	~~-~~	~~-~~	~~-~~
~~S5~~	~~20~~	~~16.6~~	~~-~~	~~-~~
~~S6~~	~~22~~	~~-~~	~~61.4 ± 5.3~~	~~38.6 ± 5.3~~
~~S7~~	~~46~~	~~-~~	~~47.5 ± 2.8~~	~~52.5 ± 2.8~~
~~S8~~	~~23~~	~~1.1~~	~~-~~	~~-~~
~~S9~~	~~29~~	~~2.6~~	~~-~~	~~-~~
~~S10~~	~~26~~	~~-~~	~~65.8 ± 0.7~~	~~34.2 ± 0.7~~
~~S11~~	~~27~~	~~-~~	~~48.2 ± 5.0~~	~~51.8 ± 5.0~~
~~S12~~	~~49~~	~~-~~	~~54.3 ± 3.1~~	~~48.7 ± 3.1~~
~~S13~~	~~17~~	~~-~~	~~55.4 ± 5.1~~	~~44.6 ± 5.1~~
~~S14~~	~~26~~	~~-~~	~~58.5 ± 1.5~~	~~41.5 ± 1.5~~
~~S19~~	~~27~~	~~0.6~~	~~-~~	~~-~~
~~S20~~	~~44~~	~~-~~	~~52.1 ± 3.8~~	~~47.9 ± 3.8~~
~~S21~~	~~53~~	~~-~~	~~58.5 ± 3.2~~	~~41.5 ± 3.2~~
~~S24~~	~~21~~	~~0.2~~	~~49.1 ± 2.8~~	~~50.9 ± 2.8~~
~~S25~~	~~26~~	~~-~~	~~-~~	~~-~~

SD = Standard Deviation.

Data availability

The AMAZOMIX data can be downloaded directly on the SEANOE site: https://www.seanoe.org/data/00860/97235/. The NEMOv3.6 model outputs are available upon request by contacting the corresponding author.

Authors contributions

AKL: funding acquisition. FK and AKL, with assistance from JM: conceptualization and methodology. FK, with assistance from PR, AB, EC and AKL: data pre-processing. Formal analysis: FK with interactions from all co-authors. Preparation of the manuscript: FK with contributions from all co-authors. This work is a contribution to the LMI TAPIOCA (www.tapioca.ird.fr).

Competing interests

The authors declare that they have no conflict of interest.

Acknowledgments

The authors thank the “Flotte Océanographique Française” and the officers and crew of the R/V Antea for their contributions to the success of operations aboard the vessel. We also appreciate the scientists involved in data and water sample collection for their valuable support during and after the AMAZOMIX cruise. We acknowledge the Brazilian authorities for authorizing the survey. The authors also thank Rockland for providing their instrument and support during the cruise and VMP data analysis, the French National Instrument Park (DT-INSU) for supplying equipment and assisting with data analysis, and US-IMAGO from IRD for its help during the cruise and in biogeochemical data analysis.

Financial support

This work is part of the “AMAZOMIX” project, funded by multiple agencies: the “Flotte Océanographique Française,” which supported the 40 days at sea aboard the R/V Antea; the Institut de Recherche pour le Développement (IRD), including the LMI TAPIOCA program; CNES, through the APR TOSCA MIAMAZ TOSCA project (PIs Ariane Koch-Larrouy, Vincent Vantrepotte, and Isabelle Dadou); LEGOS; and the Franco-Brazilian program GUYAMAZON (Call Nº 005/2017). It is also part of the PhD thesis of Fabius Kouogang, funded by Coordenação de Aperfeiçoamento de Pessoal de Nível Superior (CAPES), under the co-advisement of Ariane Koch-Larrouy and Moacyr Araujo. Co-authors Moacyr Araujo and Alex Costa da Silva acknowledge the Brazilian funding agency CNPq (National Council for Scientific and Technological Development) for their grants.

~~**Acknowledgments**~~

~~The authors would like to thank the “Flotte Océanographique Française” and the officers and crew of the R/V Antea for their contribution to the success of the operations aboard the R/V ANTEA, as well as, all the scientists involved in data and water samples collection, for their valuable support during and after the AMAZOMIX cruise. We acknowledge the Brazilian authorities for authorising the survey. The authors acknowledge Rockland company for their instrument and their support during the cruise and during the analysis of the VMP data, the National french parc of instrument (DT-INSU) for their instrument during the cruise and support in data analysis, as well as, the US-IMAGO from IRD for its help during the cruise and for biogeochemical data analysis.~~

~~**Financial support**~~

~~This work is a part of the project “AMAZOMIX”, funded multiple agencies : the “Flotte Océanographique Française” that funded the 40 days at sea of the R/V Antea, the Institut de Recherche pour le Développement (IRD), via among other the LMI TAPIOCA, the CNES, within the framework of the APR TOSCA MIAMAZ TOSCA project (PIs Ariane Koch-Larrouy, Vincent Vantrepotte, and Isabelle Dadou), the LEGOS and the program international Franco-Brazileiro GUYAMAZON (call Nº 005/2017). It is also part of the PhD Thesis of Fabius Kouogang, funded by the Coordenação de Aperfeiçoamento de Pessoal de Nível Superior (CAPES), under the co-advisement of Ariane Koch-Larrouy and Moacyr Araujo.~~

References

Araujo, M., Noriega, C., Hounsou-gbo, G. A., Veleda, D., Araujo, J., Bruto, L., Feitosa, F., Flores-Montes, M., Lefèvre, N., Melo, P., Otsuka, A., Travassos, K., Schwamborn, R., and Neumann-Leitão, S.: A Synoptic Assessment of the Amazon River-Ocean Continuum during Boreal Autumn: From Physics to Plankton Communities and Carbon Flux, Front. Microbiol., 8:1358, https://doi.org/10.3389/fmicb.2017.01358, 2017.

Assene, F., Koch-Larrouy, A., Dadou, I., Tchilibou, M., Morvan, G., Chanut, J., Costa da Silva, A., Vantrepotte, V., Allain, D., and Tran, T.-K.: Internal tides off the Amazon shelf – Part 1: The importance of the structuring of ocean temperature during two contrasted seasons, Ocean Sci., 20, 43–67, https://doi.org/10.5194/os-20-43-2024, 2024.

Assuncao, R. V., Silva, A. C., Roy, A., Bourlès, B., Silva, C. A. H. S., Ternon, J.-F., Araujo, M., and Bertrand, A.: 3D characterisation of the thermohaline structure in the southwestern tropical Atlantic derived from functional data analysis of in situ profiles, Progress in Oceanography, 187, pp.102399, https://doi.org/10.1016/j.pocean.2020.102399. hal02984588, 2020.

Barbot, S., Lyard, F., Tchilibou, M., and Carrere, L.: Background stratification impacts on internal tide generation and abyssal propagation in the western equatorial Atlantic and the Bay of Biscay, Ocean Sci., 17, 1563–1583, https://doi.org/10.5194/os-17-1563-2021 , 2021.

Barnier, B., Reynaud, T., Beckmann, A., Böning, C., Molines, J.-M., Barnard, S., and Jia, Y.: On the seasonal variability and eddies in the North Brazil Current: insights from model intercomparison experiments, Prog. Oceanogr., 48, 195–230, https://doi.org/10.1016/S0079-6611(01)00005-2, 2001.

Bertrand, A., de Saint Leger, E., and Koch-Larrouy, A.: AMAZOMIX 2021 cruise, RV Antea, https://doi.org/10.17600/18001364, 2021.

Booth, J. and Kamenkovich, I.: Isolating the role of mesoscale eddies in mixing of a passive tracer in an eddy resolving model, J. Geophys. Res., 113, C05021, https://doi.org/10.1029/2007JC004510, 2008.

Bordois, L.: Internal tide modeling : Hydraulic & Topographic controls, Ph.D. thesis, Université Toulouse III Paul-Sabatier, 195 pp., tel-01281760, version 1., https://theses.hal.science/tel-01281760, 2015.

Bourlès, B., Gouriou, Y., and Chuchla, R.: On the circulation in the upper layer of the western equatorial Atlantic, Journal of Geophysical Research, 104, 21151-21170, https://doi.org/10.1029/1999JC900058, 1999.

Bouruet-Aubertot, P., Cuypers, Y., Ferron, B., Dausse, D., Ménage, O., Atmadipoera, A. S., and Jaya, I.: Contrasted turbulence intensities in the Indonesian Throughflow: a challenge for parameterizing energy dissipation rate, Ocean Dynamics, 68, 779–800, https://doi.org/10.1007/s10236-018-1159-3, 2018.

Brainerd, K., and Gregg M. C.: Surface mixed and mixing layer depths, Deep Sea Res., 42(9), 1521–1543, https://doi.org/10.1016/0967-0637(95)00068-H, 1995.

Cisewski, B., Strass, V. H., Losch, M., and Prandke, H.: Mixed layer analysis of a mesoscale eddy in the Antarctic Polar Front Zone, J. Geophys. Res., 113, C05017, https://doi.org/10.1029/2007JC004372, 2008.

Coles, V. J., Brooks, M. T., Hopkins, J., Stukel, M. R., Yager, P. L., and Hood, R. R.: The pathways and properties of the Amazon River Plume in the tropical North Atlantic Ocean, Journal of Geophysical Research, 118, 6894-6913, https://doi.org/10.1002/2013JC008981, 2013.

Didden, N. and Schott, F.: Eddies in the North Brazil Current retroflection region observed by Geosat altimetry, J. Geophys. Res., 98, 20121, https://doi.org/10.1029/93JC01184, 1993.

de Boyer Montégut, C., Madec G., Fischer A. S., Lazar A., and Iudicone D.: Mixed layer depth over the global ocean: An examination of profile data and a profile-based climatology, J. Geophys. Res., 109, C12003, https://doi.org/10.1029/2006JC004051, 2004.

de Macedo, C. R., Koch-Larrouy, A., da Silva, J. C. B., Magalhães, J. M., Lentini, C. A. D., Tran, T. K., Rosa, M. C. B., and Vantrepotte, V.: Spatial and temporal variability in mode-1 and mode-2 internal solitary waves from MODIS-Terra sun glint off the Amazon shelf, Ocean Sci., 19, 1357–1374, https://doi.org/10.5194/os-19-1357-202, 2023.

Dossa, N., da Silva, A. C., Koch-Larrouy, A., and Kouogang, F.: Near-surface western boundary circulation off the Amazon Plume from AMAZOMIX data, in preparation, 2024.

Fer, I., Dengler, M., Holtermann, P. et al.: ATOMIX benchmark datasets for dissipation rate measurements using shear probes, Sci Data, 11, 518, https://doi.org/10.1038/s41597-024-03323-y, 2024.

Gerkema, T., and Zimmerman, J. T. F.: An Introduction to Internal Waves, 207 pp, 2008

Geyer, W. R.: Tide-induced mixing in the Amazon Frontal Zone, J. Geophys. Res., 100, 2341, https://doi.org/10.1029/94JC02543, 1995.

Gille, S.T., Ledwell, J., Naveira-Garabato, A., Speer, K., Balwada, D., Brearley, A., Girton, J.B., Griesel, A., Ferrari, R., Klocker, A., LaCasce, J., Lazarevich, P., Mackay, N., Meredith, M.P., Messias, M.-J., Owens, B., Sallée, J.-B., Sheen, K., Shuckburgh, E., Smeed, D. A., St. Laurent, L.C., Toole, J.M., Watson, A.J., Wienders, N., and Zajaczkovski, U.: The diapycnal and isopycnal mixing experiment: a first assessment, CLIVARExchanges, 17(1), 46–48, https://nora.nerc.ac.uk/id/eprint/18245, 2012.

Gregg, M., Sanford, T., and Winkel, D.: Reduced mixing from the breaking of internal waves in equatorial waters, Nature, 422, 513–515, https://doi.org/10.1038/nature01507, 2003.

Huang, P.-Q., Cen, X.-R., Lu, Y.-Z., Guo, S.-X., and Zhou, S.-Q.: Global distribution of the oceanic bottom mixed layer thickness, Geophysical Research Letters, 46, 1547–1554, https://doi.org/10.1029/2018GL081159, (2019).

Huthnance, J. M.: Circulation, exchange and water masses at the ocean margin: the role of physical processes at the shelf edge, Progress in Oceanography, 35, 353–431, https://doi.org/10.1016/0079-6611(95)80003-C, 1995.

Inall, M. E., Toberman, M., Polton, J. A., Palmer, M. R., Green, J. A. M., and Rippeth, T. P.: Shelf Seas Baroclinic Energy Loss: Pycnocline Mixing and Bottom Boundary Layer Dissipation, Journal of Geophysical Research: Oceans, 126(8):2020JC016528, https://doi.org/10.1029/2020JC016528, 2021.

Ivey, G. N., Bluteau, C. E., Gayen, B., Jones, N. L., and Sohail, T.: Roles of Shear and Convection in Driving Mixing in the Ocean, Geophysical Research Letters, 48(3), e2020GL089455, https://doi.org/10.1029/2020GL089455, 2021.

Jackson, C. R., da Silva, J. C. B., and Jeans, G.: The generation of nonlinear internal waves, Oceanography, 25(2):108–123, https://doi.org/10.5670/oceanog.2012.46, 2012.

Johns, W. E., Lee, T. N., Beardsley, R. C., Candela, J., Limeburner, R., and Castro Filho, B. M. : Annual Cycle and Variability of the North Brazil Current, Journal of Physical Oceanography, 28(1), 103-128, https://doi.org/10.1175/15200485(1998)028%3C0103:acavot%3E2.0.co;2, 1998.

Koch-Larrouy, A., Atmadipoera, A., van Beek, P., Madec, G., Aucan, J., Lyard, F., Grelet, J., and Souhaut, M.: Estimates of tidal mixing in the Indonesian archipelago from multidisciplinary INDOMIX in-situ data, Deep Sea Research Part I: Oceanographic Research Papers, 106, pp.136-153, https://doi.org/10.1016/j.dsr.2015.09.007, 2015.

Koch-Larrouy, A., Lengaigne, M., Terray, P., Madec, G., and Masson, S.: Tidal mixing in the Indonesian Seas and its effect on the tropical climate system, Clim. Dynam., 34, 891–904, https://doi.org/10.1007/s00382-009-0642-4, 2010.

Koch-Larrouy, A., Kerhervé, D., and Kouogang, F.: Evidence of overturns from AMAZOMIX off the Amazon shelf along internal tides paths, in preparation, 2024.

Klymak, J. M., Pinkel, R., and Rainville, L.: Direct breaking of the internal tide near topography: Kaena ridge, hawaii, J. Phys. Oceanogr., 38 (2), 380–399, https://doi.org/10.1175/2007JPO3728.1, 2008.

Kunze, E.: The internal-wave-driven meridional overturning circulation, J. Phys. Oceanogr., 47, 2673–2689, https://doi.org/10.1175/JPO-D-16-0142.1, 2017.

Le Bars, M., Lacaze, L., Le Dizes, S., Le Gal, P., and Rieutord, M.: Tidal instability in stellar and planetary binary systems, Physics of the Earth and Planetary Interiors, 178, 48-55, https://doi.org/10.1016/j.pepi.2009.07.005, 2010.

Lozovatsky, I. D., Roget, E., Fernando, H. J. S., Figueroa, M., and Shapovalov, S.: Sheared turbulence in a weakly stratified upper ocean, Deep Sea Res. Part I, 53, 387–407, https://doi.org/10.1016/j.dsr.2005.10.002, 2006.

Lueck, R., Fer, I., Bluteau, C., Dengler, M., Holtermann, P., Inoue, R., LeBoyer, A., Nicholson, S., Schulz, K., and Stevens, C.L: Best practices recommendations for estimating dissipation rates from shear probes, Frontiers in Marine Science, https://doi.org/10.3389/fmars.2024.1334327, 2024.

MacKinnon, J. A., and Gregg, M. C.: Mixing on the Late-Summer New England Shelf-Solibores, Shear, and Stratification, Journal of Physical Oceanography, 33, 1476-1492, https://doi.org/10.1175/1520-0485(2003)033<1476:MOTLNE>2.0.CO;2, 2003.

Madec, G., Bourdallé-Badie, R., Chanut, J., Clementi, E., Cow-ard, A., Ethé, C., Iovino, D., Lea, D., Lévy, C., Lo-vato, T., Martin, N., Masson, S., Mocavero, S., Rousset,C., Storkey, D., Vancoppenolle, M., Müeller, S., Nurser, G., Bell, M., and Samson, G.: NEMO ocean engine, Zenodo, https://doi.org/10.5281/zenodo.3878122, 2019.

Magalhaes, J. M., da Silva, J. C. B., Buijsman, M. C., and Garcia, C. A. E.: Effect of the North Equatorial Counter Current on the generation and propagation of internal solitary waves off the Amazon shelf (SAR observations), Ocean Sci., 12, 243–255, https://doi.org/10.5194/os-12-243-2016, 2016.

M'hamdi, A., Koch-Larrouy, A., Bosse, A., de Macedo, C., Vantrepotte, V., Dadou, I., da Silva, A. C., and Kouogang, F.: Internal tides imprints on chlorophyll in mesoscale intrathermocline lenses detected from ocean color and from in-situ glider data off the Amazon shelf, Ocean Sci., (in preparation), 2024.

Miles, J. W.: On the stability of heterogeneous shear flows, Journal of Fluid Mechanics, 10(4):496-508, https://doi.org/10.1017/S0022112061000305, 1961.

Muacho, S., da Silva, J. C. B., Brotas, V., Oliveira, P. B., and Magalhaes, J. M.: Chlorophyll enhancement in the central region of the Bay of Biscay as a result of internal tidal wave interaction, Journal of Marine Systems, 136, 22–30, https://doi.org/10.1016/j.jmarsys.2014.03.016, 2014.

Munk, W., and Wunsch, C.: Abyssal recipes II: Energetics of tidal and wind mixing. Deep Sea Research, Part I: Oceanographic Research Papers, 45, 1977–2010, https://doi.org/10.1016/S0967-0637(98)00070-3, 1998.

Nasmyth, P. W.: Oceanic turbulence, Ph.D. thesis, University of British Columbia, 71 pp, https://doi.org/10.14288/1.0084817, 1970.

Neto, A. V. N., and da Silva, A. C.: Seawater temperature changes associated with the North Brazil current dynamics, Ocean Dynamics, 64, 13–27, https://doi.org/10.1007/s10236-013-0667-4, 2014.

New, A. L., and Pingree, R. D.: Local Generation Of Internal Soliton Packets In The Central Bay Of Biscay, Deep-Sea Research Part A-Oceanographic Research Papers, 39 (9A), 1521 - 1534, https://doi.org/10.1016/0198-0149(92)90045-U, 1992.

New, A., and da Silva, J.: Remote-sensing evidence for the local generation of internal soliton packets in the central Bay of Biscay, Deep Sea Research Part I: Oceanographic Research Papers, 49, 915–934, https://doi.org/10.1016/S09670637(01)00082-6, 2002.

Noh, Y., Lee, WS.: Mixed and mixing layer depths simulated by an OGCM, J. Oceanogr., 64, 217–225, https://doi.org/10.1007/s10872-008-0017-1, 2008.

Nugroho, D., Koch-Larrouy, A., Gaspar, P., Lyard, F., Reffray, G., and Tranchant, B.: Modelling explicit tides in the Indonesian seas: An important process for surface sea water properties, Mar. Pollut. Bull., 131, 7–18, https://doi.org/10.1016/j.marpolbul.2017.06.033, 2018.

Osborn, T. R.: Estimates of the local rate of vertical diffusion from dissipation measurements, J. Phys. Oceanogr, 10, 83–89, https://doi.org/10.1175/1520-0485(1980)010<0083:EOTLRO>2.0.CO;2, 1980.

Prestes, Y. O., Silva, A. C., and Jeandel, C.: Amazon water lenses and the influence of the North Brazil Current on the continental shelf, Continental Shelf Research, 160, 36-48, https://doi.org/10.1016/j.csr.2018.04.002, 2018.

Rainville, L., and Pinkel, R.: Propagation of Low-Mode Internal Waves through the Ocean, Journal of Physical Oceanography, 36:1220, 2006, https://doi.org/10.1175/JPO2889.1, 2006.

Ray, R. D., and Susanto, R. D.: Tidal mixing signatures in the Indonesian seas from high resolution sea surface temperature data. Geophys, Res. Lett, 43, 8115–8123, https://doi.org/10.1002/2016GL069485, 2016.

Rippeth, T. P., Palmer, M. R., Simpson, J. H., Fisher, N. R., and Sharples, J.: Thermocline mixing in summer stratified continental shelf sea, Geophys. Res. Lett, 32 (5), L05602, https://doi.org/10.1029/2004GL022104, 2005.

Ruault, V., Jouanno, J., Durand, F., Chanut, J., and Benshila, R.: Role of the Tide on the Structure of the Amazon Plume: A Numerical Modeling Approach, J. Geophys. Res.-Oceans, 125, e2019JC015495, https://doi.org/10.1029/2019JC015495, 2020.

Sheen, K. L., Brearley, J. A., Naveira Garabato, A. C., Waterman, S., Smeed, D. A., Ledwell, J. R., Meredith, M. P., St. Laurent, L., Thurnherr, A. M., Toole, J. M., and Watson, A. J.: Rates and mechanisms of turbulent dissipation and mixing in the Southern Ocean: Results from the Diapycnal and Isopycnal Mixing Experiment in the Southern Ocean (DIMES), J. Geophys. Res. Oceans, 118, 2774–2792, https://doi.org/10.1002/jgrc.20217, 2013.

Simpson, J. H., and Sharples, J.: Introduction to the physical and biological oceanography of shelf seas, Cambridge University Press, pp. 1-24, https://doi.org/10.1038/250404a0, 2012.

Silva, J. D., Buijsman, M. C., and Magalhaes, J.: Internal waves on the upstream side of a large sill of the Mascarene Ridge: a comprehensive view of their generation mechanisms and evolution, Deep Sea Research Part I: Oceanographic Research Papers, 99, 87-104, https://doi.org/10.1016/j.dsr.2015.01.002, 2015.

Solano, M. S., Buijsman, M. C., Shriver, J. F., Magalhaes, J., da Silva, J., Jackson, C., Arbic, B. K., and Barkan, R.: Nonlinear internal tides in a realistically forced global ocean simulation, Journal of GeophysicalResearch: Oceans, 128, https://doi.org/10.1029/2023JC019913, 2023.

Sprintall, J., Gordon, A. L., Koch-Larrouy, A., Lee, T., Potemra,J. T., Pujiana, K., and Wijffels, S.: The Indonesian Seas and their impact on the Coupled Ocean Climate System, Nat. Geosci., 7, 487–492, https://doi.org/10.1038/NGEO2188, 2014.

Stansfield, K., Garrett, C., Dewey, R.: The probability distribution of the Thorpe displacement within overturns in Juan de Fuca Strait, J. Phys. Oceanogr, 31, 3421–3434, https://doi.org/10.1175/1520-0485(2001)031<3421:TPDOTT>2.0.CO;2, 2001.

St. Laurent, L. C., Garabato, A.N., Ledwell, J.R., Thurnherr, A.M., Toole, J.M., and Watson, A. J.: Turbulence and diapycnal mixing in Drake Passage, Journal of Physical Oceanography, 42, 2143-2152, https://doi.org/10.1175/JPO-D-12-027.1, 2012.

Sutherland, G., Reverdin, G., Marié, L., and Ward, B.: Mixed and mixing layer depths in the ocean surface boundary layer under conditions of diurnal stratification, Geophys. Res. Lett, 41, 8469–8476, https://doi.org/10.1002/2014GL061939, 2014.

Takahashi, A., and Hibiya, T.: Assessment of finescale parameterizations of deep ocean mixing in the presence of geostrophic current shear: Results of microstructure measurements in the Antarctic Circumpolar Current region, Journal of Geophysical Research: Oceans, 124, 135–153, https://doi.org/10.1029/2018JC014030, 2019.

Tchilibou, M., Koch-Larrouy, A., Barbot, S., Lyard, F., Morel, Y., Jouanno, J., and Morrow, R.: Internal tides off the Amazon shelf during two contrasted seasons: Interactions with background circulation and SSH imprints, Ocean Science Discussions, 14, 1283–1301, https://doi.org/10.5194/os-18-1591-2022, 2022.

Thorpe S. A.: Turbulence in the ocean pycnocline. In: An Introduction to Ocean Turbulence, Cambridge University Press, 116-157, 2007.

Thorpe, S. A.: Models of energy loss from internal waves breaking in the ocean, Journal of Fluid Mechanics, 836, 72–116, https://doi.org/10.1017/jfm.2017.780, 2018.

Varona, H. L., Veleda, D., Silva, M., Cintra, M., and Araujo, M.: Amazon River plume influence on Western Tropical Atlantic dynamic variability, Dynamics of Atmospheres and Oceans, 85, pp.1-15, https://doi.org/10.1016/j.dynatmoce.2018.10.002, 2018.

Wang, Y.-H., Dai, C.-F., and Chen, Y.-Y.: Physical and ecological processes of internal waves on an isolated reef ecosystem in the South China Sea, Geophysical Research Letters, 34(18), https://doi.org/10.1029/2007gl030658, 2007.

Whalen, C. B., Talley, L. D., and MacKinnon, J. A.: Spatial and temporal variability of global ocean mixing inferred from Argo profiles, Geophys. Res. Lett, 39:L18612, https://doi.org/10.1029/2012GL053196, 2012.

Xie, X. H., Cuypers, Y., Bouruet-Aubertot, P., Ferron, B., Pichon, A., Lourenço, A., and Cortes, N.: Large-amplitude internal tides, solitary waves, and turbulence in the central Bay of Biscay, Geophysical Research Letters, 40(11), 2748–2754, https://doi.org/10.1002/grl.50533, 2013.

Xu, P., Yang, W., Zhu, B., Wei, H., Zhao, L., and Nie, H.: Turbulent mixing and vertical nitrate flux induced by the semidiurnal internal tides in the southern Yellow Sea, Continental Shelf Research, 208, 104240, https://doi.org/10.1016/j.csr.2020.104240, 2020.

Yang, W., Wei, H., Zhao, L., and Zhang, J.: Turbulence and vertical nitrate flux adjacent to the Changjiang Estuary during fall, Journal of Marine Systems, 212: 103427, https://doi.org/10.1016/j.jmarsys.2020.103427, 2020.

Zaron, E. D., Capuano, T. A., and Koch-Larrouy, A.: Fortnightly variability of Chl a in the Indonesian seas, Ocean Sci., 19, 43–55, https://doi.org/10.5194/os-19-43-2023, 2023.

Zhao, Z., Alford, M. H., Girton, J. B., Rainville, L., and Simmons, H. L.: Global Observations of Open-Ocean Mode-1 M2 Internal Tides, J. Phys. Oceanogr., 46, 1657–1684, https://doi.org/10.1175/JPO-D-15-0105.1, 2016

Zhao, Z., Alford, M. H., and Girton, J.B.: Mapping low-mode internal tides from multisatellite altimetry, Oceanography, 776 25(2):42–51,https://doi.org/10.5670/oceanog.2012.40, 2012.